Hamburg University of Technology

Institute for ship structural design and analysis (M-10)

Master thesis

The Measurement Accuracy of instrumented Ship Structures under local Loads using Strain Gauges

B.Sc. Angelo Mario Böhm

Supervisor:	M.Sc. Hauke Herrnring
First examiner:	Prof. D.Sc. (Tech.) Sören Ehlers
Secound examiner:	D.Sc. (Tech.) Rüdiger U. Franz von Bock und Polach
Registration number:	21266467

April 4, 2019

Contents

List of Figures

List of Tables

List of Symbols

Symbol	Meaning	Unit
U_M	Measured voltage within the wheatstone bridge	[V]
U_B	Bridge supply voltage of the wheatstone bridge	[V]
$R_1 \dots R_4$	Resistances in the bridge branches	[Ω]
R_0	Nominal resistances of the strain gauge	[Ω]
$\varepsilon_{\text{StrainGauge}}$, ε_{SG}	Strain amount recorded by the strain gauge	[-]
k	Describes the relationship between the change in resistance $\mathrm{d}R/R$ and the strain captured by the strain gauge	[-]
ΔT	Temperature deviation from the reference temperature	[-]
α_k	Influence-factor of temperature on the sensitivity of the strain gauges	[-]
k_T	k-factor at any temperature T within the linear range	[-]
α_R	Temperature-dependent change of the specific resistance of the measuring grid material of the strain gauge	[-]
α_M	Thermal coefficient of linear expansion of the measuring grid	[-]
α_B	Thermal coefficient of linear expansion of the component	[-]
τ	Shear stress	[N/m^2]
γ	Shear strain	[-]
L	Frame length	[m]
s	Frame spacing	[m]
h_w	Web height	[m]
t_w	Web thickness	[m]
t_p	Plate thickness	[m]
E	Young's modulus	[Pa]
ν	Poission's ratio	[-]
$q_i L$, Q	Shear forces acting on the frames	[N]
T_i	Torsion	[Nm]
F	External loading	[N]
D	Bending stiffness of the plate	[Nm]
I	Second moment of area	[m^4]
I_T	Torsion constant	[m^4]
G	Shear modulus	[N/m^2]
$\boldsymbol{K}$	Stiffness matrix	[-]
$\boldsymbol{F}$	Load vector	[N]
$\boldsymbol{a}$	Influence coefficient matrix	[N]
$\boldsymbol{c}$	Inverse of the influence coefficient matrix	[1/N]
p	Ice pressure	[Pa]
μ	Mean value	[-]
σ	Standard deviation	[-]
ξ	Load location	[m]

Symbol	Meaning	Unit
α	Significance level	[-]
p	p-value, probability value	[-]
ℓ	Load length	[m]
R^2	Coefficient of determination	[-]

Declaration of Academic Integrity

I, *Angelo Mario Böhm* (Student of Naval Architecture and Ocean Engineering at Hamburg University of Technology, student number 21266467) hereby confirm that the present master's thesis on

> *The Measurement Accuracy of instrumented Ship Structures under local Loads using Strain Gauges*

is solely my own work and that if any text passages or diagrams from books, papers, the Web or other sources have been copied or in any other way used, all references - including those found in electronic media - have been acknowledged and fully cited.

Hamburg, April 4, 2019

Angelo Mario Böhm

1. Abstract

The State of the Art measurement set up for ice loads measurements is as follows. On four to five frames there are strain gauges attached on each end for measurements of shear-strain differences. With the help of a finite element analysis (FEA) the load strain relation of the instrumented section can be determined. This load strain relation is displayed in the so-called influence coefficient matrix which is obtained by the unit load principle.
Nevertheless after the many past measurements the following questions arise. How accurate is the mapping of the influence coefficient matrix? Which structures are suitable for measurements of shear-strain differences? How can the existing method be improved and what measurement uncertainties are inherent in the overall system?
In order to achieve the goal of this work, the theory of shear-strain measurement was presented. In addition to shear-strain measurement, the theory of shear-strain measurement on ships for the determination of ice loads was explained. Besides a grillage model which consists of five frames and one plate was modeled and point loads and pressures were investigated by finite element analysis. Under the given conditions symmetrical structures with a good load alignment are suitable for measurements of shear-strain differences.
Besides, the author shows how the influence coefficient matrix maps the response of the structure. The best mapping of the influence coefficient matrix could be achieved with a double instrumentation of the frames.
The location of the load, the load length and the pressure distribution within the contact area were one of the biggest uncertainties according to [17]. The author shows how the already existing measurement system can determine loads in the middle of the frames. In addition an approach to estimate the load length is presented as well. At the end there is a recommendation for further investigations of this kind.

2. Introduction

Short see routes and natural resources increased the interest and activities in arctic waters. Ships operating in ice-covered waters experience intense loads from ice. In Figure 1 the ice breaking patter around the ship's hull is shown. However, the knowledge about the ice-structure interaction of ships is limited. In addition, the availability of full scale measurements is limited. In the previous project thesis the author dealt with an analysis of a finite element model of a multi-purpose dry cargo ship for measurements of ice loads on the ship's hull using strain gauges [3]. First of all, the author had chosen a section for the instrumentation which suits the needs of a strain gauge measurement the most. This model was then build in a Computer Aided Design (CAD) program and analyzed in a Computer Aided Engineering (CAE) program. For the finite element analysis (FEA), *Ansys 18.2* was used. The behavior of the structure under the design ice load according to the *Finnish-Swedish Ice Class Rules* (FSICR) [19] was investigated, the ice-structure interaction of the modeled section was determined by the calculation of an influence coefficient matrix (ICM) and at the end the applicability of the used methods was discussed.

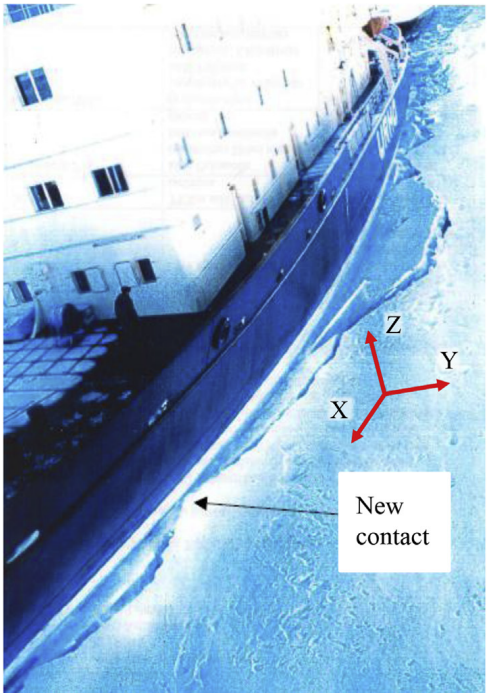

Figure 1: The breaking pattern around the ship hull. Figure taken from [7].

The major concern in FEA is the required computing power, the time taken to run the analysis and the amount of memory the analysis needs. When examine a local part of a global structure there are mainly two possibilities to overcome these concerns. One possibility positions the local model with the high-dense mesh directly within the overall global model with the coarse mesh. Another possibility runs the analysis in two stages.

First the global model is calculated and either the nodal forces or nodal displacements are extracted from the boundary. Second the local model is calculated using the boundary conditions which are extracted from the global model. The first possibility offers an analysis in a single run with the global-to-local interface as a key issue. The analysis with an independent local model requires accurate and meaningful interpolation of either boundary forces or displacements. The overriding consideration in global/local modeling is that the strain energy on the global and local boundaries should balance. In order to achieve this, the displacement and the force should be used at the same time [1]. The author will use an independent simple local model where different boundary conditions will be investigated. Possible sources of errors are discussed in Section 8.
There are two possibilities to measure ice loads on a ship's hull. On the one hand the load can be measured directly by instrumenting the contact area with pressure sensors and on the other hand the load can be measured indirectly by measuring the response of the structure. In Table 1 the full-scale measurements based on strain measurements are shown and in Table 2 the full-scale measurements based on other than strain measurements are shown.

Table 1: Full-scale measurements based on the strain measurements. Table taken from [17].

IB Urho, Baltic Sea, 1976	Shear strain
MT Igrim, Baltic Sea, 1978	Shear strain
IB Sisu, Baltic Sea, 1978-85	Shear strain difference
CANMAR Kigoriak, Arctic, 1979	Shear strain
USCGC Polar Sea, Arctic, Antarctica, 1982-84	Compressive strain normal to shell
MS Arcturus, Baltic Sea, 1983-88	Shear strain difference
RV Polarstern, Arctic, 1984-85	Strain
MT Kashira, Baltic Sea, Arctic, 1984-90	Shear strain difference
MS Kemira, Baltic Sea, 1985-91	Shear strain difference
IB Oden, Arctic, 1991, 1996	Shear strain difference
RV Nathanial B. Palmer, Antarctica, 1992	Compressive strain normal to shell
CCGS Louis S. St. Laurent, Arctic, 1994-95	Shear strain difference
MT Uikku, Arctic, Baltic Sea, 1998, 2000-01, 03	Shear strain difference
PM Teshio, Sea of Okhotsk, 1998-99	Shear strain difference
USCGC Healy, Arctic, 2000	Shear strain difference
CCGS Terry Fox, Arctic, 2001	Shear strain difference
PV Soya, Southern Sea of Okhotsk, 2005-09	Shear strain difference
IB Otso, Baltic Sea, 2005	Shear strain difference
KV Svalbard, Arctic, 2007-08	Shear strain
PSRV S.A. Agulhas II, Baltic Sea, Antarctica, 2012-18	Shear strain difference

Table 2: Full-scale measurements based on other than strain measurements. Table taken from [17].

MT Igrim, Baltic Sea, 1978	Special type of pressure gauge installed inside the hull
IB Sisu, Baltic Sea, 1978-85	Special type of pressure gauge installed inside the hull
CANMAR Kigoriak, Arctic, 1979	Special type of pressure gauge installed inside the hull
CCGS Louis S. St. Laurent, Arctic, 1980	Through hull pressure sensors
MS Arcturus, Baltic Sea, 1983-88	Special type of pressure gauge installed inside the hull
MT Kashira, Baltic Sea, Arctic, 1984-90	Special type of pressure gauge installed inside the hull
RV Polarstern, Arctic, 1984-85	Triaxial load sensor installed in pockets
IB Sampo, Baltic Sea, 1989	External PVDF-pressure panel
CCGS Terry Fox, Arctic, 2001	External impact panel based on optic measurements

The most common approach is to measure the ice loads indirectly by using strain gauges [17]. In this thesis the author will be focusing on the indirect measurements based on the shear-strain difference. The shear-strains will be measured on the end of the frames of the ship [3]. From here on the exerted force is extrapolated by using an influence coefficient matrix. One can imagine, that most commonly the frames in the bow area are instrumented since here the first impact with the ice occurs. However, various maneuvers have an influence on the first contact area.
The author of [17] dealt with uncertainties and variations in measured ice-induced loads on a ship's hull. Mainly, the pressure distribution within the contact area in the horizontal direction and the load length are the main uncertainties affecting the measurement results in shear-strain difference-based measurements.
Following questions are dealt within this thesis. How accurate is the mapping of the ICM? Which structures are suitable for measurements of shear-strain differences? How can the existing method be improved and what measurement uncertainties are inherent in the overall system?

3. Strain gauge measurements

In this Section the theory of strain gauge measurements will be described. The following derivations are based upon [6].
The measurement approach with strain gauges is, that electrical resistors changing their resistance as they are lengthened. The advantage of strain gauges is that they convert the strain into an electrical signal. The mechanical quantity to be measured, the strain, produces a change in resistance in the strain gauge, which then changes the output voltage of the Wheatstone bridge circuit. The strain gauge is actually a component of the Wheatstone bridge circuit. Furthermore, the measured parameter strain is converted into an electrical parameter that can be easily further processed. In addition, the Wheatstone bridge circuit offers an excellent possibility of largely compensating for the effects of undesirable influences such as those caused by temperature changes. The Wheatstone bridge circuit is described in more detail in the next Subsection 3.1. Further in text, the output voltage is then amplified and the thus produced measurement signal is displayed or recorded. The schema is shown in Figure 2.

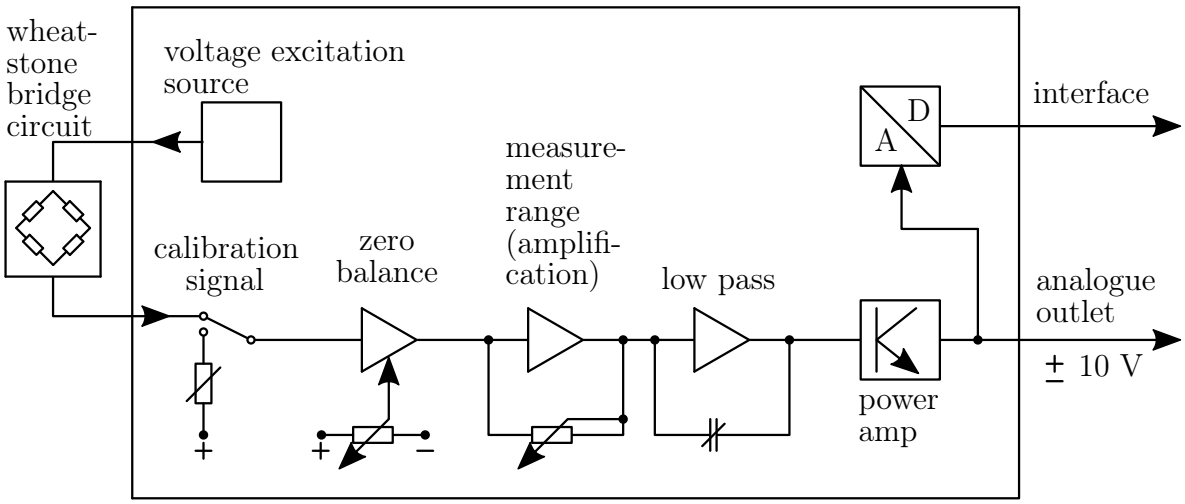

Figure 2: Concept of analogue measurement system with A/D-converter and digital output.

So the basic principle of the strain gauge is, that strain changes occurring on the surface of the measurement object are transfered on an electrical conductor fixed on this surface which then changes its resistance accordingly. From the measured change in resistance, the strain change can be determined with high precision [6].

3.1. Wheatstone bridge circuit

The State of the Art to measure the change in resistance of a strain gauge is to utilize it in a so-called Wheatstone bridge circuit. The following derivations are based upon [6]. Figure 3 shows the schematic principle structure of a Wheatstone bridge circuit.

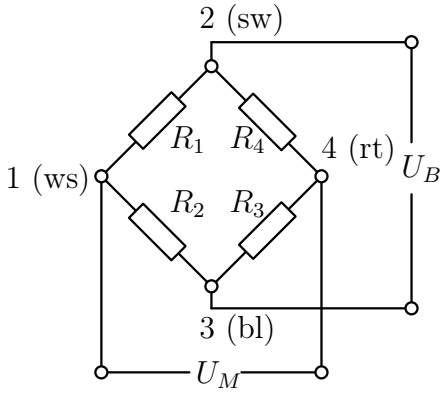

Figure 3: Wheatstone bridge circuit.

As it can be seen, the bridge circuit consists of four bridge branches with resistors R_1 to R_4, where U_B is the bridge supply voltage, U_M is the measured voltage, Node 2 and Node 3 are the nodes for the bridge-supply voltage and Node 1 and Node 4 are the nodes for the measured voltage.
The principle of the circuit is to compare the output voltage of two parallel voltage dividers. If realized with strain gauges, in the initial state, all resistances are equal, and therefore the measured voltage is zero (balanced Wheatstone bridge). If a resistor changes its resistance, the electric potential between the two resistors of that branch changes, which results in a measurable voltage between Node 1 and Node 4 (unbalanced Wheatstone bridge). Additional to that, the measured voltage is linearly dependent to the bridge supply voltage [20]. Using the Kirchoff's law for this circuit results in the following equation.

$$\frac{U_M}{U_B} = \frac{R_1}{R_1 + R_2} - \frac{R_4}{R_3 + R_4} \tag{1}$$

This equation shows that the ratio U_M/U_B is independent of U_B itself, which is why the resistance determination is also possible with unstable voltage sources. It is intended, when measuring with strain gauges, that resistance changes ΔR_i are allowed within the circuit. Then by introducing a nominal resistance R_0 of the strain gauges,

$$R_1 = R_2 = R_3 = R_4 = R_0 \tag{2}$$

and using the assumption of $\Delta R_i \ll R_0$, Equation 1 will leads to the simplified basic equation of Wheatstone's bridge circuit for measuring with strain gauges as follows.

$$\frac{U_M}{U_B} = \frac{(\Delta R_1 - \Delta R_2 + \Delta R_3 - \Delta R_4)}{2(2R_0 + \Delta R_1 + \Delta R_2 + \Delta R_3 + \Delta R_4)} \tag{3}$$

It can be seen from Equation 3 that resistance changes of the same magnitude in all bridge branches have no effect on the output voltage U_M. Wheatstone's bridge circuit thus opens up excellent possibilities for compensating for the effects of interferences that affect the entire circuit. If, for example, the four strain gauges of the bridge circuit are subjected to the same temperature change at the same time, this causes the same resistance change in all strain gauges and the output signal of the bridge circuit remains unaffected. More about the sensitivity of strain gauges will be discussed in the Subsection 3.3.
Measuring with strain gauges in the arrangement of the Wheatstone bridge circuit requires the presence of all four bridge branches, but not all four branches need to be measuring branches equipped with strain gauges. For example, two or three of the bridge branches can be replaced by fixed resistors or so-called dummies and strain gauges can only be arranged in the remaining branches.
This results in the possibility of using so-called full, half and quarter bridge circuits. However, these designations refer only to the part of the bridge in which strain gauges are used. As shown in Figure 4, the half and quarter bridge circuits are supplemented to form complete Wheatstone bridges by fixed resistors which can be connected in the measuring device.

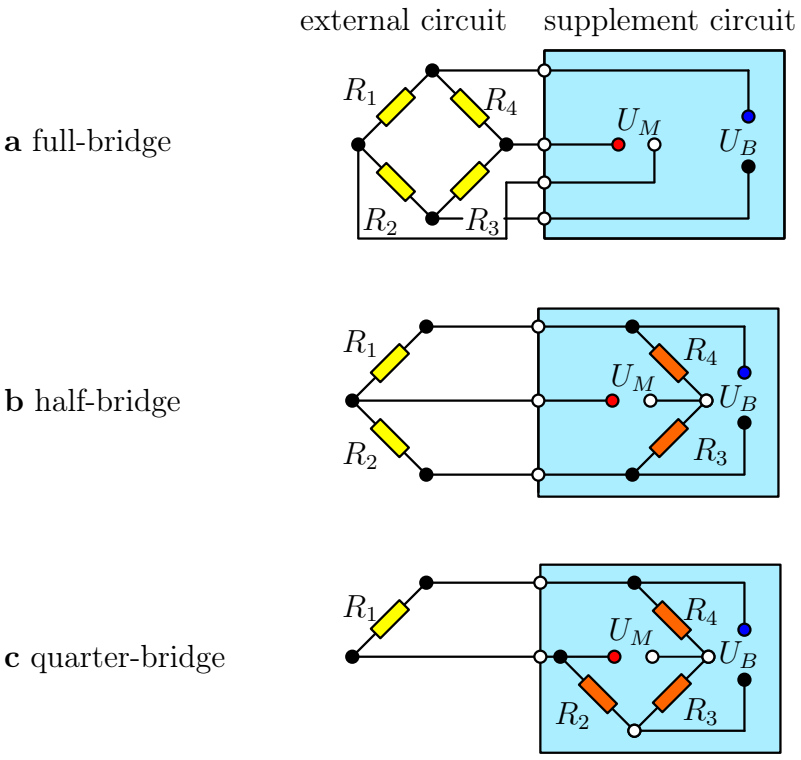

Figure 4: Full-, half- and quarter-bridge for measurement with strain gauges.

For more detailed information regarding the Wheatstone bridge the author refers to [15].

3.2. Structure of strain gauges

The basic structure of a sheet strain gauge as it is used today in huge quantities in many areas of application is explained in Figure 5.

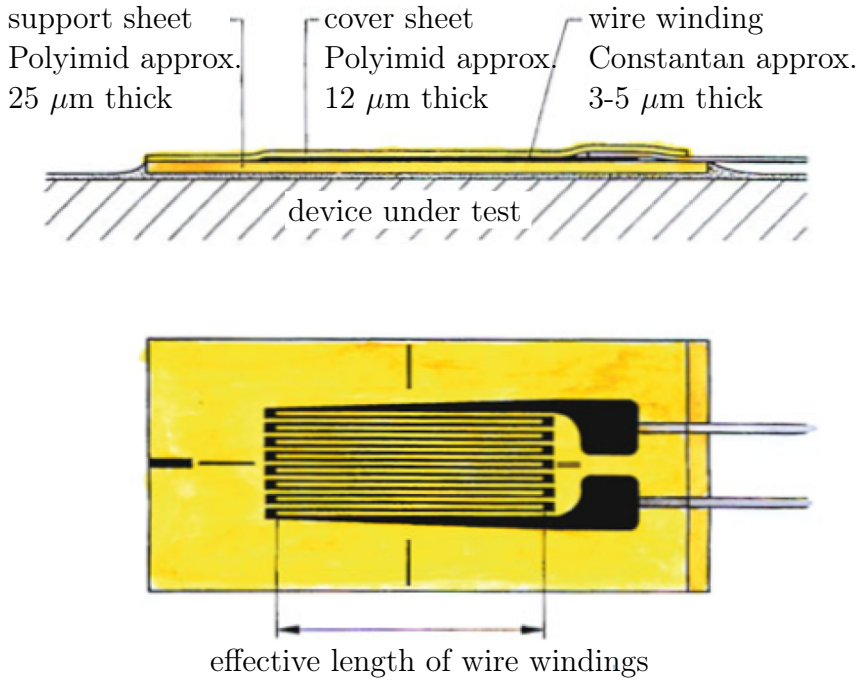

Figure 5: Modern sheet based strain gauge. Figure taken and translated from [6].

The following descriptions are based upon [6]. On an isolating carrier sheet of plastic, which is approx. 25 μm thick, there is an approx. 5 μm thick metallic measuring-grid-sheet. Towards the top, the measuring grid is protected by an approx. 12 μm thick covering layer.
Strain gauges are used to measure, in the longitudinal direction of its measuring-grid, the occurring mechanical strain. This strain produces a change in the resistance of the measuring-grid and thus a measurable change of the electrical bridge circuit in which the strain gauge is located. However, resistance changes in the strain gauge can also be caused by influences other than the mechanical strain occurring in the measuring direction of the strain gauge. In addition to the actual measured value *mechanical strain in measuring direction* are generally thermal influences and creep phenomena the most important causes of resistance changes. Hydrostatic pressure on an installed strain gauge also causes a change in resistance. The lateral strain influence, i.e. the change in resistance caused by strains acting transversely to the measuring direction, can be important for precision measurements. Since hydrostatic pressure is not expected in ice load measurements and with the development of modern sheet strain gauges, the lateral strain sensitivity has lost its importance. The author will only deal with the thermal influences and the influence of creep in Subsection 3.3.

Strain gauges measure the mean strain on the surface of the measurement object at the installation surface as defined in the following equation.

$$\varepsilon_{StrainGauge} = \int_{x_2}^{x_1} \frac{\varepsilon(x)}{x_2 - x_1} \mathrm{d}x \tag{4}$$

If strain gradients occur along the measuring-grid-axis of the strain gauge in the object to be measured, the strain gauge takes up the mean value of the strain occurring in the area of the active measuring-grid-length as an integrating instrument. It is shown schematically in Figure 6, according to the mean value theorem of the integral calculation.

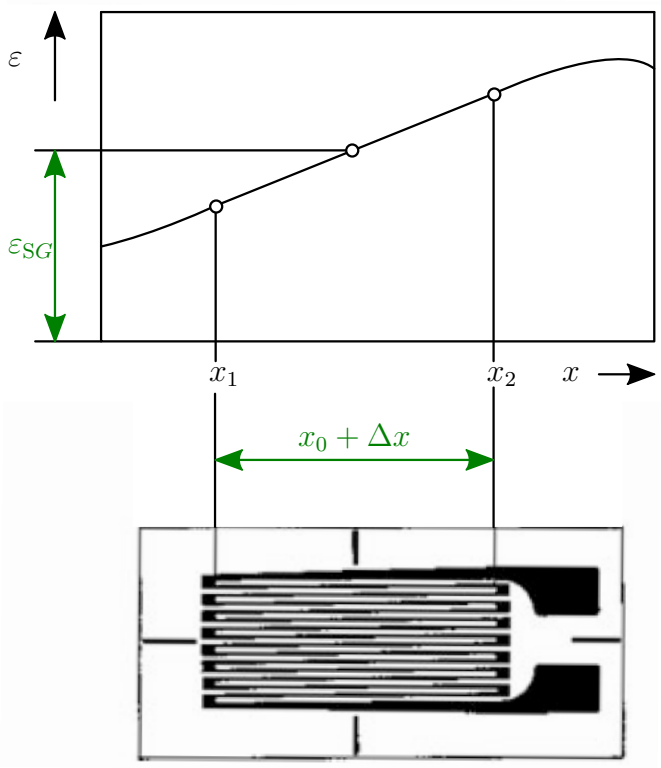

Figure 6: Integrated measurement of the strain curve over the active measuring-grid-length of the strain gauge. Figure taken from [6].

In Equation 4, $\varepsilon_{StrainGauge}$ is the strain amount recorded by the strain gauge and transformed into resistance change, x_1 and x_2 are the longitudinal coordinates limiting the active measuring grid length in the measuring direction. Thus the strain gauge measures the true strain. The true strain provides the correct measure of the final strain when deformation takes place in a series of increments, taking into account the influence of the strain path [13] on the contrast to the engineering strain which is expressed as the ratio of total deformation to the initial dimension of the material body. According to Equation 4 it should be mentioned that such an integration over each conducting path of the strain

gauge takes place. The term $\varepsilon(x)/(x_2 - x_1)$ accounts subjected to the following condition that no strain gradients occurs transverse to the measuring direction. So that the outcome of $\varepsilon_{StrainGauge}$ is the sum of the results of the integration over each conducting path. This consideration becomes more important if the longitudinal strain to be measured has a gradient transverse to the direction of measurement, as is the case, for example, at the edges of boreholes or notches. Different strains affect the individual conductors and the overall result $\varepsilon_{StrainGauge}$ is the arithmetic mean of the integration results of all conductors of the strain gauge. As the following equation describes.

$$\varepsilon_{StrainGauge} = \frac{1}{n} \sum_{i=1}^{n} \int_{x_2}^{x_1} \frac{\varepsilon_i(x)}{x_2 - x_1} \mathrm{d}x \tag{5}$$

Where i is the minimum number of conductors and n the number of conductors mounted on the strain gauge.

3.3. Sensitivity

By definition of [4] and translated, the sensitivity of a measuring element is the ratio of a change in its output quantity observed on the measuring element to the change in the input quantity causing it. The following descriptions are based upon [6]. The input value of the strain gauge is the strain ε captured by it, the output value is the change in resistance $\mathrm{d}R/R$ caused by the change in strain. The relationship between the two is described for strain gauges by the k-factor.

$$\frac{\mathrm{d}R}{R} = k\varepsilon \tag{6}$$

Experience shows that the k-factors given by the well-known manufacturers for their strain gauges are valid for the elastic deformation range with high reliability, but the k-factor need to be corrected if the yield point for the so-called high strain range is exceeded.

3.3.1. Temperature influences

During long journeys on a ship the temperatures can vary strongly. Differences in draft causes temperature differences on the outside of the ship's hull, since seawater around 0° C and cold arctic air or ice touches the hull. Steel is a good heat conductor and since the taken measurements only make sense in the area around the waterline, the strain gauge has to cope with temperature changes.
The k-factors specified for strain gauges by manufacturers generally apply to measurements at room temperature. Temperature changes may affect the k-factor, especially if the carrier material or adhesive is not suitable for the temperatures. In these cases the temperature-depended changes in mechanical properties of the carrier material and adhesive cause partially transmission of the strain from the component to the measuring grid. Thus no explicit k-factor exists. When strain gauges and adhesives are used, which are suitable for the expected temperatures, then the temperature-dependency of the k-factor can be determined at a measuring point. A quantitative example is shown in Figure 7.

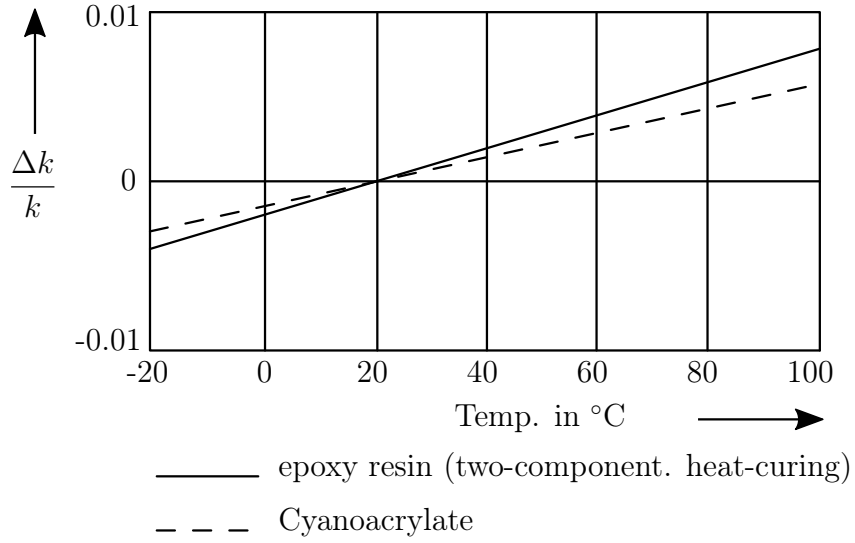

Figure 7: k-factor change over temperature. Figure taken from [6].

A linear correlation between the change in k-factor and the temperature within a certain temperature range is given by [6] as follows.

$$\frac{\Delta k}{k} = \alpha_k \Delta T \text{ or } k_T = k(1 + \alpha_k \Delta T) \tag{7}$$

In Figure 7 an example for the changes of the k-factor is given with a reference temperature of $T = 20°$ C. In addition, for the support material, polyimid, and for the wire material, constantan, is used. The wire winding length is 6 mm. As it can be seen the ratio is dependent on the adhesive used for the attachment. In Equation 7, ΔT is the temperature deviation from the reference temperature valid for the specified k-factor, k_T the k-factor at any temperature T within the linear range and α_k an experimentally determinable coefficient. Guidelines for the experimental determination of the temperature

dependence of the k-factor are given in [22].
However, temperature changes also cause resistance changes in the strain gauge, which additively overlap the strain-related resistance change. The considerations of resistance changes at changing temperatures to be made here, are only relevant for measurements where the temperature changes occur during the measurement process, i.e. a zero adjustment of the measurement setup at measurement temperature is not possible. For measurements that allow a zero adjustment of the measuring arrangement at measurement temperature, the temperature-related resistance changes are irrelevant. For full-scale, long term, measurements of ice loads on a ship's hull a zero balance is not possible, as the measurement temperature might change during the long measurement period.
The resistance changes occurring in the measuring point during temperature changes and the zero signal changes caused thereby can be described with three coefficients. The temperature-dependent change of the specific resistance α_R of the measuring grid material, the thermal coefficient of linear expansion α_M of the measuring grid and the thermal coefficient of linear expansion α_B of the component. Then the part of the resistance change of a strain gauge, at a measuring point, caused by changes in temperature can be measured with the following equation.

$$\left(\frac{\Delta R}{R_0}\right)_{\text{therm}} = \alpha_R \Delta T_{20} + k_T(\alpha_B - \alpha_M)\Delta T_{20} \tag{8}$$

With a reference temperature of 20° C.

$$\Delta T_{20} = T - 20^\circ\ \text{C} \tag{9}$$

To encounter temperature influences a dummy strain gauge within a Wheatstone bridge or a self-compensated strain gauge can be used. The author of [6], proposes to use self-compensated strain gauges in a bridge circuit when measurements are carried out at changing temperatures and the circumstances permit this.

3.3.2. Creep influences

If a strain gauge is stretched for a sufficiently long time, relaxation phenomena can occur in the carrier material which cause an enlargement of the transition zones at the measuring grid ends. The force opposite to the restoring force of the measuring grid from the carrier material decreases and the measuring grid can partially relax. This slow process is called creep of the strain gauge. Creep is of particular interest if measurements are to be taken over a longer period of time, at higher temperatures or very accurately. Figure 8 shows the phenomenon of strain gauge creep schematically.

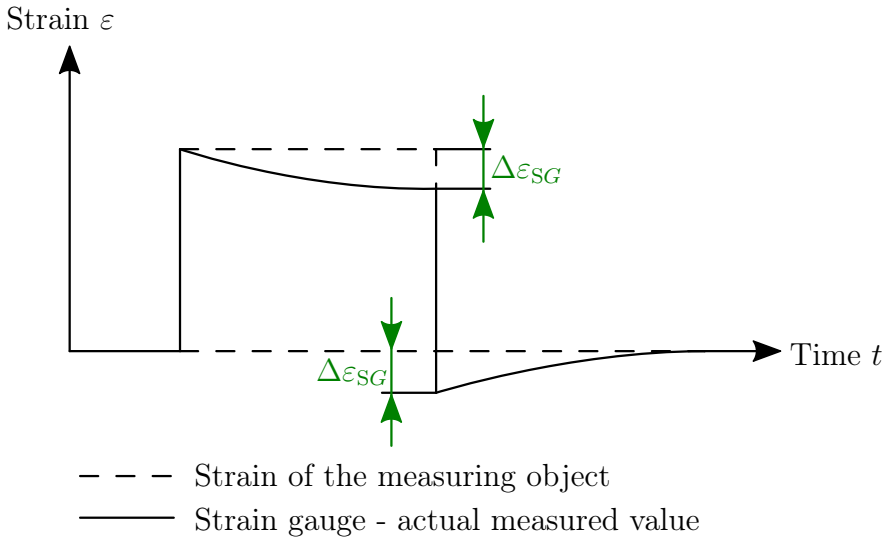

Figure 8: Creep-induced temporal change of the strain display of a strain gauge.

The diagram shows the strain of the measuring object and the strain recorded by the strain gauge installed on the measuring object. At time $t = 0$ the measuring object is loaded. The strain in the measured object and the measured strain increase synchronously to the same maximum value. While the strain in the object remains constant, the measured strain decreases slowly due to the creep of the strain gauge, resulting in a time-dependent strain difference $\Delta\varepsilon$. When after a longer period of time the measuring object is unloaded, the strain of the measuring object is reduced by the same amount as before the loading. However, since the strain of the strain gauge by the amount $\Delta\varepsilon$ was smaller than that one of the measuring object, after unloading the strain of the strain gauge by the amount $\Delta\varepsilon$ is below zero. Then it creeps after a certain period of time back to zero.
Several factors of creep can influence the measurements. Another influence for creep could be a permanent deformation caused by collision or by higher ice loads than accounted for in the ship design. The duration of the force acting can cause creep, which is not expected in measurements of ice-loads [17]. Besides, the temperature can influence the creep, the dimensions of the wire windings and the device under test itself can creep. For full-scale, long term measurements of ice loads on ship's hull are temperature changes and permanent deformations more expected then long-term forces in terms of creeping.

Mostly the strain gauge can adapt to the lengthening of the device under test. In addition, the longer the wire windings are the less creeping occurs. Over the time the relative strain $\frac{\Delta\varepsilon}{\varepsilon}$ is assumed to follow an exponential from with a certain limit. An example is shown in the next Figure 9.

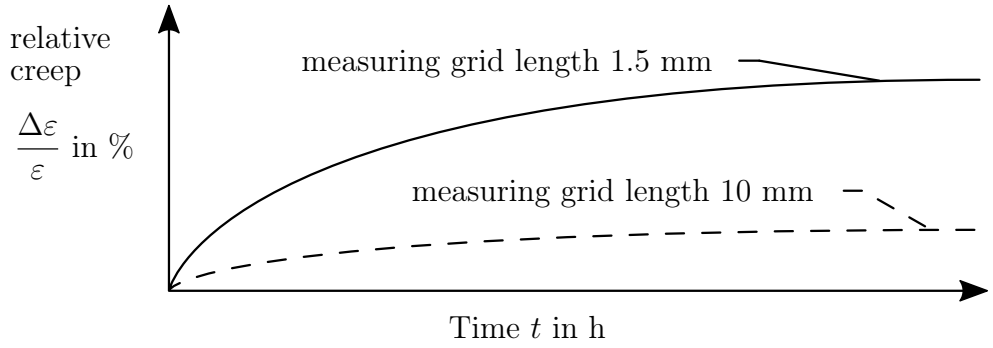

Figure 9: Creep curves of two foil strain gauges of different lengths.

As a total relaxation and therefore a deviation of 100 % is only seen at higher temperatures, at lower temperatures the relative strain stays reasonable low. The creeping problem of temperature lengthening can be resolved by placing a dummy strain gauge in the Wheatstone bridge.

3.4. Measurements of plane-shear states with strain gauges

It will be clear from Subsection 3.5 that the main approach to measure ice-induced loads on a ship's hull is by utilizing strain gauges for shear-strain measurements. The emphasis is on the word shear. From the measured shear-strains the ice loads can be determined. Thus, this Subsection will introduce to shear-strain measurements with strain gauges. The following descriptions are based upon [12].
The load on a specimen shown in Figure 10 leads to shear stresses and shear-strains in the specimen material.

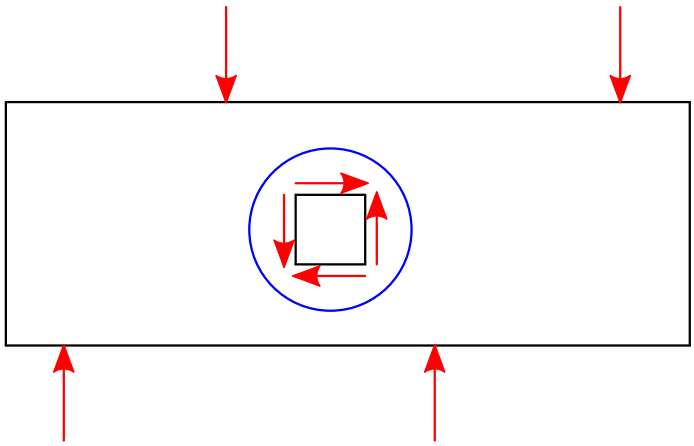

Figure 10: Shear loads applied to specimen.

An initially square element of the material, having vertical sides parallel to the direction of loading, is distorted by these stresses into a diamond shape as illustrated in Figure 11, where the distortion is greatly exaggerated for pictorial clarity.

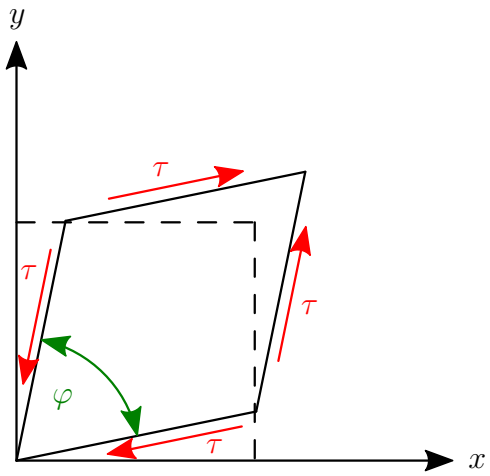

Figure 11: Enlarged shear deformation of an initially square element of the material. Zoom out Figure 10 marked in blue.

Besides the shear-strain is defined as the magnitude of the angular change of the original right angle of the element at the $x-y$ origin. Thus the following relationship can be made.

$$\gamma = \frac{\pi}{2} - \varphi \tag{10}$$

As mentioned before, normal strains cause dimensional changes in the measuring grid of a strain gauge, which then changes its electrical resistance. But pure shear-strains merely rotate the measuring grid, and do not cause the elongation or contraction necessary to vary the resistance. Through mechanic principles it can be shown, that shear-strains and normal strains are related, allowing strain gauges to provide a direct indication of shear-strain. In Figure 12 an array of two strain gauges, No. 1 and No. 2, are oriented at arbitrarily different angles with respect to an $x-y$ coordinate system which is arbitrarily oriented with respect to the principal axes.

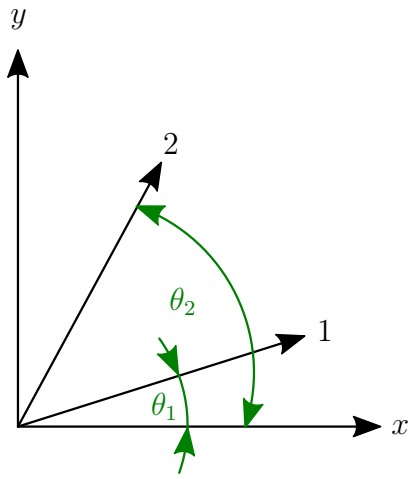

Figure 12: Arbitrarily oriented strain gauges in a biaxial strain field.

From the elementary mechanics of materials follows.

$$\varepsilon_1 = \frac{\varepsilon_x + \varepsilon_y}{2} + \frac{\varepsilon_x - \varepsilon_y}{2}\cos(2\theta_1) + \frac{\gamma_{xy}}{2}\sin(2\theta_1) \tag{11}$$

$$\varepsilon_2 = \frac{\varepsilon_x + \varepsilon_y}{2} + \frac{\varepsilon_x - \varepsilon_y}{2}\cos(2\theta_2) + \frac{\gamma_{xy}}{2}\sin(2\theta_2) \tag{12}$$

Subtracting Equation 12 from Equation 11 and solving for γ_{xy} results in the following equation.

$$\gamma_{xy} = \frac{2(\varepsilon_1 - \varepsilon_2) - (\varepsilon_x - \varepsilon_y)(\cos(2\theta_1) - \cos(2\theta_2))}{\sin(2\theta_1) - \sin(2\theta_2)} \tag{13}$$

For $\cos(2\theta_1) \equiv \cos(2\theta_2)$ the terms ε_x and ε_y vanish. Thus

$$\gamma_{xy} = \frac{2(\varepsilon_1 - \varepsilon_2)}{\sin(2\theta_1) - \sin(2\theta_2)} \tag{14}$$

Since the cosine function is symmetrical about the zero argument, and about all integral multiples of π, $\cos(2\theta_1) \equiv \cos(2\theta_2)$ when, for an arbitrary angle α,

$$\theta_1 + \alpha = -\pi/2,\ 0,\ \pi/2,\ \pi \ldots \frac{n\pi}{2} = \theta_2 - \alpha \tag{15}$$

If one now arranges the strain gauges in such a way that they are symmetrically oriented with their grid axes, e.g. to the x-axis as shown in Figure 13, then the following applies.

$$\theta_1 = -\theta_2 = \alpha \tag{16}$$

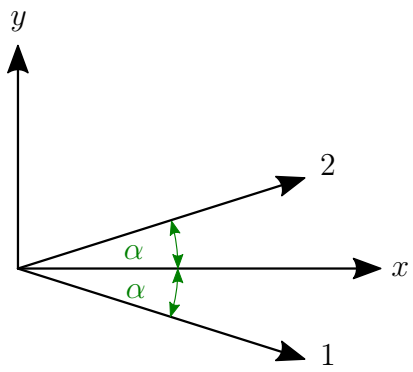

Figure 13: Defining x-axis as bisector of angle between gauge axes, $\gamma_{xy} = (\varepsilon_1 - \varepsilon_2)/\sin(2\alpha)$.

Which then leads to the following equation.

$$\gamma_{xy} = -\frac{\varepsilon_1 - \varepsilon_2}{\sin(2\theta_2)} = \frac{\varepsilon_1 - \varepsilon_2}{\sin(2\theta_1)} = \frac{\varepsilon_1 - \varepsilon_2}{\sin(2\alpha)} \tag{17}$$

Now, when the two gauges are 90° apart, the denominator of Equation 17 becomes unity and the shear-strain along the bisector is numerically equal to the difference in normal strains. Thus, a conventional two-gauge 90° rosette constitutes an ideal shear half bridge because the required subtractions, $\varepsilon_1 - \varepsilon_2$, is performed automatically for two gauges in adjacent arms of the bridge circuit. When the gauge axes of a two-gauge 90° rosette are aligned with the principal axes, the output of the half bridge is numerically equal to the maximum shear-strain.
It should be kept in mind that with the shear-bridge described above, the indicated shear-strain exists along the bisector of any adjacent pair of gauge axes, and it is not possible to determine the maximum shear-strain or the complete state of strain from any combination of gauge outputs unless the orientation of the gauge axes with respect to the principal axes is known. In general, when the directions of the principal axes are unknown, a three-gauge 45° rectangular rosette can be used. Since the maximum shear-strains are not of interest a conventional two-gauge 90° rosette is sufficient and is therefore more economical from a cost standpoint of view.

3.5. Theory of ice-induced load measurements using strain gauges

In this Subsection the theory of the applicability of strain gauges for ice load measurements on a ship's hull will be described. Furthermore, the possibilities of measurements, the taken considerations and the used measurement approach will be pointed out. Starting with the theory of the applicability of strain gauges for ice load measurements on a ship's hull. All insights are based on the bachelor's thesis [20] and the dissertation [17]. Mainly there are two different approaches to measure ice-induced loads on a ship's hull. The first approach is the indirect structural strain measurement and the second one is the direct measurement of the contact pressure or load. In this thesis the indirect structural strain measurement will be investigated. In the indirect method, a possibility is to measure the shear-strains between two locations on the frame. Another possibility is to measure the compressive strain on the frame normal to the shell or to determine the local loading by measuring the bending strain at the flange. Then the external loading is determined from the load-strain relation of the built structure which can be determined by a finite element analysis, by a calibration pull or through an analytical approach which offers a much rougher solution. Figure 14 shows how the shear-strains in the web frame change and Figure 15, 16 and 17 show how the strains in the web of the frame change at a specific location, when moved away from the loading point.

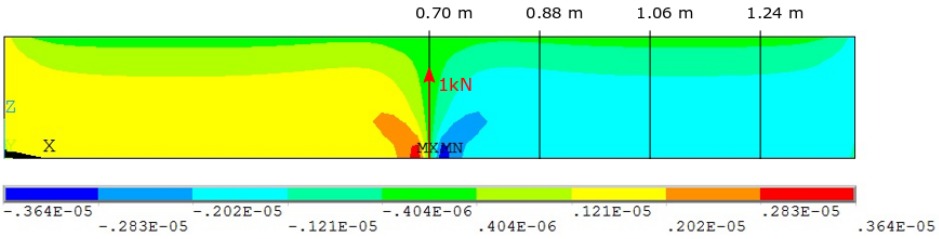

Figure 14: The shear-strain γ_{xz} in the web of the frame.

In Table 3 the parameters are listed which defines the topology and the material data of the model.

Table 3: Geometry and material data for the investigation of the strain behavior.

Description	Variable	Size	Unit
Frame length	L	1.400	m
Frame spacing	s	0.400	m
Web height	h_w	0.200	m
Web thickness	t_w	0.019	m
Plate thickness	t_p	0.020	m
Young's modulus	E	209	GPa
Poisson's ratio	ν	0.3	[-]

The shear force, i.e. the ice-induced load, acting between the two locations equals the change in the shear force between the two locations. This relationship can be shown through looking at the elastostatics of a simply loaded beam. So when shear forces are of interest, the structure is instrumented at least at two locations. The strain in the z-direction ε_z decreases rapidly outside the contact area, as it can be seen in Figure 16. Thus the loads that have a direct effect at the location of the strain gauge can be determined. As it can be seen from Figure 15, 16 and 17 measurements based on the difference in the shear-strain are less sensitive to the variation in the location of the load along the transverse frame than measurements based on the compressive strain normal to the hull. Thus, the strain normal to the shell structure is a function of the amplitude, location with respect to the sensor, and the extent in the horizontal and vertical directions. When looking globally on the ship, x is the vertical direction and y the horizontal direction. When it comes to the shear-strain difference, the determined loading is not sensitive to the height and location of the loading on the frame, as long as the loading has an effect between the gauges. Figure 17 shows that outside the contact location, the shape of shear-strain curve over the web of the frame remains relatively constant in the x-direction of the frame. However, the shear-strains within the frame are sensitive to the location and length of the loading the y-direction. As the measurements based on the shear-strain difference are the least sensitive to the load height and locations and thus they are reliable in giving the load acting between the sensors, this thesis focuses on the measurements based on shear-strain difference.

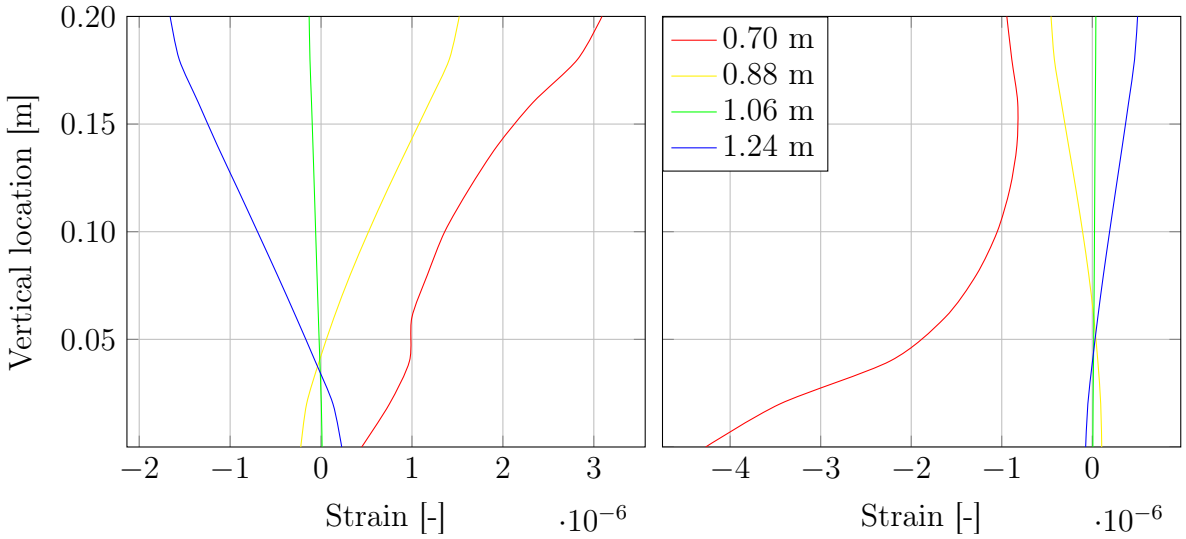

Figure 15: ε_x over the web height measured at different spots along the frame.

Figure 16: ε_z over the web height measured at different spots along the frame.

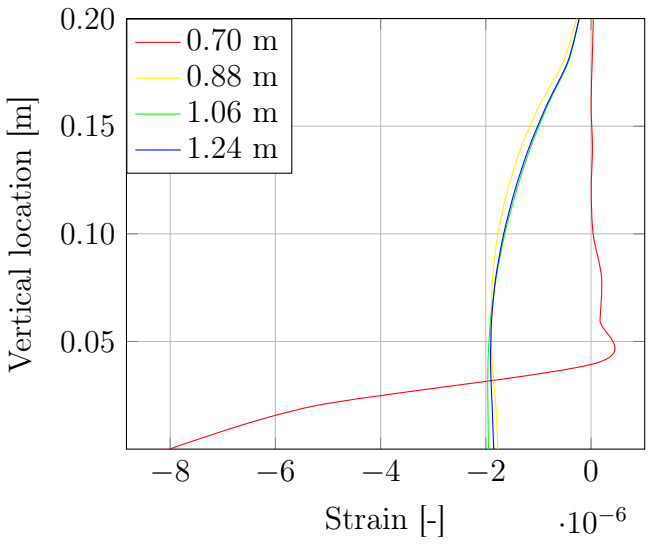

Figure 17: γ_{xz} over the web height measured at different spots along the frame.

For measurements based on shear-strain difference it is assumed that the pressure distribution within the ice load patch acts uniform. Also, in order to determine the load-strain relation of the structure an assumption about the location and shape of the ice has to be made. Commonly these are kept constant through the measurements but in reality they vary. Besides the variation in long-term measurements is assumed to result from the variation in ice conditions and properties, from the ice failure mechanism and from the ship operations. For example, one can imagine that the vertical location of the contact is affected by the draught and the movement of the ship. In the case of full-scale measurements, additional variation in the measured loading arises from the measurement techniques that are applied [17].
For indirect strain gauge measurements of ice loads on a ship's hull mainly the two following strategies exist:

1. The measurement on the plate between the frames, this was conducted e.g by [9].

2. The measurement on frames with strain gauges at the end of the frame, close to the next higher supporting structure like [18] did or distributed along the frame like [8] did.

A combination of these strategies is possible as well. The detection of small, confined load-impacts can only be seen with high resolution, whereas the overall force per frame can be derived from the shear strains at the ends of the frame with much less strain gauges needed. This is a good ratio of reducing the number of measurement inputs versus reduction of measurable information [20]. This thesis focuses on the second strategy with strain gauges at the end of the frame. Since the chosen set-up measures the structural response, the structural ability to transfer loading should be understood.

3.5.1. Structural response

The load acts through the shell as a shear force on the frame [17]. The reason for that is, due to the ability of the structure to transport loading. One part of the loading is carried by the loaded frame and the other part is transported to the adjacent frames by the hull plating connecting the frames [17]. The amount of loading carried by the directly loaded frame depends on the topology of the frame structure. This will be shown in the Section 3.5.2. When the loading affects a frame directly, the shear force on the frame is a result of the deflection. The adjacent frame to the loaded frame undergoes deflection and rotation. The shear-strain resulting from the deflection is a function of the z-coordinate and remains constant over the thickness and the shear-strain resulting from the torsion is a function of the y-coordinate and varies linearly over the thickness. As the resulting shear-strain is a sum of these actions, the side of the frame affects the measured loads [18]. Figure 18 shows the composition of shear-strain in the web frame.

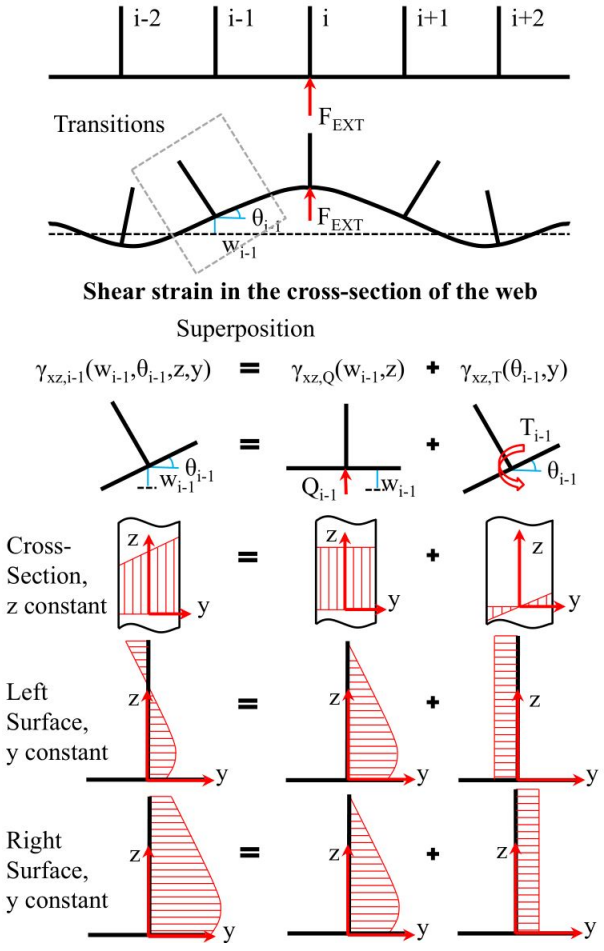

Figure 18: The shear-strain in a cross-section resulting from the displacement in the z-direction and the rotation around the x-axis and the resultant shear-strain on both sides of the frame. Figure taken from [18].

3.5.2. Relationship between the topology of the structure and the load transfer

In order to understand how the load transfer of a ship structure correlates to its topology, an analytical grillage model will be derived. All insights are based on [10] and [18]. It is assumed that the loading $q_i L$, caused by external loading F, acts directly on the frame and induces bending to it. The adjacent frames, having the same direction, are assumed to be connected to this frame by a transverse beam. This transverse beam models the plate between the frames. Besides, the frames support the transverse beam, i.e. the plate with vertical loads $q_i L$ and torsions T_i. An assumption is, that the beams are considered long and slender and they behave according to the *Euler-Bernoulli* kinematics. In Figure 19 the plate-frame system is depicted.

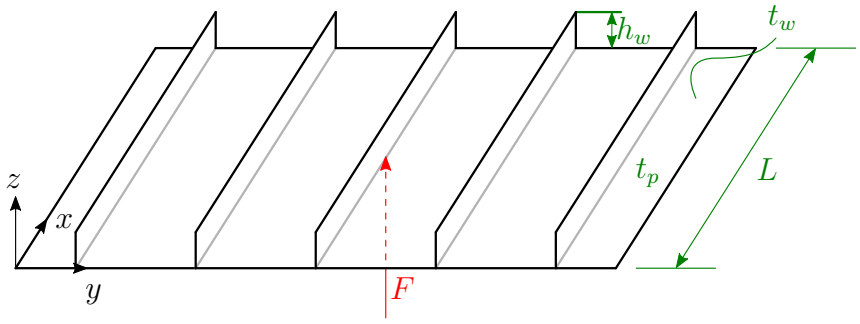

Figure 19: Plate-frame system.

This frame system contains five frames which are connected to one plate. The corresponding idealized grillage model is depicted in Figure 20, where the plate is modeled as a transverse beam. It should be mentioned that it is only one of the three possible loading conditions, when taken the symmetry into account. The external loading F induces bending to the plate and the frames respond with shear forces $q_i L$ and torsions T_i.

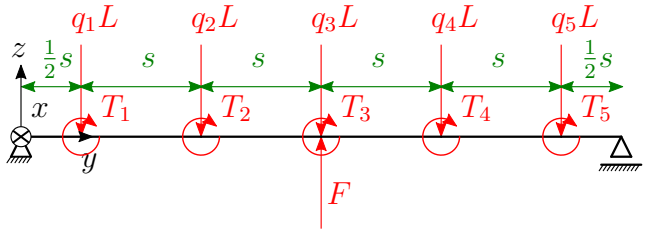

Figure 20: Idealized plate system.

In Figure 21 the frame, which is loaded directly by the external force, is depicted. The corresponding model looks as follows.

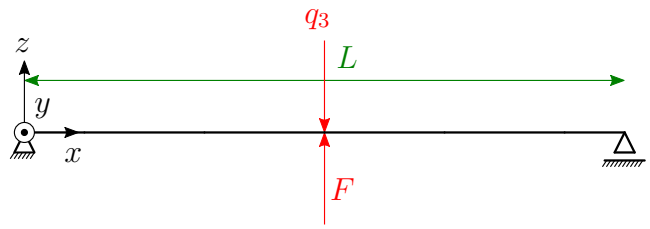

Figure 21: Idealized frame system, directly loaded.

In Figure 22 one of the four frames, which is not loaded directly by the external force, is depicted. Here, it is the second frame and the corresponding model looks as follows.

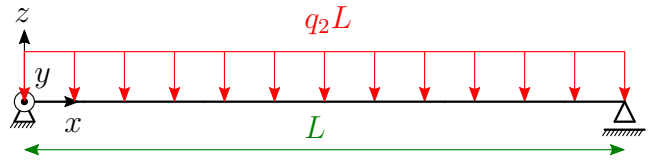

Figure 22: Idealized frame system, not directly loaded.

As it can be seen from Figure 21 and Figure 22, the loading on the loaded frame is taken as a point load and as a line load on the adjacent frames. For the other adjacent frames the model looks similar. It is considered to calculate five frames with a frame spacing s, giving the total breath.

$$B = 5 \cdot s \tag{18}$$

The web thickness is t_w and the web height is h_w. The grillage length is equal to the frame length L. In addition it is assumed, that the frames and the plate consist of the same material with a Young's modulus E. Furthermore the plate thickness is t_p and the grillage is assumed to be simply supported to model the maximum load distribution to the adjacent frames. In order to calculate the unknown shear forces $q_i L$ and torsions T_i, the equilibrium conditions for the plate

$$\sum F_z = 0 \tag{19}$$

$$\sum M_x = 0 \tag{20}$$

and the frames,

$$\sum F_z = 0 \tag{21}$$

$$\sum M_y = 0 \tag{22}$$

have to be solved. Then the equation for the deflection and rotation of the plate are obtained by integrating the moment equation,

$$D L_e \frac{\mathrm{d}^2 w_{\mathrm{Pl}}(y)}{\mathrm{d}y^2} = -M_x(y) \tag{23}$$

where D is the bending stiffness of the plate,

$$D = \frac{Et_p^3}{12(1-\nu^2)} \tag{24}$$

and L_e is the effective length of the plating. It is assumed that the effective length is equal to the real length of the plate [18]. Equation 23 can be derived from the equilibrium conditions for the plate-frame system, how [18] did. Following assumptions have to be made in order to get the right derivation. Pure bending is assumed, because it leads to uncoupling the moments in the x- and the y-direction. Besides, the stiffness of the frame is assumed significantly larger than that one of the plate. The assumption of pure bending can be applied for lateral loading when the deflections are small in comparison to the width of the plate [21]. It is highlighted that the approximation is very rough, based on assumption of small curvature of the plate in the x-direction. In order to solve the integration constants of Equation 23, boundary conditions have to be applied. In the same way, the deflection and rotation for the frames along the x-axis $w_{\mathrm{Fr}}(x)$ are obtained.

$$EI = \frac{\mathrm{d}^2 w_{\mathrm{Fr}}(x)}{\mathrm{d}x^2} = -M_y(x) \tag{25}$$

Where I is the second moment of area of the frame, with the effective breath of the plate being taken into consideration. In order to solve the shear forces $q_i L$ and the torsions T_i, the plate displacements and rotations at the frame locations have to be set equal with the displacement and rotation of the corresponding frame at the mid span of the frame. For the rotation of the frames the following applies.

$$\theta_{\mathrm{Fr},i}\left(\frac{L}{2}\right) = \frac{T_i L}{2GI_T} \tag{26}$$

Thereby is I_T the torsion constant. For the case depicted in Figure 20, following equations results when proceeding as described before.

$$q_3 = \frac{25k^2(20-126u+125u^2)+320k(10-81u+145u^2)+4096(1-9u+19u^2)}{k_0}F \tag{27}$$

$$q_2 L = q_4 L = \frac{8k[15k(4-30u+33u^2)+64(2-18u+35u^2)]}{k_0}F \tag{28}$$

$$q_1 L = q_5 L = \frac{8k[5k(4-30u+37u^2)+192(u-6u^2)]}{k_0}F \tag{29}$$

$$\frac{T_2}{s} = \frac{T_4}{s} = \frac{2k(8+5k)[5k(-1+u)+32(-1+5u)]}{k_0}F \tag{30}$$

$$\frac{T_1}{s} = \frac{T_5}{s} = \frac{k(8+5k)[5k(-2+3u)-64u]}{k_0}F \tag{31}$$

Where k is

$$k = \frac{DL^4}{EIs^3}, \tag{32}$$

and u is

$$u = \frac{DL^2}{GI_T s}. \tag{33}$$

For the nominator following applies.

$$\begin{aligned} k_0 =& 25k^3(4 - 6u + u^2) + 5k^2(356 - 2166u + 2129u^2) + 64k(82 - 645u + 1093u^2) \\ &+ 4096(1 - 9u + 19u^2) \end{aligned} \tag{34}$$

From these equations following observations can be made. Assuming that the bending stiffness EI and the torsional stiffness GI_T going against infinite, so that k and u become zero, the following applies for Equation 28.

$$q_3 = F \tag{35}$$

Thus all the force is taken by the middle frame. When neglecting only the torsion of the frames, u becomes zero. This results in a load distribution from the loaded frame to the adjacent frames depending in the parameter k. Figure 23 presents the ratio of the load taken by the adjacent frames and the loaded frame as a function of k.

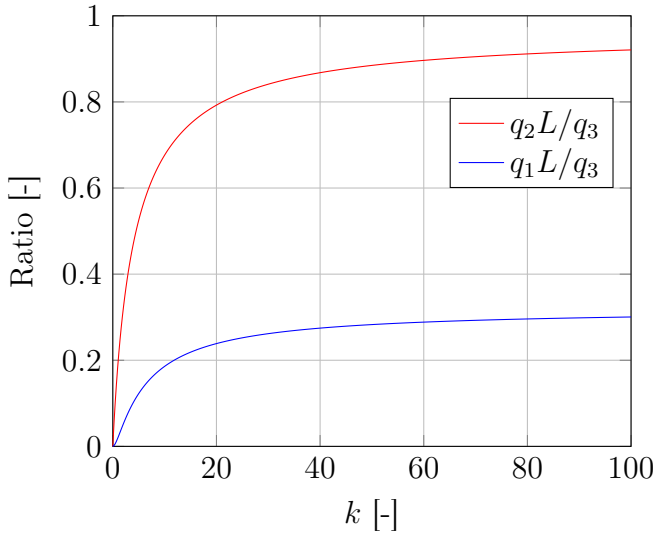

Figure 23: The ratio of loading on the loaded frame and adjacent frames as a function of k when u is zero.

When k increases the ratio q_2L/q_3 approaches to 0.96 and the ratio q_1L/q_3 approaches to 0.32. This shows that in ice-load measurements, where the load magnitude and the length are from interest, the response of the adjacent frames should be accounted. The art's state of determining the load carried by the loaded frame is by using finite element analysis [17], in order to calculate an influence coefficient matrix.

3.6. Determination of the ice-load from the shear-strain measurements using FEA

When a ship breaks through ice, the ice-structure interaction induces a load on the side plating [18]. The load can go over several frame spacings in the horizontal direction or acts only on a single frame spacing. In this cases it is considered that the transverse frames carry the majority of the loading. As the ice load acts on a frame as an external shear force and is concentrated in the vertical direction in first-year ice conditions [14], the ice load can be determined by measuring shear-strains at the ends of the frame [18]. The response of the adjacent frames can be accounted in the full-scale measurements by introducing an influence coefficient matrix (ICM). This concept assumes that a proportionality between the exerted load and the measured shear-strains exists, where a proportionality factor is to be determined. One might say, that this proportionality factor behaves like the stiffness matrix $\boldsymbol{K}$. The assumption is that the structure behaves only elastic, which is not true in reality when i.e. certain magnitude of loads are exceeded. The distribution of the loading $\boldsymbol{F}$ and shear-strain $\boldsymbol{\gamma}$ can be accounted for in the measurements with an ICM $\boldsymbol{a}$ defined from the relation:

$$\boldsymbol{F} = \boldsymbol{a}\Delta\boldsymbol{\gamma} \tag{36}$$

The ICM is determined using the inverse $\boldsymbol{c}$:

$$\boldsymbol{a} = \boldsymbol{c}^{-1} \tag{37}$$

$$\boldsymbol{c}_{ij} = \Delta\boldsymbol{\gamma}_i \boldsymbol{F}_j \tag{38}$$

Where $\boldsymbol{a}$ is the influence coefficient matrix, $\boldsymbol{c}$ is the inverse matrix of $\boldsymbol{a}$. $\Delta\gamma_{i...m}$ is the shear-strain difference measured on the frame i, m is the number of the instrumented frames and F_j is the external force exerted on the frame j. The diagonal terms of the influence coefficient matrix define the force-strain relation of the frame under loading and the off-diagonal terms determine the response of the adjacent frames. Looking back at Figure 23, the graphs represent the behavior of the off-diagonal terms in the ICM with respect to the diagonal terms as a function of k. The difference in the shear-strain between the ends of the frame $\Delta\boldsymbol{\gamma}$, is determined by calculating the shear-strain occurring at the lower and upper parts of the frame with FEA and then calculating the difference.

$$\Delta\gamma = \gamma_{\text{upper}} - \gamma_{\text{lower}} \tag{39}$$

In order to determine the coefficients of the inverse influence coefficient matrix the unit load principle is used.

$$\begin{bmatrix} c_{i,i} & c_{i,i+1} & \dots & c_{i,n} \\ c_{i+1,i} & c_{i+1,i+1} & \dots & c_{i+1,n} \\ \dots & \dots & \dots & \dots \\ c_{n,i} & c_{n,i+1} & \dots & c_{n,n} \end{bmatrix} \begin{pmatrix} 1 \\ 0 \\ \dots \\ 0 \end{pmatrix} = \begin{pmatrix} \Delta\gamma_i \\ \Delta\gamma_{i+1} \\ \dots \\ \Delta\gamma_n \end{pmatrix} \tag{40}$$

This means that one frame at a time will be loaded by a force in the middle between the two strain gauges and then the response of the frames, in terms of the shear-strains,

will be measured. The force should be high enough to take into account the influence on the adjacent frames, but it should also be possible to apply this force in reality by means of a calibration pull. In the Appendix A, Figure 54 to Figure 58, the load cases for the determination of the inverse ICM are shown.

4. Accuracy of the ICM

The finite element model, presented in Figure 24, was created in *Ansys 18.2* using *SHELL181* elements. The model serves for the investigation of the measurement accuracy of an exemplary instrumented ship structure at local loads using strain gauges. In particular this Section deals with the question which accuracy can be obtained with the influence coefficient matrix. The model consist of 10,500 elements which builds a structured quadrilateral grid. The element size is 0.02 m x 0.02 m, which is one tenth of the frame height. The author of [11] recommends to use at least 3 elements over the web height. The coordinate system can be seen at the lower right end of Figure 24. It is a Right-Hand-System, where the x-coordinate points towards the direction of the frames and the y-coordinate points towards the direction of the plate. The z-coordinate points towards the expected direction of the external force.

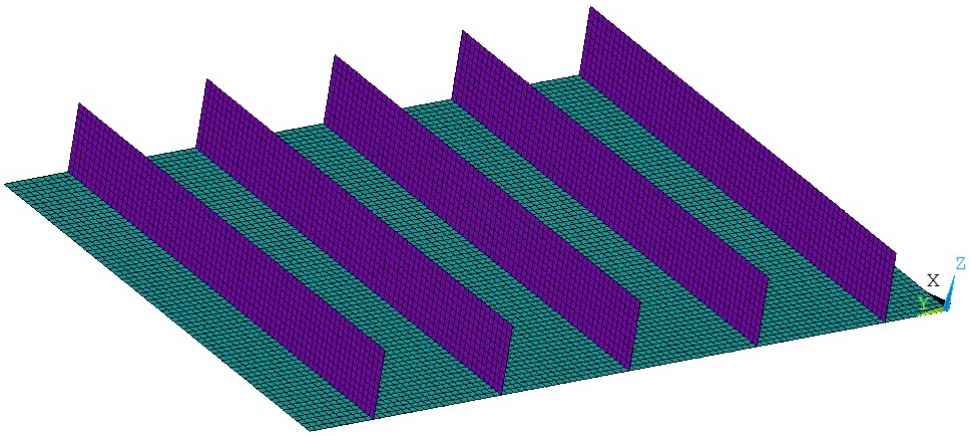

Figure 24: Idealized FEM model.

The same model is used in Section 3.5 and the geometry and material data are shown in Table 4.

Table 4: Geometry and material data for the investigation of the ICM.

Description	Variable	Size	Unit
Frame length	L	1.400	m
Frame spacing	s	0.400	m
Web height	h_w	0.200	m
Web thickness	t_w	0.019	m
Plate thickness	t_p	0.020	m
Young's modulus	E	209	GPa
Poisson's ratio	ν	0.3	[-]

The static analysis is conducted with *Ansys 18.2*. The brief description of the static

analysis is based on [11]. In a static analysis, displacements, stresses, strains and forces in structures are calculated that are attributable to loads that do not contain any significant inertia or damping effects. Static loads and boundary conditions are assumed, which means, that the loads and the response of the structure are constant over the time. The load types that can be applied in a static analysis are externally acting forces and pressures, temporally constant inertia forces, predefined displacements and temperatures. A static analysis can be either linear or nonlinear. All types of nonlinearities are permissible in *Ansys 18.2* such as large displacements, plasticity, creep, hardening by prestressing, contact elements, hyperelastic elements and others. The procedure for a static analysis consists of the following three main steps.

1. Creation of the model (preprocessing)
2. Apply the loads and calculate the solution (solution)
3. Evaluation of the results (postprocessing)

Now after the model is created the boundary conditions have to be considered, according to the main steps. The boundary condition will be applied at the nodes of the elements. For this purpose four planes will be defined in Table 5.

Table 5: Boundary planes

	Plane 1	Plane 2	Plane 3	Plane 4
at	$x = 0$	$x = L$	$y = 0$	$y = 5s$

In order to investigate the influence of boundary conditions on the solution two cases of different boundary conditions will be studied. In Table 6 and Table 7 the following cases are used for the investigation.

Table 6: Boundary conditions, Case 1

Plane 1	Plane 2	Plane 3	Plane 4
$u_x = u_z = 0$	$u_z = 0$	$u_y = u_z = 0$	$u_z = 0$
$\varphi_x = 0$	$\varphi_x = 0$	$\varphi_y = 0$	$\varphi_y = 0$

Table 7: Boundary conditions, Case 2

Plane 1	Plane 2	Plane 3	Plane 4
$u_x = u_y = u_z = 0$	$u_x = u_y = u_z = 0$	$u_x = u_y = u_z = 0$	$u_x = u_y = u_z = 0$
$\varphi_x = \varphi_y = \varphi_z = 0$	$\varphi_x = \varphi_y = \varphi_z = 0$	$\varphi_x = \varphi_y = \varphi_z = 0$	$\varphi_x = \varphi_y = \varphi_z = 0$

Further on, in order to calculate and afterwards to investigate the influence coefficient matrix, a unit load of 1 kN is chosen. As mentioned before in the Subsection 3.6, the unit load will be applied in the middle between the two strain gauges and then the response of the frames will be measured.

In the Figure 25 an exemplary shear-strain gauge arrangement on a transverse frame is displayed.

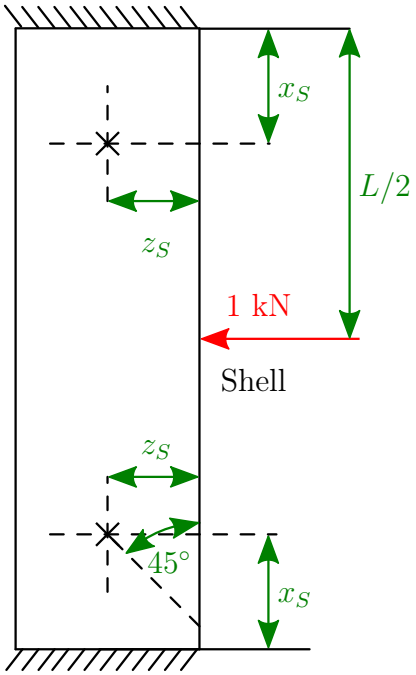

Figure 25: Exemplary shear-strain gauge arrangement on a transverse frame.

For the investigation $x_S = 0.3$ m and $z_S = 0.02$ m is chosen, by means that the shear-strains are measured at these node location. The investigation approach is as follows. First, a boundary conditions case is chosen, which is followed by the selection of the measuring approach. This means that a side of the frame is chosen where the shear-strains are measured. It is also possible to measure the shear-strains on both sides of the frame. Third, the influence coefficient matrix will be calculated. As last, within two loops along the plate in an interval of 0.02 m in x- and y-direction, a point load or a pressure load is applied. At the respective points of the frame, the shear-strains are measured and then the external load is determined using the influence coefficient matrix. For the further process the components of the load vector $\boldsymbol{F}$ are added up. Now the determined value can be compared with the applied load. With the determined force either the absolute or the relative error is calculated. When the true value is γ and the measured or inferred value γ_0 then the relative error is defined by

$$\delta\gamma = \frac{\Delta\gamma}{\gamma} = \frac{\gamma_0 - \gamma}{\gamma} = \frac{\gamma_0}{\gamma} - 1 \tag{41}$$

where $\Delta\gamma$ is the absolute error [2].

In Table 8 the investigation approaches are listed.

Table 8: Investigation approaches.

Approach	Boundary condition case	Load type	Measuring technique
1	1	point	one sided
2	2	point	one sided
3	2	point	one sided, other side
4	2	pressure patch	one sided
5	2	point	double sided

As it can be seen form this table the chosen boundary condition case, the load type and the measuring technique for each approach is listed. This will give a better overview over the next subsections.

4.1. First approach

The first approach is as follows. The boundary conditions, Table 6, Case 1 will be applied and then the first influence coefficient matrix will be calculated. The shear-strains are measured on the top side of the frames which means on that surface, whose surface normal points in opposite direction as of the y-axes. The influence coefficient matrix is shown in Equation 42.

$$\boldsymbol{a} = \begin{bmatrix} -332.23 & -6.93 & -3.32 & -0.50 & -0.21 \\ 69.41 & -258.55 & -9.29 & 1.02 & -0.54 \\ -22.41 & 41.96 & -257.95 & 9.93 & 0.77 \\ 7.61 & -14.57 & 41.62 & 258.48 & 8.69 \\ -2.30 & 4.86 & -14.34 & -41.83 & 252.84 \end{bmatrix} \cdot 10^3 \text{ [kN]} \tag{42}$$

When looking at the first row of the influence coefficient matrix, it can be seen that the responds of the fifth frame, which is shown in the fifth column, is relatively low. This is the reason why often only four frames are instrumented, like [18] did. The positions of the point loads were determined with this influence coefficient matrix, which resulted in a relative error of less than 5 % of an 1 kN point load. The results are shown in Figure 26. The crossing points of the grid indicate the positions of the strain gauges. It can be seen that only few 5 % cases exist within the instrumented area. In addition, it turns out that these cases lie more in the direction of the top side of the frames, where the shear-strains are measured from.

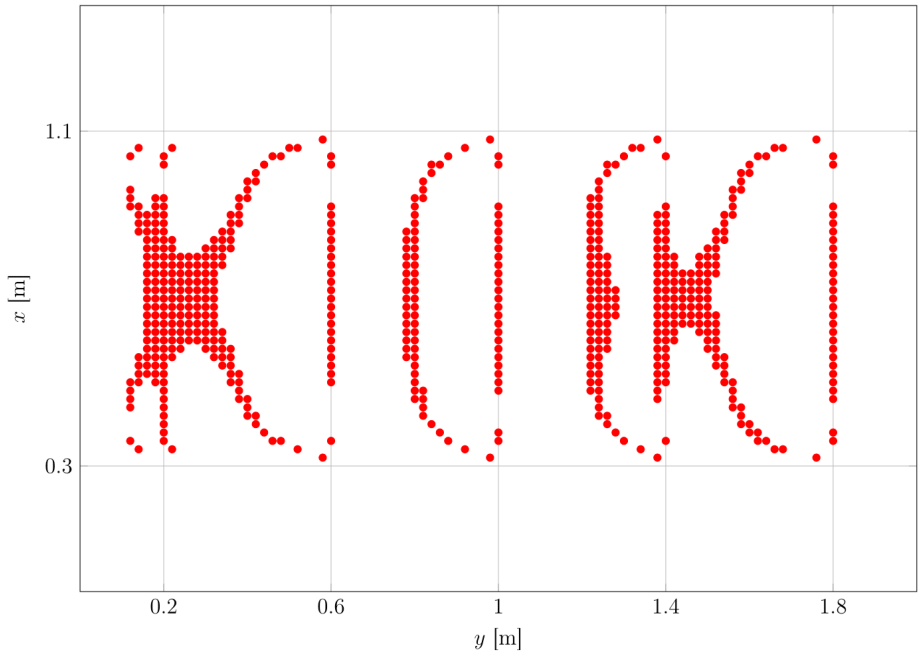

Figure 26: Load locations which resulted in relative error of less than 5 % of an 1 kN point load, simply supported case, measurements on the top side of the frames.

4.2. Second approach

In order to exclude an influence of the boundary conditions on the solution, the same procedure of Subsection 4.1 is carried out with the boundary conditions from Table 7, Case 2. The influence coefficient matrix is shown in Equation 43.

$$\boldsymbol{a} = \begin{bmatrix} -375.59 & 1.68 & -1.01 & -0.57 & -0.09 \\ 59.51 & -255.46 & -7.67 & 0.04 & -0.15 \\ -18.33 & 31.50 & -253.23 & 7.91 & 0.01 \\ 5.59 & -10.10 & 30.84 & 253.16 & 7.52 \\ -1.69 & 3.36 & -10.68 & -33.49 & 265.43 \end{bmatrix} \cdot 10^3 \text{ [kN]} \tag{43}$$

This time the boundary conditions are stricter, i.e. all degrees of freedom are suppressed. This means that local loads should lead to larger deformations. This can be seen, when comparing the first row of Equation 42 with the first row of Equation 43. The first frame carries more of the load and thus the responds of the adjacent frames decays more the further they lie from the loaded frame. However, when looking on the results in Figure 27 no big difference can be made when comparing them to Figure 26, which suggests that the boundary conditions have little effect on the solution. In the further course of this Section, only the boundary conditions of Table 7, Case 2 will be applied.

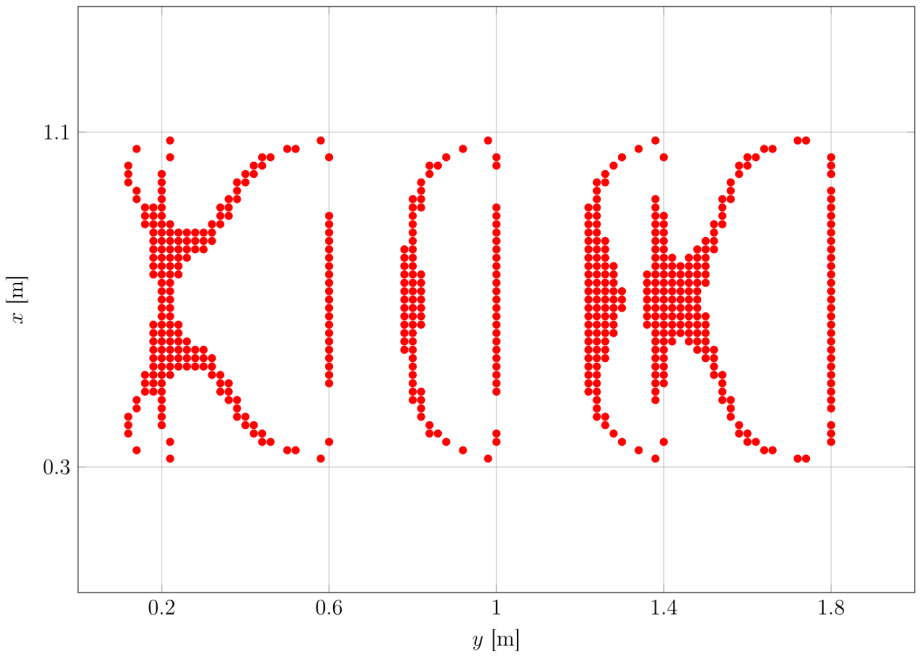

Figure 27: Load locations which resulted in relative error of less than 5 % of an 1 kN point load, fixed supported case, measurements on the top side of the frames.

4.3. Third approach

For demonstrative purposes the last approach, Subsection 4.2, was calculated repeatedly only this time the shear-strains were measured on the bot side of the frame so that the surface normal points in the same direction as of the y-axes. The influence coefficient matrix is shown in Equation 44.

$$\boldsymbol{a} = \begin{bmatrix} -265.43 & 33.49 & -10.68 & -3.36 & 1.69 \\ -7.52 & -253.16 & 30.84 & 10.10 & -5.59 \\ -0.01 & -7.91 & -253.23 & -31.50 & 18.33 \\ 0.15 & -0.04 & -7.67 & 255.46 & -59.51 \\ 0.09 & 0.57 & -1.01 & -1.68 & 375.59 \end{bmatrix} \cdot 10^3 \text{ [kN]} \tag{44}$$

Similarities between the ICM of Equation 43 and Equation 44 can be seen. The first row of Equation 43 equals the last row of Equation 44 when changing the first column with the last and the second with the forth and then changing its sign respectively. The same applies for the second row of Equation 43 and the forth row of Equation 44 and for the third row of Equation 43 and the third row of Equation 44. Besides, one can see, that Figure 28 equals Figure 27 only it is rotated.

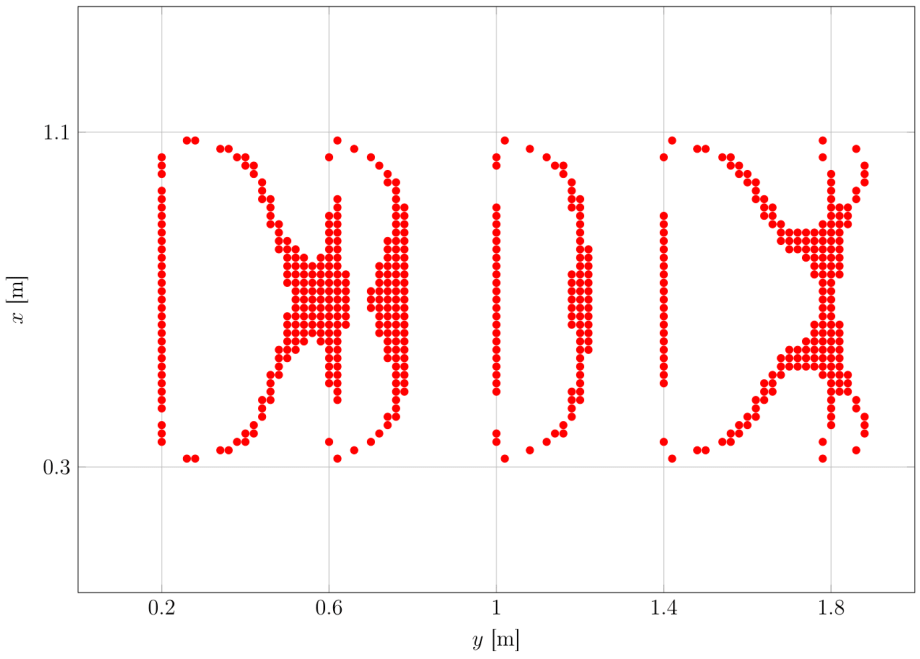

Figure 28: Load locations which resulted in relative error of less than 5 % of an 1 kN point load, fixed supported case, measurements on the bot side of the frames.

4.4. Forth approach

In this approach it will be investigated whether there is a difference between a point load of 1 kN at one node or a pressure which equals a point load of 1 kN, in relation to the influence coefficient matrix and to the applied method. For this purpose a pressure of

$$\frac{1000 \text{ N}}{0.02 \text{ m} \times 0.02 \text{ m}} = 2.5 \text{ MPa} \tag{45}$$

will be applied. The influence coefficient matrix is shown in Equation 46.

$$\boldsymbol{a} = \begin{bmatrix} -379.55 & 1.99 & -1.05 & -0.59 & -0.09 \\ 61.77 & -256.20 & -7.68 & 0.05 & -0.15 \\ -19.23 & 32.51 & -253.85 & 7.94 & 0.01 \\ 5.92 & -10.52 & 31.80 & 253.78 & 7.55 \\ -1.82 & 3.54 & -11.13 & -34.57 & 266.37 \end{bmatrix} \cdot 10^3 \text{ [kN]} \tag{46}$$

There is a marginal difference between the ICM of Equation 43 and Equation 46. The frame which is directly loaded takes less of the load and thus the load is transferred more to the other frames due to the fact that the load is not that concentrated. In order to get more information relative error areas will be created instead of only looking at cases below 5 %. Relative error areas between 0 % - 10 % were marked in blue, areas between 10 % - 25 % were marked in green, 25 % - 50 % were marked in yellow and everything over 50 % were marked in red. The results are shown in Figure 29. From Figure 29 it can be deduced that outside the instrumented area, relative errors of more than 50 % are to be expected under the given conditions. On the other hand, relative errors of less than 50 % can be expected within the instrumented area. The instrumented area is 1.28 m^2.

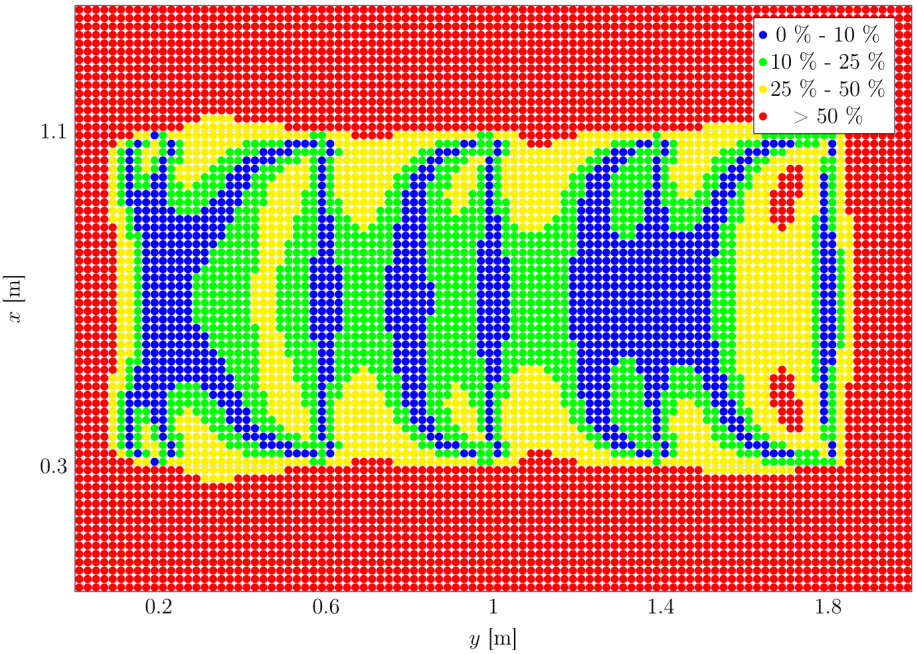

Figure 29: Relative error areas of an 1 kN pressure load, fixed supported case, measurements on the top side of the frames.

In order to get better comparisons of the data within the instrumented area, a proper probability distributions have to be chosen. If for example the data shows a *Normal distribution*, handy values like the mean value μ and the standard deviation σ can be computed. Thus, one have not to look at the complete data but rather can make statements based on these values which in turn are based on the chosen probability distribution. It is stated that these values have a kind of summarizing function and will be used as such. In statistics, a probability distribution is a mathematical function that provides the probabilities of occurrence of different possible outcomes in an experiment [16]. Without going too deeply into the subject of statistics and probability distributions, the author describes in the following the topics *null hypothesis* and *Kolmogorov–Smirnov test* (KS test) briefly. The KS test is a statistical test for the correlation of two probability distributions. This test returns a decision for the *null hypothesis* that the data comes from the chosen distribution, against the alternative that it does not come from such a distribution. The result is $h = 1$ if the test rejects the null hypothesis at the 5 % significance level α, or otherwise the result is $h = 0$. The *null hypothesis* gets rejected when the p-value is less then the significance level α. In addition, the *null hypothesis* states that there is no specific connection between the compared data. Thus if the KS test rejects the *null hypothesis*, so that $h = 1$, there is a connection between the data. Besides, the smaller the p-value the more the result speaks against the *null hypothesis*. The relative error of the data of the instrumented area of Figure 29 is grouped and plotted so its probability can be visualized in Figure 30.

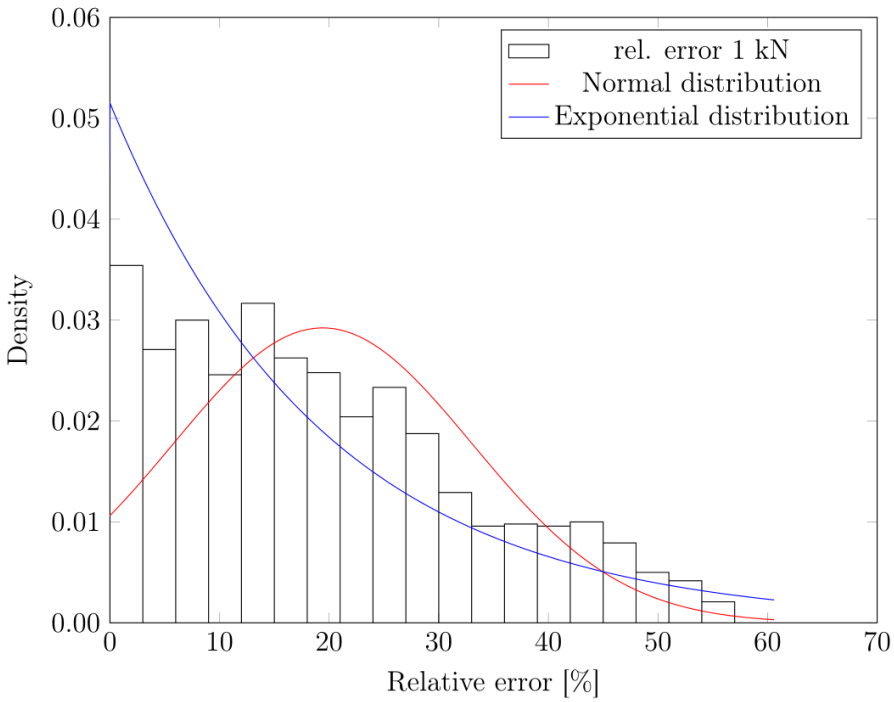

Figure 30: Probability density function of the relative error of an 1 kN pressure load from the instrumented area of Figure 29, pressure area 0.02 m × 0.02 m.

Many KS test were conducted, but in order to keep the statistical part of the thesis short only the honorable mentions are discussed. For the *Normal distribution* the KS test rejects the *null hypothesis*, so that $h = 1$ with $p =$ 2.866e-17, the *Exponential distribution* and the *Rayleigh distribution* were rejected as well with $p =$ 3.141e-36 and $p =$ 6.335e-60 respectively. In other words these distributions have a connection between the data. In Figure 30 the *Normal distribution* function and the *Exponential distribution* function are plotted. Although after the KS test all three distribution functions are applicable, some distribution functions fit better to the dataset than others. The *Rayleigh distribution* gives the smallest p-values however the author states that the *Generalized extreme value distribution* fits the dataset most. In the case *Normal distribution* versus *Exponential distribution* the *Exponential distribution* fits the dataset the most as it can be seen from Figure 30. In order to see if a distribution function fits to the dataset the cumulative probability function is shown in Figure 31, which gives a better overview.

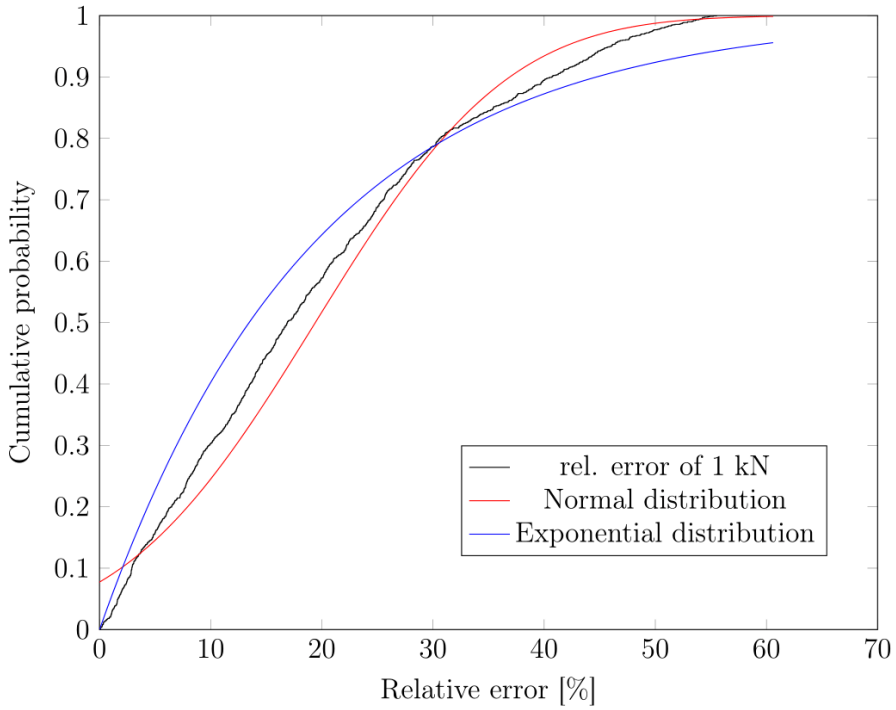

Figure 31: Cumulative distribution function of the relative error of an 1 kN pressure load from the instrumented area of Figure 29, pressure area 0.02 m × 0.02 m.

For the further course of this thesis the author uses the *Normal distribution*, since the parameters are more common and more pictorial.
For comparison purposes for the further approaches, a brief description of the arithmetic mean value μ and the standard deviation σ will be given. The mean value is calculated as follows.

$$\mu = \frac{1}{n} \sum_{i=1}^{n} x_i \tag{47}$$

Here, the arithmetic mean is the sum of all relative errors divided by their number [2]. In addition the standard deviation is an useful value, which is calculated as follows.

$$\sigma = \sqrt{\frac{\sum_{i=1}^{n} (x_i - \mu)^2}{n}} \tag{48}$$

The standard deviation is a measure that is used to quantify the amount of variation of a set of data values [2]. So now to be more precise, the instrumented area gives in the mean relative errors of

$$\mu_{icm4} = 19.411\ \% \tag{49}$$

and the standard deviation of the relative errors is

$$\sigma_{icm4} = 13.646\ \%. \tag{50}$$

4.5. Fifth approach

Now both sides of the frame will be instrumented, what the result is, that shear-strains from other sources than shear forces will be neglected. In order to achieve this, the shear-strains on both sides are measured at the same location and the mean value is then calculated. Figure 18 proves the calculation graphically. This should enhance the accuracy of the applied method. So this time the shear-strains are measured on both sides of the frames and the calculation is done using point loads. The method using point loads resulted in a shorter calculation time and achieved similar results compared to the method using pressure patches of 0.02 m $\times$ 0.02 m, as it can be seen in the last approach. The influence coefficient matrix is shown in Equation 51.

$$\boldsymbol{a} = \begin{bmatrix} -313.35 & 20.92 & -5.38 & -1.48 & 0.34 \\ 20.83 & -257.63 & 12.47 & 3.76 & -1.41 \\ -5.53 & 12.50 & -256.44 & -12.50 & 5.53 \\ 1.41 & -3.76 & 12.47 & 257.63 & -20.83 \\ -0.34 & 1.48 & -5.38 & -20.92 & 313.35 \end{bmatrix} \cdot 10^3 \text{ [kN]} \tag{51}$$

Following observation can be made. The first row of Equation 51 equals its last row when changing the first column with the last and the second with the forth and then changing its sign respectively. The same applies for the second and the forth row. In addition the third row is symmetric to the third column when changing the signs about the third column on one side. Further the third column is symmetric to the third row. A relative error area plot can be seen in Figure 32.

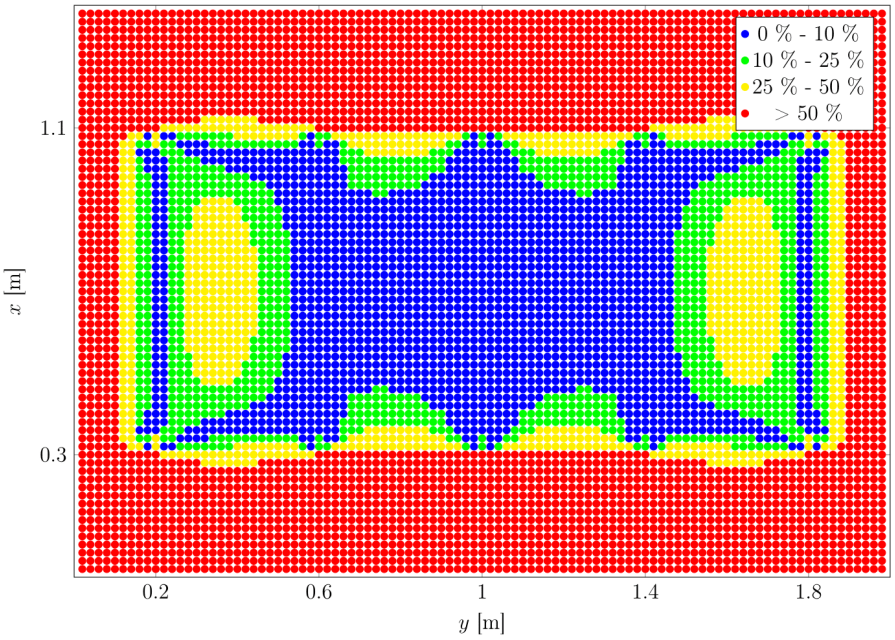

Figure 32: Relative error areas of an 1 kN point load, fixed supported case, measurements on both sides of the frames.

As the ICM of Equation 51 indicated the plot shows a symmetrical behavior. In addition, there is an area of 0.4048 m^2, which is $\approx$ 31.6 % of the instrumented area, that has an accuracy of less than 10 %. Further the instrumented area gives in the mean relative errors of

$$\mu_{icm5,rel} = 14.0828\ \% \tag{52}$$

and the standard deviation of the relative errors is

$$\sigma_{icm5,rel} = 12.726\ \%, \tag{53}$$

which shows that with double instrumented frames a much higher accuracy is achieved. Besides the relative error area plot a plot of the absolute error is shown in Figure 33 as a heat map.

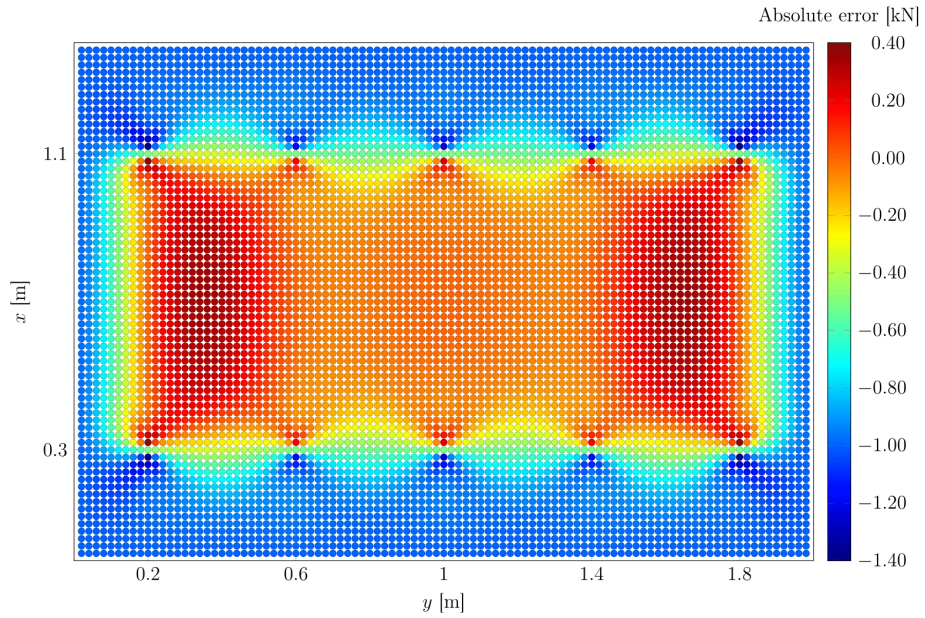

Figure 33: Absolute error heat plot of an 1 kN point load, fixed supported case, measurements on both sides of the frames.

On the legend one can see that the absolute error in the range 0 is colored orange. This plot shows perfectly that within the instrumented area the load is in general overestimated and beyond the instrumented area the load is in general underestimated. In addition the instrumented area gives in the mean absolute errors of

$$\mu_{icm5,abs,1kN} = -0.00794821 \text{ kN} \tag{54}$$

and the standard deviation of the absolute errors is

$$\sigma_{icm5,abs,1kN} = 0.189659 \text{ kN}. \tag{55}$$

In Figure 34 the probability density function of the 1 kN case of the absolute error is shown.

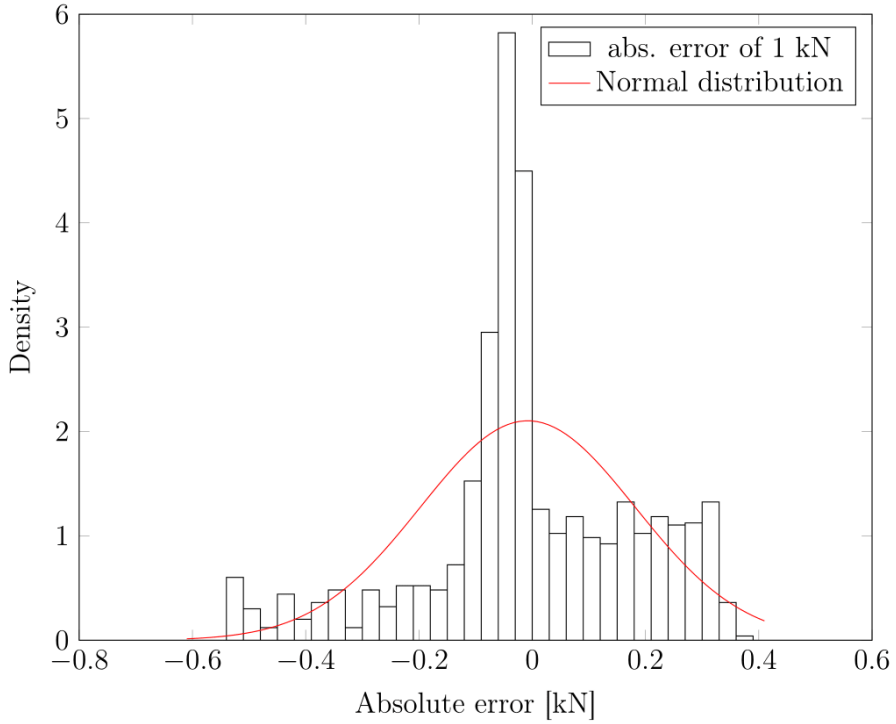

Figure 34: Probability density function of the absolute error of an 1 kN point load from the instrumented area of Figure 33.

As it can be seen from Figure 34, the absolute error has a more normal-like distribution. The cumulative distribution function of the Figure 33 is shown in the Appendix A, Figure 62. Besides, in order to maintain the readability of this thesis all probability distribution functions and all cumulative distribution functions which are not available in this and other sections are shown in the Appendix A, Figure 59 to Figure 77.

The same procedure as for the 1 kN point load, was conducted with a 100 kN point load, where *Ansys 18.2* started to calculate nonlinear. The reason behind this was to check if the results of the method changes when conducting the calculation in the nonlinear region. The absolute error of this procedure is shown in Figure 35 and it can be seen that no difference can be made to Figure 33. The calculation time tripled in this case.

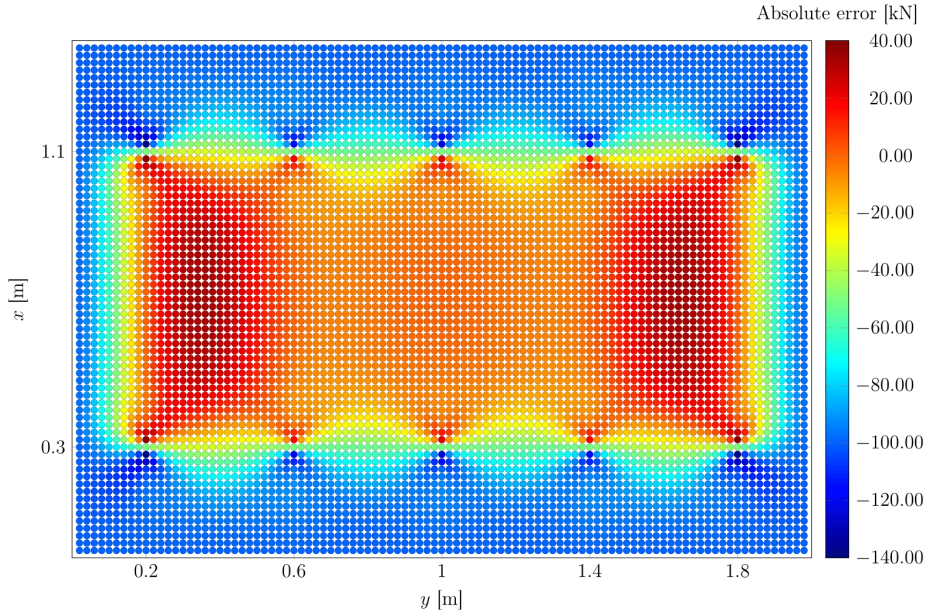

Figure 35: Absolute error heat plot of an 100 kN point load, fixed supported case, measurements on both sides of the frames.

The instrumented area gives in the mean absolute errors for the 100 kN case of

$$\mu_{icm5,abs,100kN} = -0.921494 \text{ kN} \tag{56}$$

and the standard deviation of the absolute error is

$$\sigma_{icm5,abs,100kN} = 18.926 \text{ kN}. \tag{57}$$

Relatively speaking, the calculation of the 100 kN point load gives marginal higher mean values at the nearly same relative standard deviation.

5. Determining the load location

From the previous investigations it should be clear, that the location of the load is of big interest, because loads outside the instrumented area have an impact on the instrumented area. It was shown, that the point loads outside the instrumented area are in general underestimated. Thus these loads could vanish under the noise of the measurement system. Nevertheless in this Section an approach to determine the load location is presented.
In order to minimize the complexity of the measurement system, an attempt is made to determine the load location with the existing strain gauges of the load measurement. A simply loaded beam is presented in Figure 36, where the load location ξ is unknown. Q_1 and Q_2 are the reaction shear forces which are measured using the existing strain gauges.

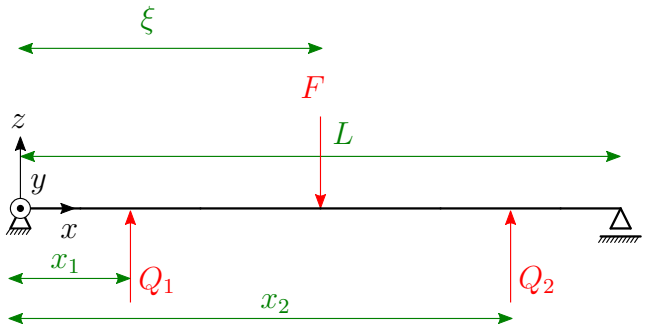

Figure 36: Simple Beam - Point load at any location ξ.

The shear force curve of the beam consists of the following two functions.

$$Q(x) = -F + F\frac{\xi}{L} \quad \text{for} \quad 0 < x \leq \xi \tag{58}$$

$$Q(x) = -F + F\frac{\xi}{L} + F \quad \text{for} \quad \xi < x \leq L \tag{59}$$

Here it is already evident that the load must always lie between the two measuring points. Thus for Q_1 and Q_2 follows.

$$Q_1 = \left(\frac{\xi}{L} - 1\right) F \tag{60}$$

$$Q_2 = \frac{\xi}{L} F \tag{61}$$

And thus the load location can be determined as follows.

$$\xi = \frac{Q_2 L}{Q_2 - Q_1} \quad \text{for} \quad x_1 < x \leq x_2 \tag{62}$$

The Equation 62 shows, that the determined location does not depend on the magnitude of the point load. In addition, outside the instrumented area $Q_1 = Q_2$ applies and so no location can be calculated. In reality a location can be calculated, by differences of

two nearly equal numbers but this location is beyond being reasonable. The accuracy for the pure shear force measurement is greatest for the double instrumentation, since shear effects from non shear loads are nearly neglected. Thus it only makes sense to use this instrumentation method in order to measure the location of the load. Now that it is clear how to measure the location of the point load at one frame the question arises how do we apply this method for a plate-frame system of five frames. The author choses the following approach. At first the magnitude of the load is calculated using the influence coefficient matrix. As a result one gets a load vector $\boldsymbol{F}$ with five rows, depending on the number of instrumented frames. In the next step the frames which are subjected to the highest loads will be chosen. At these frames the location of the load will be calculated. For this purpose a point load of 1 kN is chosen. The results of the loading location calculation is presented in Figure 37.

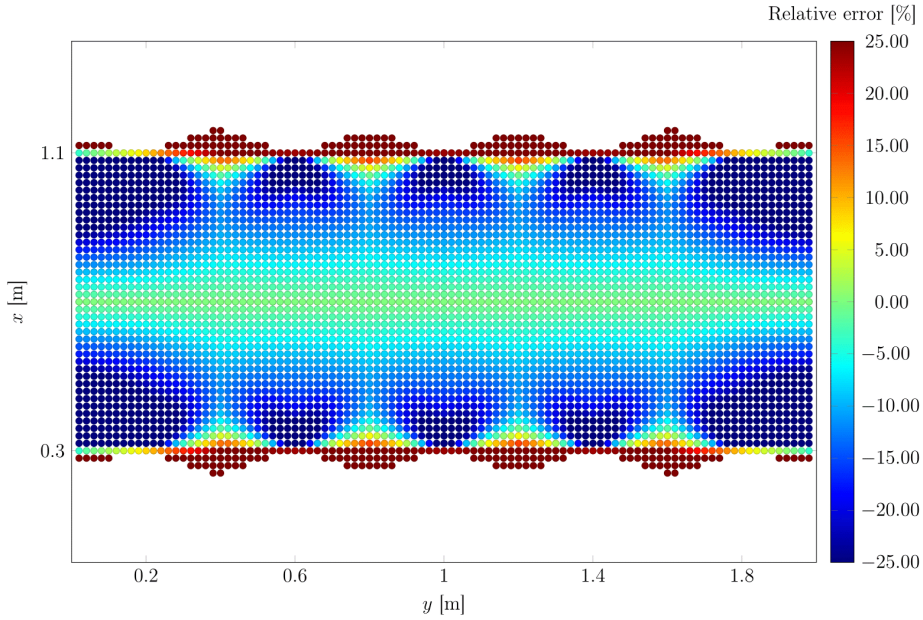

Figure 37: Relative error of the calculated load locations.

The instrumented area gives in the mean relative errors for the load location of

$$\mu_{icm,loc} = -9.425\ \% \tag{63}$$

and the standard deviation of the relative absolute is

$$\sigma_{icm,loc} = 11.886\ \%. \tag{64}$$

It can be seen, that in horizontal direction an overall relative error of $|\delta\xi| \approx 20$ % is achieved with this method. Worth to be mention is, that the location of the loads at $L/2$ could be determined exactly. Due to the symmetry at $x = 0.7$ m and $y = 1.0$ m on both axes, the Figure 38 shows a quarter of the plate field of Figure 37. However, the error is displayed in the whole area. In Figure 38 it can be seen that outside the instrumented area in vertical direction the position is overall greatly overestimated. Furthermore the positions in the corners of the plate are greatly underestimated.

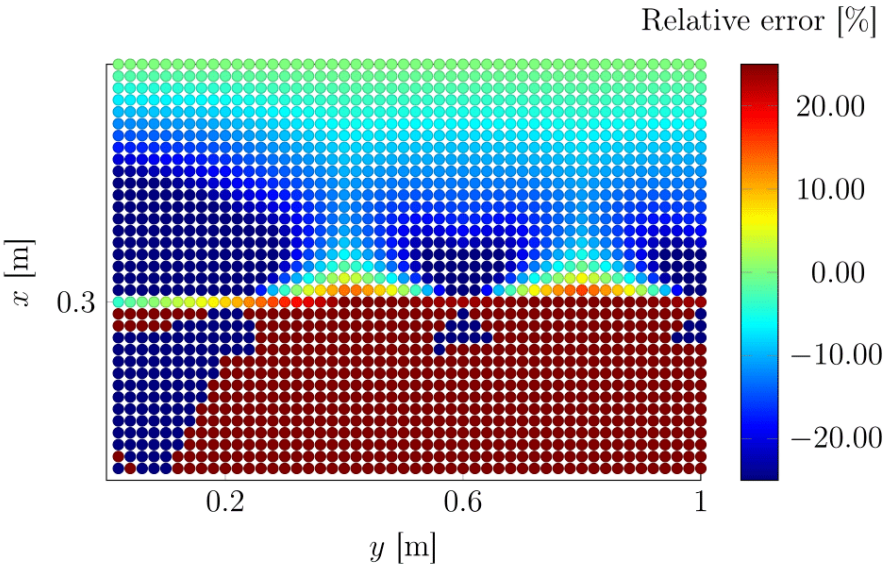

Figure 38: Relative error of the calculated load locations, zoom on a quarter.

6. Accuracy of line loads

In Section 4 the accuracy of the influence coefficient matrix in regards to point loads was discussed. It turns out when instrumenting a frame on both side the best accuracy can be achieved. The reason for that is, that the main approach assumes a proportionality between the exerted force and the measured shear force. In order to measure the shear-strains induced by shear forces, the double instrumentation gives the best solution since shear-strains of non shear loads are nearly neglected.
In Section 5 an approach was shown in order to determine the load location. Hereby the already existing strain gauges for the load measurements were used for the determination of the location. The approach is based on a simply loaded beam analogy and produces relatively precise results near the middle of the frames.
This Section comes closer to the reality. In reality the ice acts on an area of the ship's shell with a pressure. The following is taken into account. It is assumed that the ice acts uniform on the ship's hull. Therefore the design height $h = 0.3$ m of the area actually under constant ice pressure at any particular point of time is chosen. This corresponds to the design height of an ice class IA ship regarding to the *Finnish-Swedish Ice Class Rules* of 2008, [19]. The length of the pressure area is 0.2 m which corresponds to the half length of the frame spacing. For the unit load 100 kN is chosen. This results in a pressure of

$$\frac{100 \text{ kN}}{0.2 \text{ m} \times 0.3 \text{ m}} = 1.67 \text{ MPa}. \tag{65}$$

In Figure 39 the absolute error reached with the method is shown.

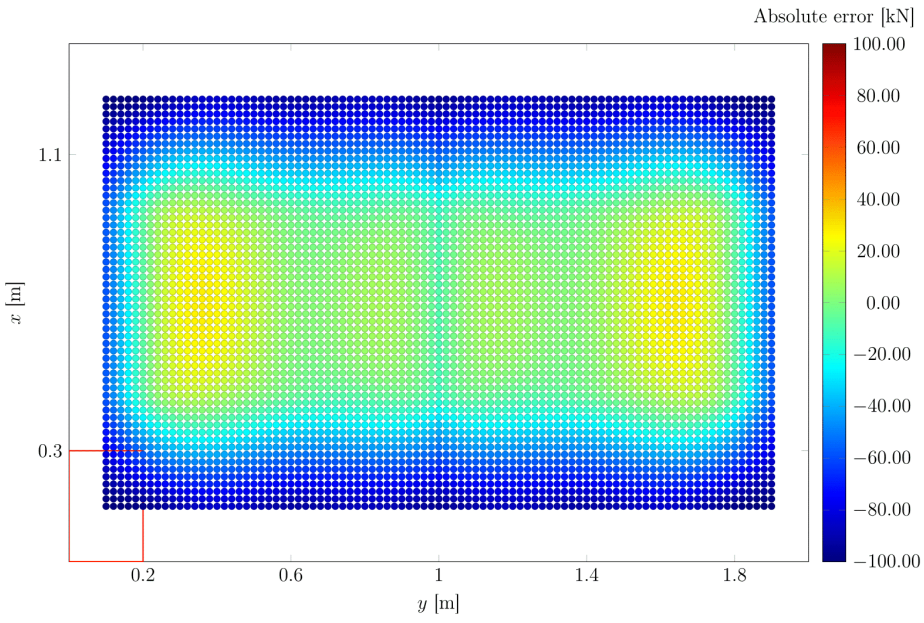

Figure 39: Absolute error, pressure area 0.3 m × 0.2 m.

In the lower left corner a red rectangle is shown which demonstrates the pressure area.

Thus the location of the points are the location of the center of the pressure area. As in Figure 35 with the point loads, Figure 39 shows an acceptable accuracy within the instrumented area. Furthermore the area between the second and the forth frame tends to be nearly uniform in terms of accuracy, both for Figure 35 and Figure 39. Outside the instrumented area the load is underestimated as in the investigation with the point loads. It is also noticeable that between the first and second and between the fourth and fifth frame the absolute error generally seems to be slightly larger. This could also be seen in the point loads. The instrumented area gives in the mean absolute errors for the load of

$$\mu_{icm,1.67MPa} = -4.0507 \text{ kN} \tag{66}$$

and the standard deviation of the absolute errors is

$$\sigma_{icm,1.67MPa} = 18.275 \text{ kN}. \tag{67}$$

In Figure 40 the relative error of the calculated load locations is displayed. Again it shows that the location at $L/2$ tends to be exact as with point loads. It also seems that the accuracy around the mid line is slightly better compared to the point loads in Figure 37.

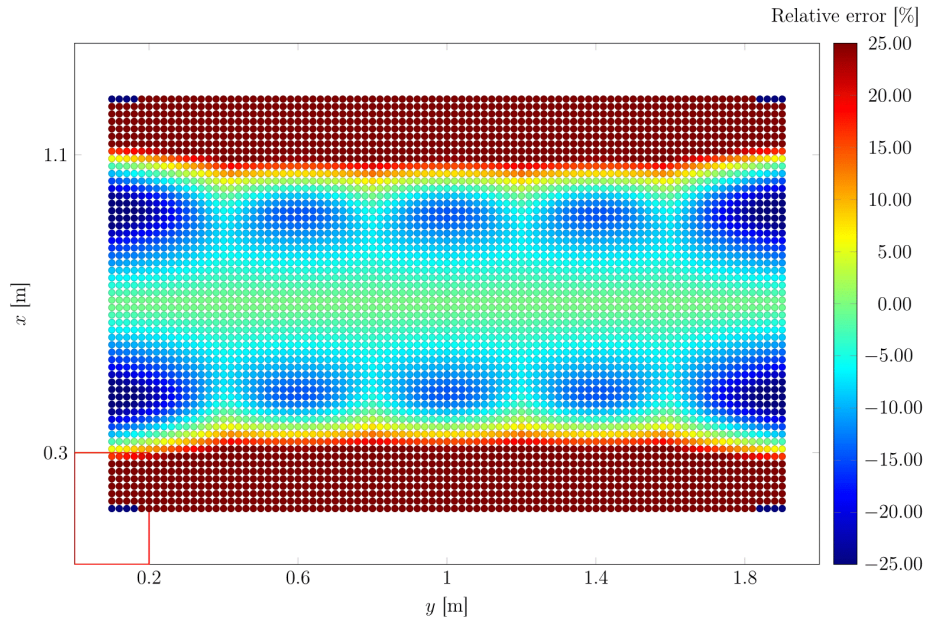

Figure 40: Relative error of the calculated load locations, pressure area 0.3 m × 0.2 m.

The instrumented area gives in the mean relative errors for the load location of

$$\mu_{icm,1.67MPa,loc} = -3.201 \text{ \%} \tag{68}$$

and the standard deviation of the relative errors is

$$\sigma_{icm,1.67MPa,loc} = 9.479 \text{ \%}. \tag{69}$$

In addition to consideration the accuracy of the ICM and the load position determination, the standard deviation of the load vector was also determined. An attempt is made to use the standard deviation to determine the load length. The approach is presented in Section 7. In Figure 41 the standard deviation of the load vector $\boldsymbol{F}$ is shown. It can be seen that along the frames a homogeneous area in the form of an ellipse is formed. In addition, along the third frame the standard deviation of the load vector $\boldsymbol{F}$ seems to be nearly constant.

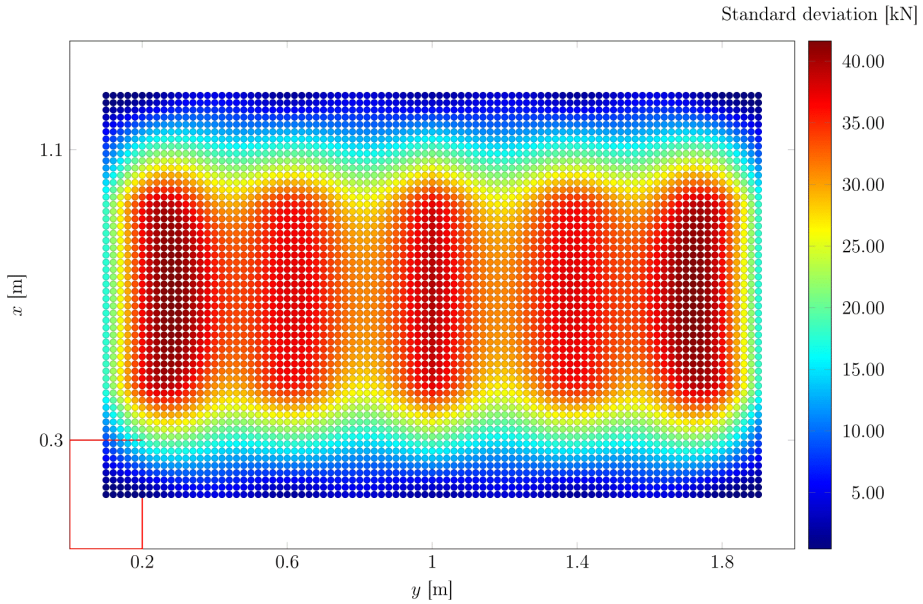

Figure 41: Standard deviation of the load vector $\boldsymbol{F}$, pressure area 0.3 m $\times$ 0.2 m.

For the next investigation the length of the pressure area is 0.4 m which corresponds to the frame length of one frame spacing. The same unit load of 100 kN is chosen, which results in a pressure of

$$\frac{100 \text{ kN}}{0.4 \text{ m} \times 0.3 \text{ m}} = 833.33 \text{ kPa}. \tag{70}$$

In Figure 42 the absolute error is shown.

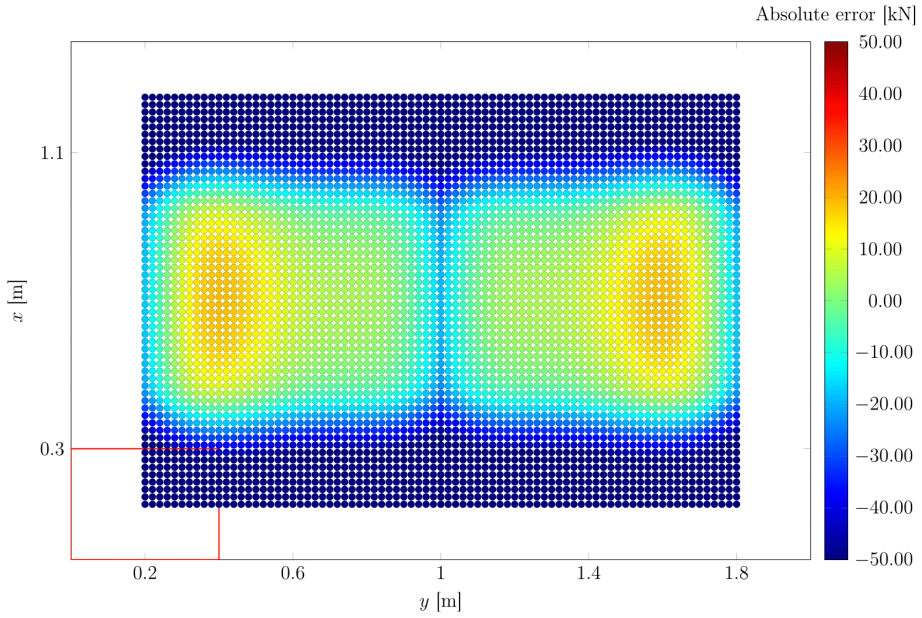

Figure 42: Absolute error, pressure area 0.3 m × 0.4 m.

The pressure area of the ice is displayed in the lower left corner of the Figure. Since the pressure area is bigger, fewer cases are calculated. As expected, within the instrumented area an acceptable accuracy can be seen whereby outside the instrumented area the load is underestimated. In addition the area between the second and the forth frame tends to be nearly uniform in terms of accuracy. In the previous case between the first and the second and between the fourth and the fifth frame the absolute error was generally larger. In this case the boarders are smoother and the error is smaller in the area between the first and the second and between the fourth and the fifth frame as in the previous case. The instrumented area gives in the mean absolute errors for the load of

$$\mu_{icm,833kPa} = -7.991 \text{ kN} \tag{71}$$

and the standard deviation of the absolute errors is

$$\sigma_{icm,833kPa} = 17.729 \text{ kN}. \tag{72}$$

In Figure 43 the relative error of the calculated load location is shown. At $L/2$ the determined location is exact. In comparison to Figure 40 the accuracy outside the mid line is slightly better in Figure 43.

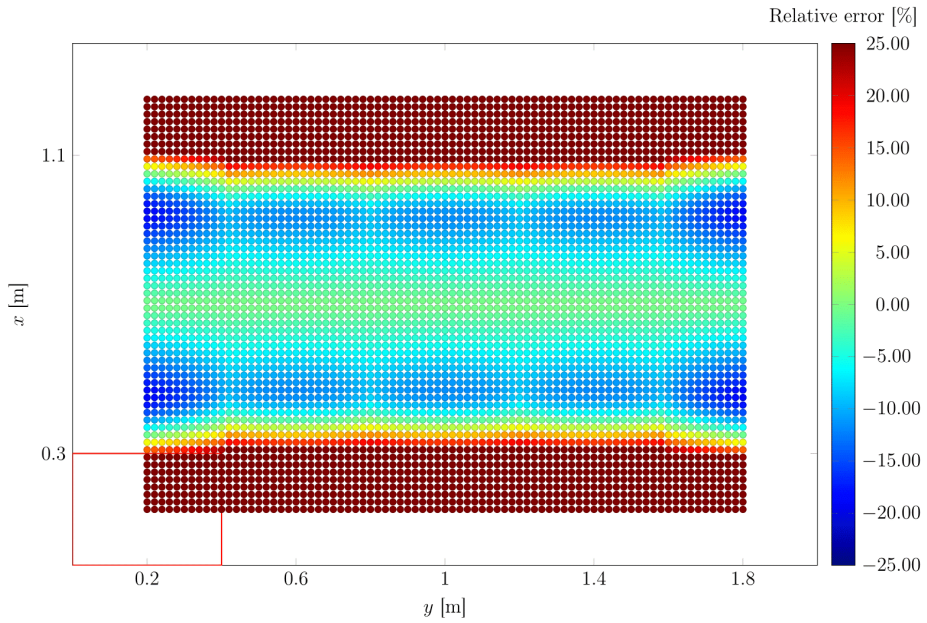

Figure 43: Relative error of the calculated load locations, pressure area 0.3 m × 0.4 m.

The instrumented area gives in the mean relative errors for the load location of

$$\mu_{icm,833kPa,loc} = -3.00249\ \% \tag{73}$$

and the standard deviation of the relative errors is

$$\sigma_{icm,833kPa,loc} = 9.355\ \%. \tag{74}$$

In Figure 44 the standard deviation of the load vector $\boldsymbol{F}$ is shown. The same homogeneous area in form of an ellipse can be seen along the frames. In addition it seems to be, that the maximum standard deviation occurs at the middle frame and it is nearly constant.

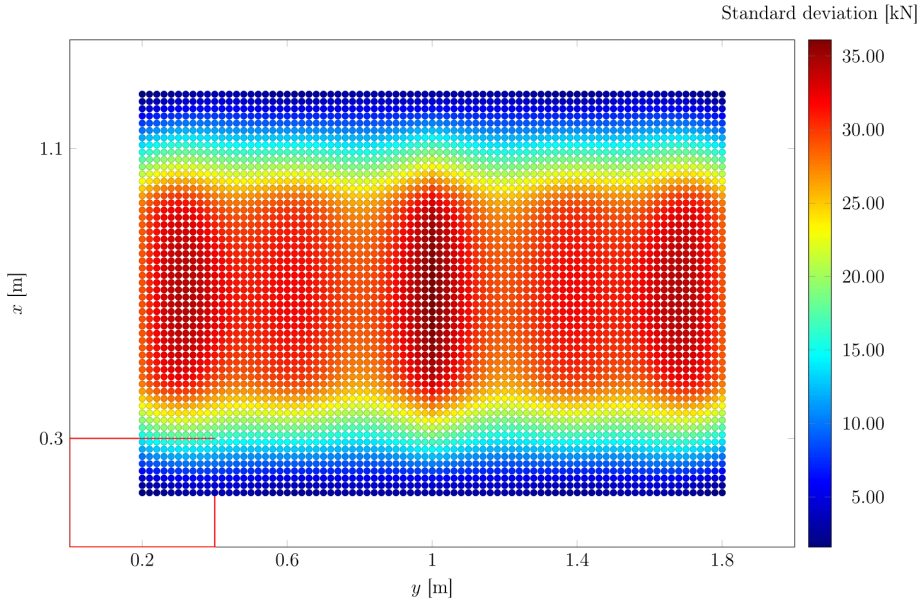

Figure 44: Standard deviation of the load vector $\boldsymbol{F}$, pressure area 0.3 m $\times$ 0.4 m.

For the next investigation the length of the pressure area is 0.8 m which corresponds to the frame length of two frame spacings. The same unit load of 100 kN is chosen, which results in a pressure of

$$\frac{100 \text{ kN}}{0.8 \text{ m} \times 0.3 \text{ m}} = 416.67 \text{ kPa}. \tag{75}$$

In Figure 45 the absolute error is shown.

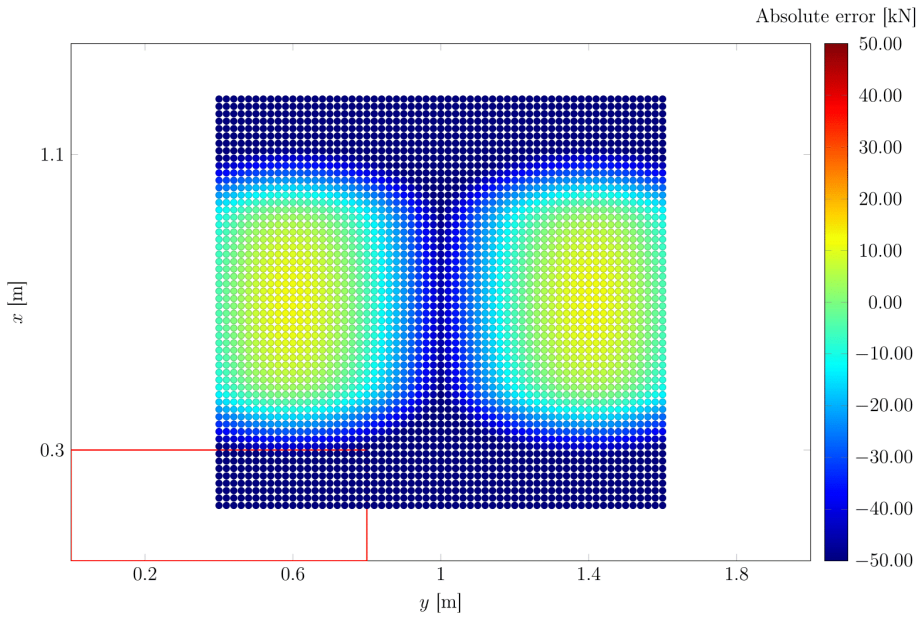

Figure 45: Absolute error, pressure area 0.3 m × 0.8 m.

The pressure area of the ice is displayed in the lower left corner of the Figure. In contrast to the cases shown in Figure 39 and Figure 42 only acceptable accuracy areas could be achieved on the second and on the forth frame. These homogeneous areas are in a form of an ellipse with a width of one frame spacing. Unusual is that the loads at the third frame are generally underestimated just like outside the instrumented area. The instrumented area gives in the mean absolute errors for the load of

$$\mu_{icm,416kPa} = -16.534 \text{ kN} \tag{76}$$

and the standard deviation of the absolute errors is

$$\sigma_{icm,416kPa} = 20.256 \text{ kN}. \tag{77}$$

In Figure 46 the relative error of the calculated load location is shown.

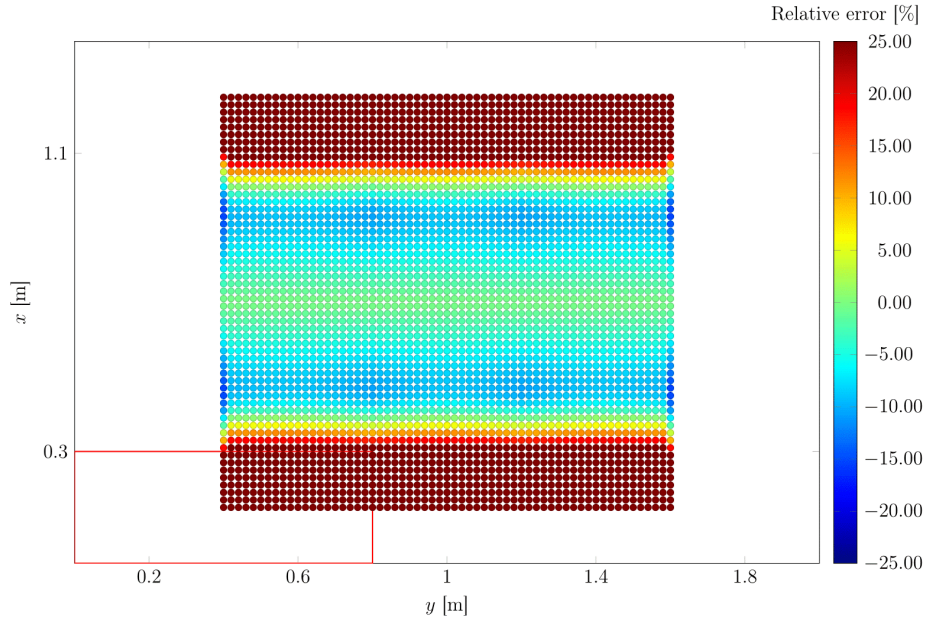

Figure 46: Relative error of the calculated load locations, pressure area 0.3 m × 0.8 m.

It seems to be, in contrast to the determination of the loads, that the accuracy of the load location increases with the load length. In Table 9 a summary of the calculated errors for the conducted investigations of the double instrumented cases is presented.

Table 9: Summary of the calculated errors for the conducted investigations.

Type of load	μ, Load [kN]	σ, Load [kN]	μ, Location [%]	σ, Location [%]
1 kN, point load	-0.00795	0.190	-9.425	11.886
100 kN, point load	-0.921	18.926	not calc.	not calc.
100 kN, $\ell = 0.2$ m	-4.0507	18.275	-3.201	9.479
100 kN, $\ell = 0.4$ m	-7.991	17.729	-3.00249	9.355
100 kN, $\ell = 0.8$ m	-16.543	20.256	-1.183	9.509

Table 9 shows that with increasing load length the accuracy for determining the load magnitude decreases, by means both the mean value of the errors and the standard deviation of the errors increase with the load length. For the determination of the load length the inverted seems to be the case. With increasing load length the accuracy for the determination of the load length increases at a stable standard deviation. Again at $L/2$ the determined load location is exact. In comparison to Figure 40 and Figure 43 the accuracy outside the mid line is better in Figure 46. Furthermore the accuracy range, green to light blue, is wider around the mid line. The instrumented area gives in the mean relative errors for the load location of

$$\mu_{icm,416kPa,loc} = -1.183\ \% \tag{78}$$

and the standard deviation of the relative errors is

$$\sigma_{icm,416kPa,loc} = 9.509\ \%. \tag{79}$$

In Figure 47 the standard deviation of the load vector $\boldsymbol{F}$ is shown. The same homogeneous area in form of an ellipse can be seen along the frames - more specific around the third frame. Here again the maximum standard deviation occurs at the middle frame and it is nearly constant.

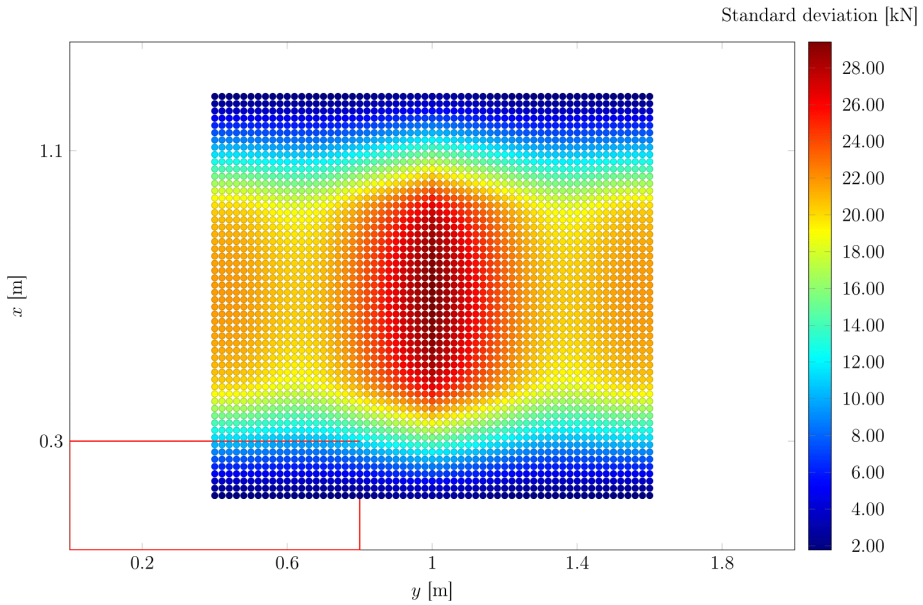

Figure 47: Standard deviation of the load vector $\boldsymbol{F}$, pressure area 0.3 m $\times$ 0.8 m.

7. An approach to determine the load length

As the author of Literature [17] states the load length is one of the main uncertainty at measurements based on shear strain differences. Thus in this Section an approach to determine the load length is presented. The following description is based on the Literature [18]. Either the load acts only on one frame or on several frames at the same time depending on the load length. In both cases it is taken into account that most of the load is carried by the frames. On the basis of the superposition principle, a long loading can be considered to consist of sub-loads acting on individual frames as it can be seen in Figure 48.

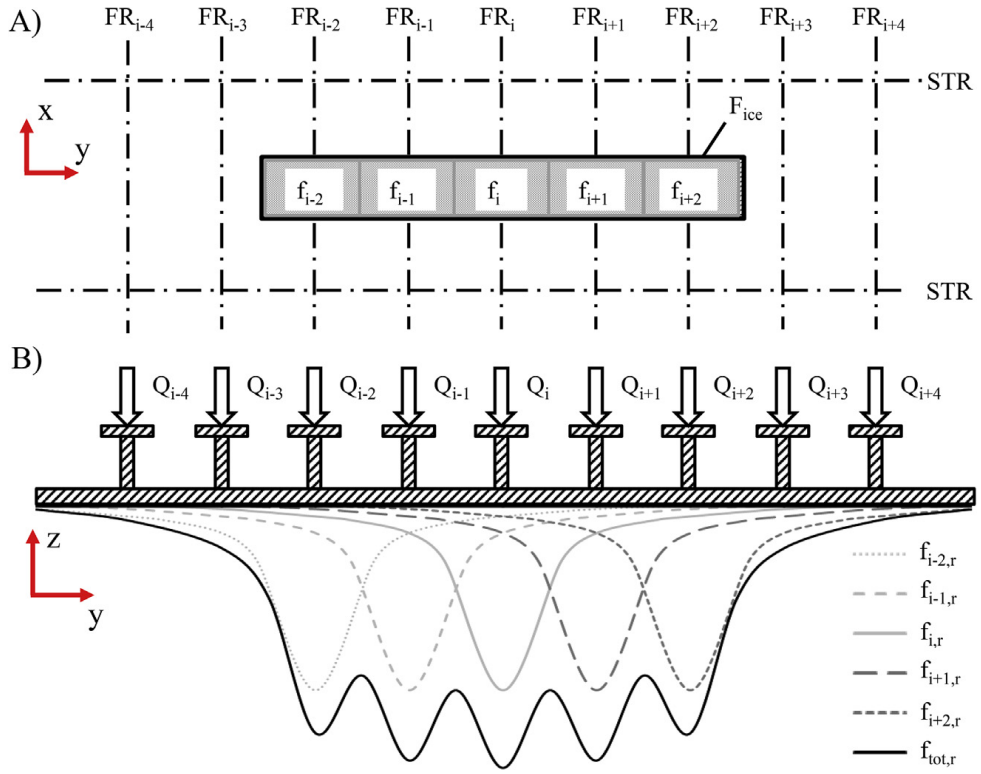

Figure 48: A) A schematic presentation of an ice load, F_{ice}, acting on the shell structure over several frames and its separation into subloads, f. B) A schematic two dimensional model of the load distribution and interaction between the frames. Figure taken from [18].

FR and STR denote a frame and stringer, respectively, Q represents the supporting reaction force of the frame. The subindex $i + n$, n = {-4, -3, ..., 3, 4}, refers to a frame and r to distributed loading between frames. The black solid line, $f_{tot,r}$ refers to the total internal force which is obtained summing all the internal loads, $f_{i,r}$, caused by the external subloads, f_i. In the example Figure 48, if the length of the external loading is taken as the responding length, then the load length is nine frame spacings. However, in reality it is only about five frame spacings. Thus, the internal redistribution of the loading should be taken into account in order to define the actual load length [18].

Since according to [18] the loading can be considered to consist of sub-loads, the calculated load vector $\boldsymbol{F}$ using the ICM, gives the magnitudes of these sub-loads. Thus when five frames are instrumented, the magnitudes of these sub-loads are calculated. In addition, the distribution of the entries of the load vector $\boldsymbol{F}$ gives an indication of the internal distribution of the load. An exemplary plot of two different load vectors $\boldsymbol{F}$ is shown in Figure 49.

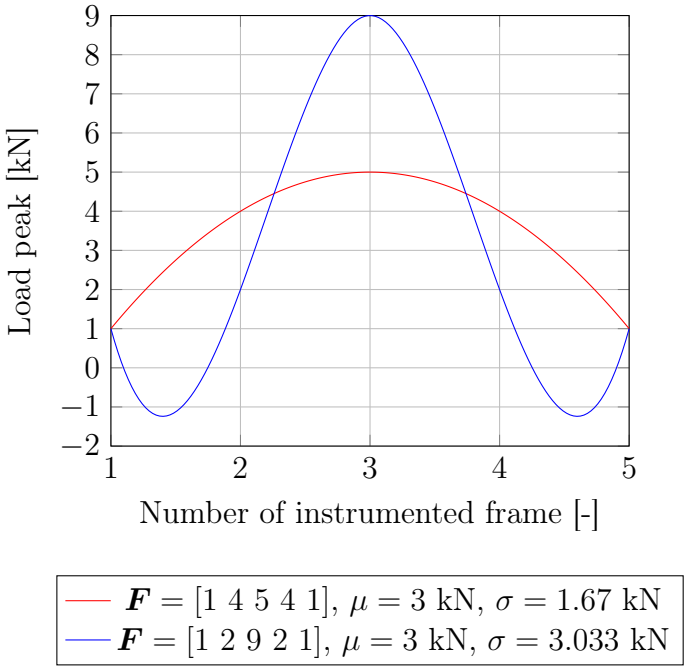

Figure 49: Exemplary plot of two different load vectors $\boldsymbol{F}$ calculated by the ICM.

The red line represents a long load which is about three frame spaces long and the blue line represents a shorter load which is about one frame space long. In this case, there are two equal loads if the entries of the load vector are summed. However, as can be seen, the load with the shorter load length has a greater standard deviation than the load with the longer load length. Thus the author states that the standard deviation of the load vector $\boldsymbol{F}$ behaves anti proportional to the load length assuming a normal-like distribution of the entries of the load vector $\boldsymbol{F}$. In the following it is investigated if a relationship between the standard deviation of the load vector $\boldsymbol{F}$ and the load length can be made.

In Figure 50 the standard deviation of the load vector $\boldsymbol{F}$ is plotted over the load length. The procedure was as follows. In the middle of the plate field at $x = 0.7$ m and $y = 1.0$ m a pressure was applied with a constant height. From 0.04 m the load length was increased by a increment of 0.02 m. In order to have the same unit load the following pressure was applied.

$$p = \frac{100 \text{ kN}}{hl} \tag{80}$$

Where h is the constant load height and l the load length. Two calculations were conducted with a load height of $h = 0.2$ m and $h = 0.4$ m.

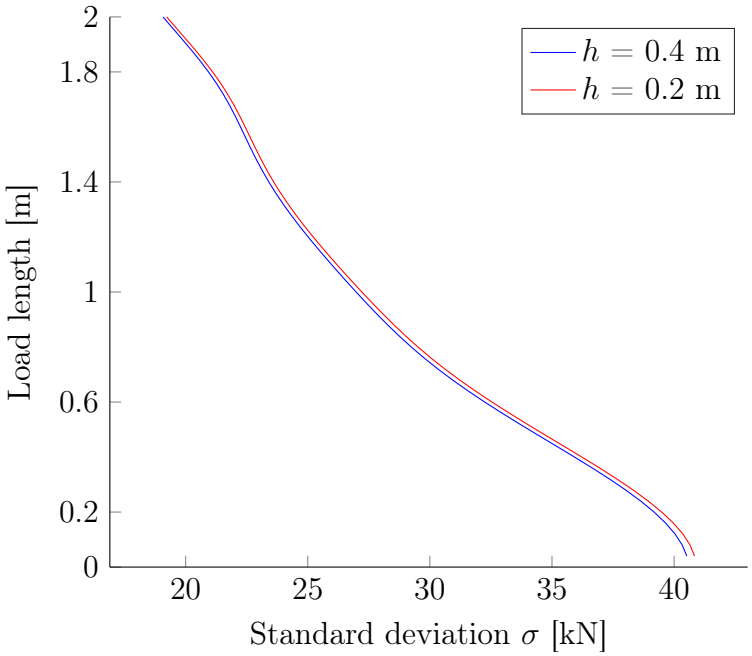

Figure 50: Standard deviation over the load length.

As it can be seen there are marginal differences between the calculation with a load height of $h = 0.2$ m and a load height of $h = 0.4$ m. In order to give an estimate of the load length, trend lines can be created for the graphs. For a proper estimation of these trend lines, a log-log plot of Figure 50 is shown in Figure 51.

A log-log plot is a two-dimensional graph of numerical data that uses logarithmic scales on both axes. Relationships of the form $y = ax^k$, appear as straight lines in a log-log plot. The power term corresponds to the slope and the constant term corresponds to the shift in vertical direction. Thus these graphs are very useful for recognizing these relationships and estimating parameters [2].

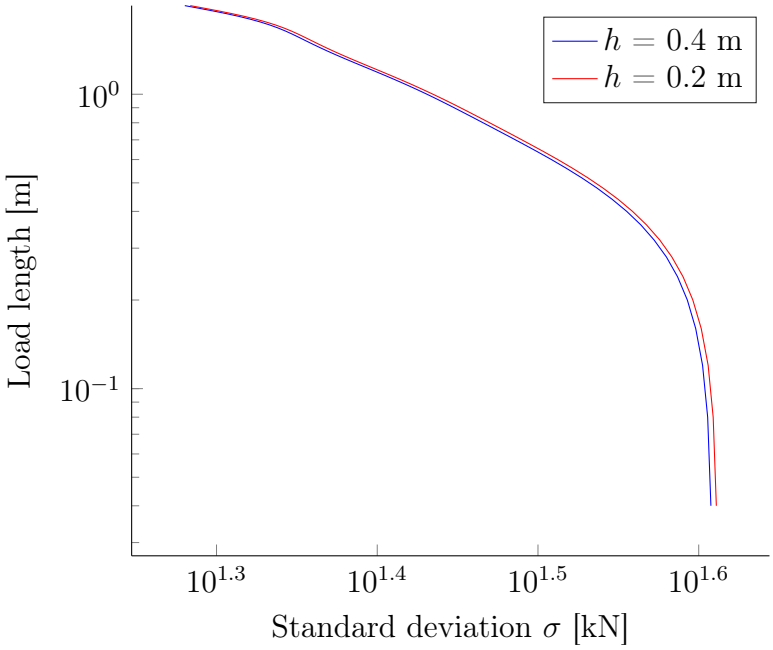

Figure 51: Standard deviation over the load length, log-log plot.

In Figure 51 a logarithmic-like relationship can be recognized, which supports the statement of the author, that the relationship between the standard deviation of the load vector $\boldsymbol{F}$ and the load length are anti proportional. Thus trend lines based on a logarithmic approximation are created. In Figure 52 these trend lines are depicted and the corresponding log-log plot is depicted in Figure 52.

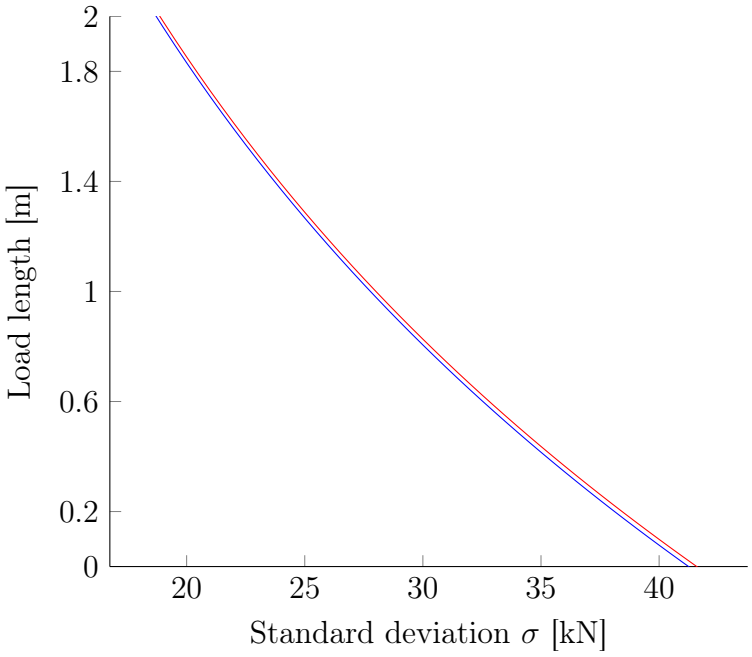

Figure 52: Standard deviation over the load length approximation.

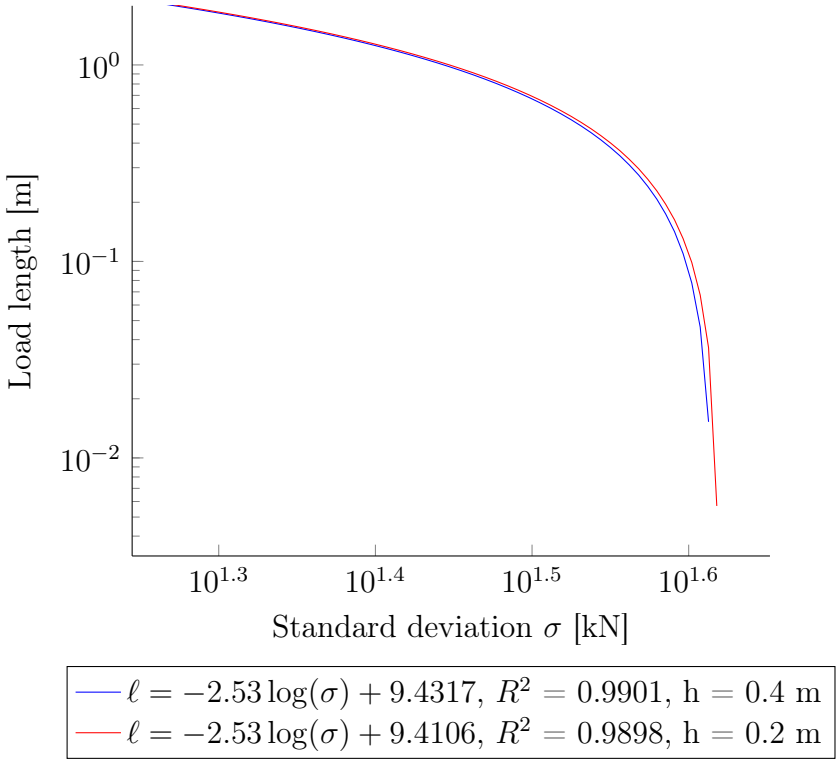

Figure 53: Standard deviation over the load length approximation, log-log plot.

As it can be seen the coefficient of determination which is denoted as R^2 is for both graphs about 0.99. In statistics this coefficient is the proportion of the variance in the dependent variable that is predictable from the independent variable [2]. In regression, the R^2 coefficient of determination is a statistical measure of how exact the regression predictions approximate the real data points. An R^2 of 1 indicates that the regression predictions perfectly fit the data [5]. Among the assumptions made, there is a logarithmic relationship between the standard deviation of the load vector $\sigma(\boldsymbol{F})$ and the load length ℓ. Thus a first approach for the determination of the load length was presented. To what extent this approach can be applied should be studied in future investigations.
Now having the load vector $\boldsymbol{F}$ and thus the calculated position, the load length could be estimated using this approximation. This method applies when the load length is determined in the middle of the third frame under the used conditions.

8. Possible sources of errors of ice load measurements

In this Section the possible sources of errors within the measurement set-up will be described in order to evaluate the future outcomes out of the ice load measurements properly. Coming to some first limitations based on the Literature [12]. Since shear-strains are derived from normal strain measurements, accurate results require the same care and attention to detail as for any other strain measurement task. At first, Equation 11 and Equation 12 are based on the theory of small-strains. So that the Equations of 17 are only precise for infinitesimal strains but they are adequately accurate for typical strain measurements on metal test objects where the strains are usually less than 1 % [12]. Furthermore the uniformity of the strain field under the area covered by the rosette should be considered. Ideally would be an uniform state of strain. Since the determination of shear-strain is accomplished by measuring two normal strains it is always necessary to make certain that the indicated shear-strain is unaffected by non-shearing load components such as bending, twisting, or axial loads. This requirement can usually be satisfied quite easily in the case of geometrically symmetric test objects, which is not the case when looking on the topology of a ship's structure. Besides, through the stochastically pressure distribution from the ice on the ship's hull a good load alignment is not present neither. Thus in case of ice load measurements it is recommended by the author that each frame should be at least double instrumented, in order to get more accurate results.
The assumption is that near the boundary conditions the stresses will be much higher compared to reality, since the large bending moments are inherent for a rigid clamp boundary condition. At the same time it is expected that the displacement will be much greater in areas far away from the boundary conditions. More precisely, the largest displacement is expected at the center of the applied force. Through the chosen case it is possible that plastic deformation occurs because of the high stresses at the boundary conditions, though in reality plastic deformation should not occur at this magnitude of load. To get a better understanding of the influence of the boundary effects on the global solution, various boundary conditions can be applied. For a more precise analysis, the stiffness of the surrounding structure should be applied by mechanical springs at the places of the boundary conditions instead of applying the boundary conditions in the form of displacement restrictions. The assumed boundary conditions are sufficient to evaluate the structural behavior.
In addition, it is important to know, when the location of the loading is not between the sensors in vertical direction. The measurement fails outside the instrumented area as the method does not account for the loading having an effect outside the measurement area. As the author pointed out in the Section 4 and the following sections, loads outside the instrumented area are generally underestimated. In Section 5 the author shows how the load location can be determined with the existing measuring system.
The measurements only account for the location of the instrumentation, since the loads are measured of a local structure and no information about the surrounded not instrumented structure can be obtained. It could be shown under the used assumptions that in the middle of the frames the calculated load location resulted in $L/2$, which is to 100 % exact. Thus future measurements with the help of the calculated load position could be

regarded as permissible, since it is ensured that the load is applied in the instrumented area. It should be ensured that the maximum value in the load vector $\boldsymbol{F}$ is present in one of the inner frames.
Another problem is, that the structure in the ice belt region is rather stiff. Thus, the response to smaller loads is minimal and difficult to measure, as the strain gauges are commonly optimized for higher loads [17]. As a consequence, it can be impossible to separate the smaller loads from the noise of the carrier voltage of the measurement system. In addition, the pressure distribution within the contact area in the horizontal direction and the load length are the main uncertainties affecting the measurement based on shear-strain differences [17]. In Section 7 the author showed an approach how the load length could be determined by calculating the standard deviation of the load vector $\boldsymbol{F}$. One possible error is that although the vertical position ℓ can be determined, the horizontal position is only estimated on the basis of the load vector $\boldsymbol{F}$. The maximum value of the load vector $\boldsymbol{F}$ indicates the frame at which the load is concentrated.
In addition, the maintenance of such a shear-strain measurement set-up for ice load measurements on a ship's hull requires higher personnel needs. Ideally, the installation of this measurement set-up should be easy as possible, yet the working environment in ships is challenging for strain gauge measurements. The main problems of the measurement set-up are the location of the power supply and the attachment of the cables, which can be long, depending on the environment. In addition physical problems occur like humidity, cold temperatures, high velocities, accelerations and vibration. These problems affect not only the measuring system but also the personnel. Furthermore is the possibility of confined space, low sources of light, air ventilation and limited possibilities for the transportation of the measurement devices [3].

9. Conclusion

In the introduction of this thesis with the title *the measurement accuracy of instrumented ship structures under local loads using strain gauges* following questions arose. How accurate is the mapping of the ICM? Which structures are suitable for measurements of shear-strain differences? How can the existing method be improved and what measurement uncertainties are inherent in the overall system?
A suitable measurement method for ice load measurements is by measuring the shear force using strain gauges in a half-bridge for the shear-strain measurements. The strain gauges are attached at the end of each instrumented frame near the next higher supporting structure, see Figure 25. In order to consider the relation of the measured shear-strains and the ice load, an influence coefficient matrix is calculated. A simple grillage model with one plate and five frames, Figure 24, was modeled for the conducted investigations.
The ICM maps the response of the structure and in Section 4 and further sections it is shown how the ICM conducts the mapping. It could be shown that the mean relative error within the instrumented area by one sided instrumented frames is $\mu = 19.411$ % regarding point loads with a standard deviation of $\sigma = 13.646$ %. Double instrumented frames show a mean relative error within the instrumented area of $\mu = 14.083$ % with a standard deviation of $\sigma = 12.726$ %, regarding point loads. Thus it is shown that the measurement accuracy is largely enhanced with a double instrumentation. This means that the frame is instrumented on both sides. Thus shear-strain from non shearing forces are neglected. This roughly answers the question of which structures are most suitable for measurements of shear-differences. Symmetrical structures with a good load alignment are suitable for measurements of shear-differences. This applies as well as regarding ice load measurements on a ship's hull when using strain gauges.
It is shown that outside the instrumented area, in vertical and horizontal direction, loads are generally underestimated. The load location was in past ice load measurements one of the uncertainties [17]. The author shows in Section 5 how the load location in vertical direction can be determined using the already existing measurement system. With the method presented, loads in the middle of the frame could be exactly determined under the used assumptions. In Table 10 a summary of the calculated errors for the conducted investigations is shown. Worth to be mentioned is that only the double instrumented cases are shown in this table. Besides the load height was kept constant through the investigation of the line loads and was chosen to be $h = 0.3$ m. The values are displayed with 3 significant digits.

Table 10: Summary of the calculated errors for the conducted investigations.

Type of load	μ, Load [kN]	σ, Load [kN]	μ, Location [%]	σ, Location [%]
1 kN, point load	-0.00795	0.190	-9.425	11.886
100 kN, point load	-0.921	18.926	not calc.	not calc.
100 kN, $\ell = 0.2$ m	-4.0507	18.275	-3.201	9.479
100 kN, $\ell = 0.4$ m	-7.991	17.729	-3.00249	9.355
100 kN, $\ell = 0.8$ m	-16.543	20.256	-1.183	9.509

Table 10 shows that with increasing load length the accuracy for determining the load magnitude decreases. For the determination of the load length the inverted seems to be the case. With increasing load length the accuracy for the determination of the load length increases.
Besides in Section 7 the author shows an approach how the load length can be estimated using the standard deviation of the load vector $\boldsymbol{F}$. The chosen approach shows a logarithmic-like relationship between the standard deviation of the load vector and the load length. A normal distribution of the load vector entries is assumed. For future investigations regarding the determination of the load length other distribution functions should be considered. Since only a first approach for the determination of the load length is presented, in the future it should be investigated to what extent this approach can be applied.
The pressure distribution within the contact area in the horizontal direction and the load length are the main uncertainties in past ice load measurements [17].
From the results of this thesis, the existing measuring system consisting of double-instrumented frames could provide information about the load position in vertical direction and load length in addition to the load size through a post-connected micro controller.
A simple grillage model consisting of five frames and one plate was investigated. For further investigations the author recommends to change the complexity of the models. This includes unsymmetrical frames, curved frame with or without unsymmetrical stiffeners. A future study could consist of different tests of the methods used in this thesis with the model presented in the project thesis [3]. Uneven load application should be investigated as well. Thereby different materials within the grillage model should not be neglected. The results of these investigations could be correlated with the results of the methods already used to determine the load magnitude and the methods introduced by the author to determine the load position and load length. The *APDL*-Code of the calculations conducted in *Ansys 18.2* are shown in the Appendix A, Figure 78 - Figure 88.

References

[1] T. Abbey. Global-to-local modeling in fea. `https://www.digitalengineering247.com/article/global-local-modeling-fea/`. Date accessed: 18.03.2019.

[2] M. Abramowitz and I. A. Stegun, editors. *Handbook of mathematical functions: With formulas, graphs, and mathematical tables*. Dover books on mathematics. Dover Publ, New York, NY, 9. dover print edition, 2013.

[3] A. M. Böhm. *Analysis of a FEM-model for measurements of ice loads on a ship's hull with strain gauges*. Institute for Ship Structural Design and Analysis, Hamburg University of Technology, 2018.

[4] DIN 1319. *Grundlagen der Meßtechnik: Fundamentals of metrology*, volume 2 of *Deutsche Norm*. Beuth, Berlin, 1980.

[5] D. N. Gujarati and D. C. Porter. *Basic econometrics*. The McGraw-Hill series Economics. McGraw-Hill Irwin, Boston, Mass., 5. ed. edition, 2009.

[6] S. Keil. *Dehnungsmessstreifen*. Springer Fachmedien Wiesbaden, Wiesbaden, 2nd ed. edition, 2017.

[7] L. Kujala et al. *Talvimerenkulku ja sen kustannukset Perämerellä, Winter navigation in the Gulf of Bothnia*. Aalto University, 2011.

[8] L. Müller and H. G. Payer. *Port and Ocean engineering under Arctic Conditions 1987: Loads on research vessel polarstern under arctic conditions*. POAC 1987, 1988.

[9] T.-K. Lee, J.-H. Lee, H. Kim, and C. W. Rim. Field measurement of local ice pressures on the araon in the beaufort sea. *International Journal of Naval Architecture and Ocean Engineering*, 6(4):788–799, 2014.

[10] M. Suominen, J. Romanoff H. Remes & P. Kujala. The determination of ice-induced loads on the ship hull from shear strain measurements. In C. G. Soares and R. A. Shenoi, editors, *Analysis and design of marine structures V*, pages 375–383. CRC Press/Balkema, Leiden, The Netherlands, 2015.

[11] G. Müller and C. Groth. *FEM für Praktiker*, volume 23 of *Edition expertsoft*. expert-Verl., Renningen, 7. aufl. edition, 2002.

[12] C. C. Perry. Plane-shear measurement with strain gages. *Experimental Mechanics*, 9(1):19N–22N, 1969.

[13] D. W. A. Rees. *Basic engineering plasticity: An introduction with engineering and manufacturing applications*. Elsevier, Boston, MA, 1st ed. edition, 2006.

[14] K. Riska, H. Rantala, and A. Joensuu. *Full scale observations of ship-ice contact: Results from tests series onboard IB Sampo, winter 1989*. Teknillinen korkeakoulu, Otaniemi, 1990.

[15] C. A. Sciammarella and F. M. Sciammarella. *Experimental mechanics of solids*. John Wiley & Sons, Hoboken, NJ, 2012.

[16] D. W. Stroock. *Probability theory: An analytic view*. Cambridge Univ. Press, Cambridge, rev. ed. edition, 1999.

[17] M. Suominen. *Uncertainty and variation in measured ice-induced loads on a ship hull*. Department of Mechanical Engineering, Aalto University, 2018.

[18] M. Suominen, P. Kujala, J. Romanoff, and H. Remes. Influence of load length on short-term ice load statistics in full-scale. *Marine Structures*, 52:153–172, 2017.

[19] Swedish Maritime Administration. *Finnish-Swedish ice class rules 2008*. Swedish Maritime Administration, Helsinki, 2008.

[20] Till Zorn. *Strain-gauge-based measurements of ice loads on ships.* Institute for Ship Structural Design and Analysis. Hamburg University of Technology, Hamburg University of Technology, 2018.

[21] S. P. Timošenko and S. Woinowsky-Krieger. *Theory of plates and shells*. Engineering societies monographs. McGraw-Hill, Auckland, 2. ed., internat. ed. edition, 1976.

[22] VDI/VDE/GESA-Richtlinie 2635. *Experimentelle Strukturanalyse Dehnungsmessstreifen mit metallischem Meßgitter: Kenngrößen und Prüfbedingungen*. Beuth-Vertrieb GmbH. VDI, Berlin and Köln, 2007.

A. Appendix

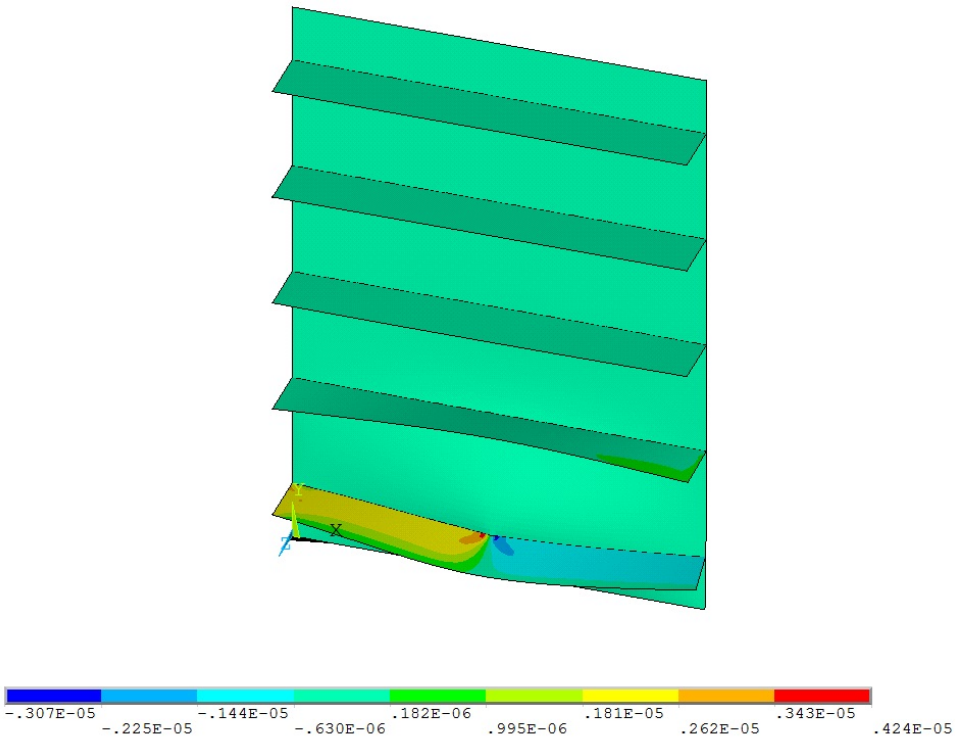

Figure 54: Cumulative distribution function of the relative error of an 1 kN pressure load from the instrumented area of Figure 29.

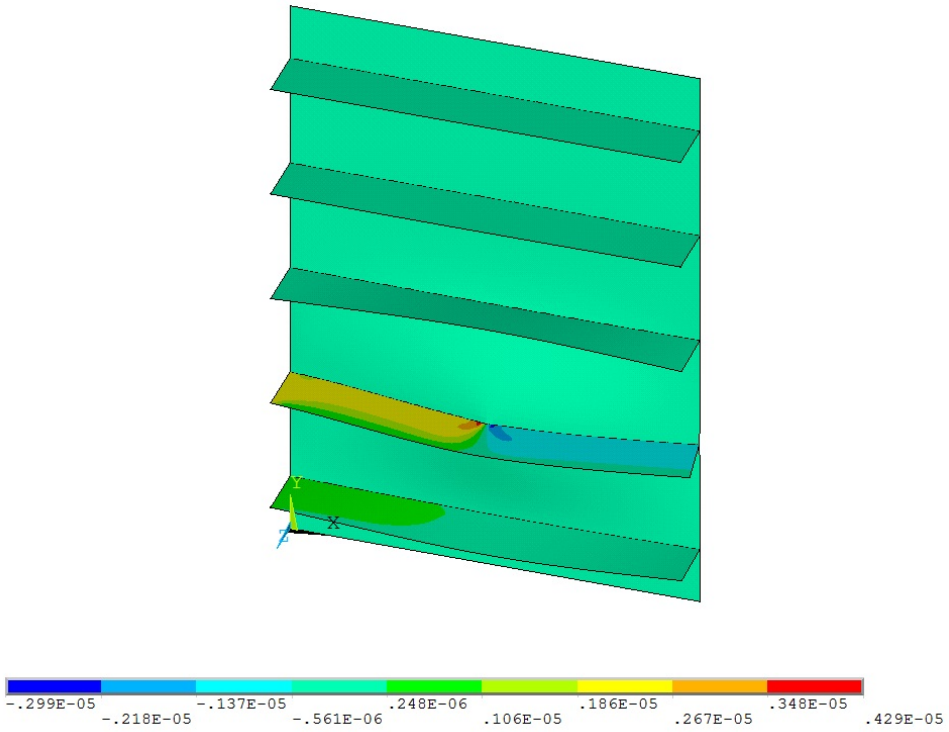

Figure 55: 2. load case for ICM calculation, inner structure, rotated 90° about z-axis.

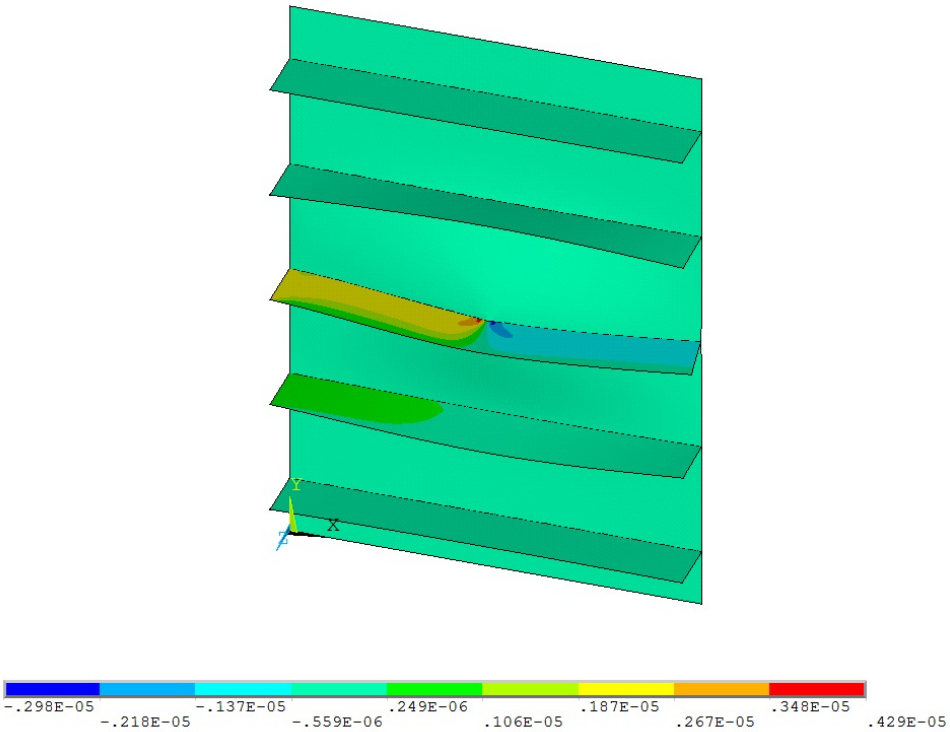

Figure 56: 3. load case for ICM calculation, inner structure, rotated 90° about z-axis.

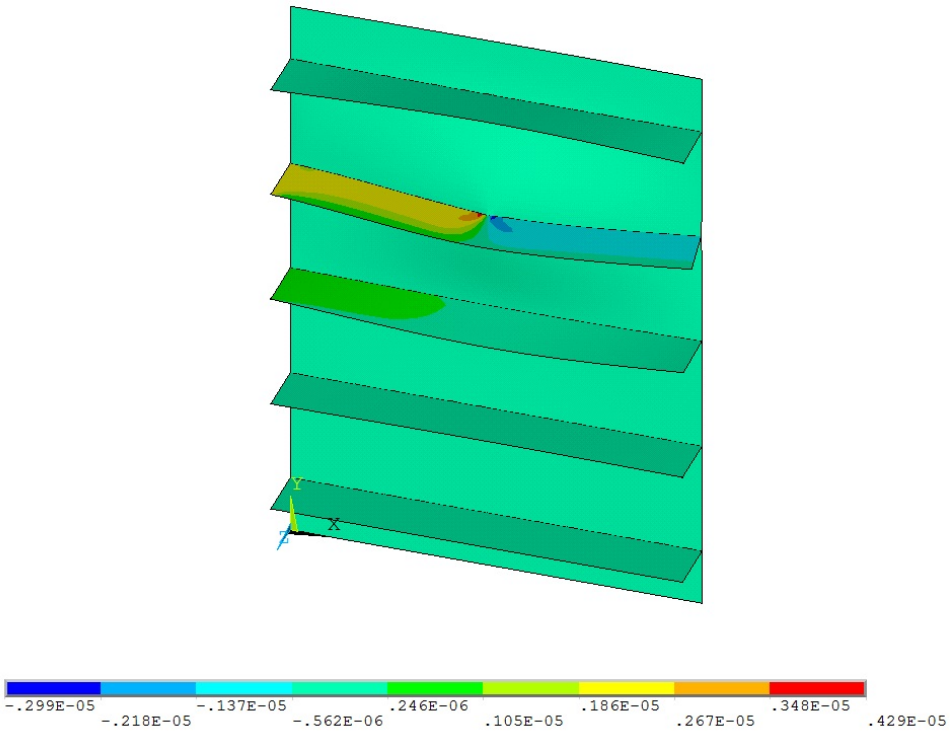

Figure 57: 4. load case for ICM calculation, inner structure, rotated 90° about z-axis.

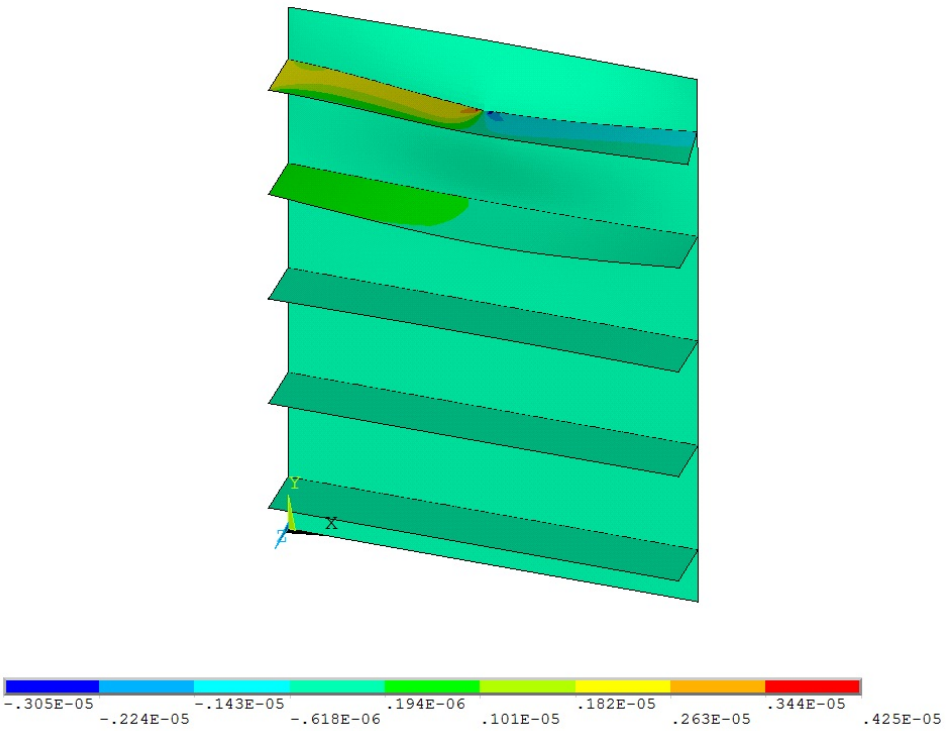

Figure 58: 5. load case for ICM calculation, inner structure, rotated 90° about z-axis.

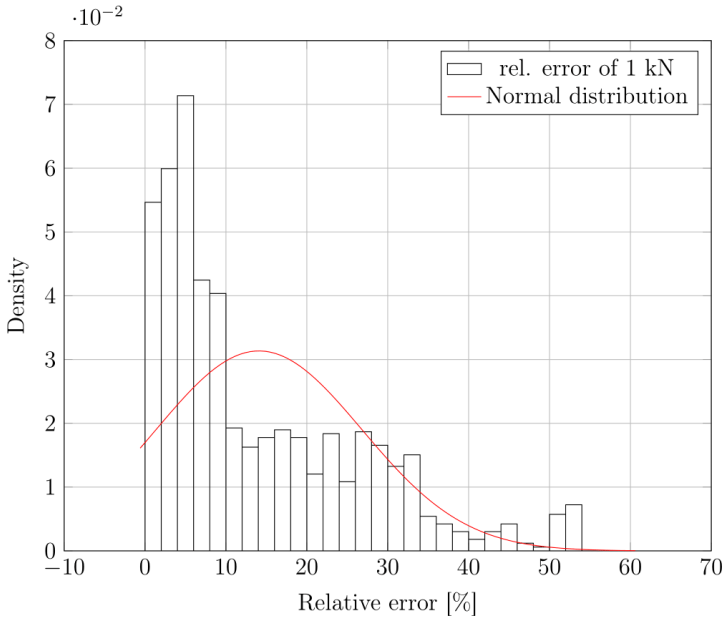

Figure 59: Probability distribution function of the relative error of an 1 kN point load from the instrumented area of Figure 32.

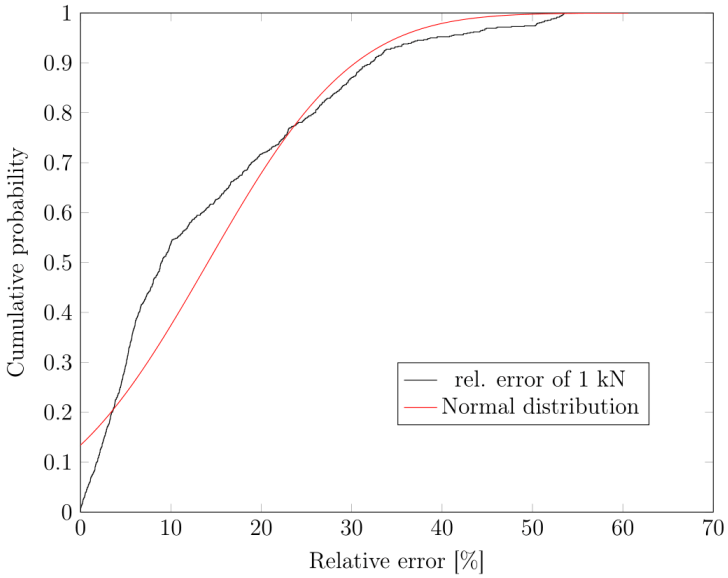

Figure 60: Cumulative distribution function of the relative error of an 1 kN point load from the instrumented area of Figure 32.

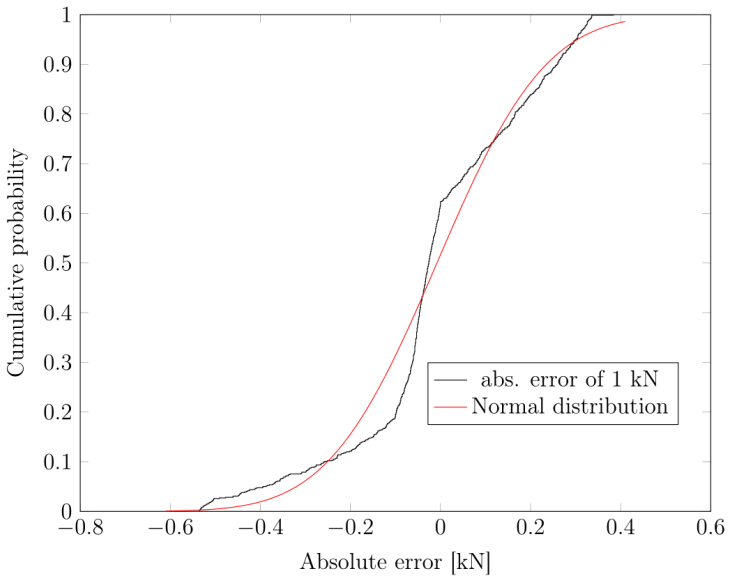

Figure 61: Cumulative distribution function of the absolute error of an 1 kN point load from the instrumented area of Figure 33.

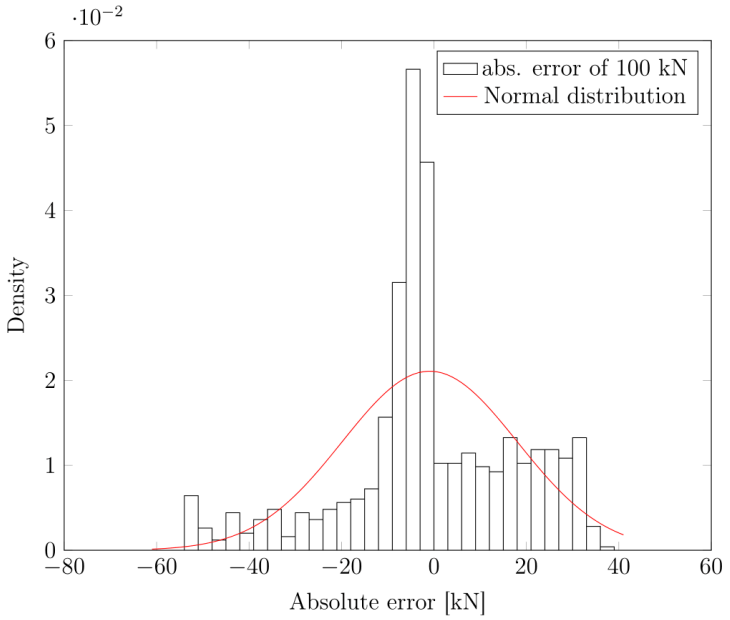

Figure 62: Probability density function of the absolute error of an 100 kN point load from the instrumented area of Figure 35.

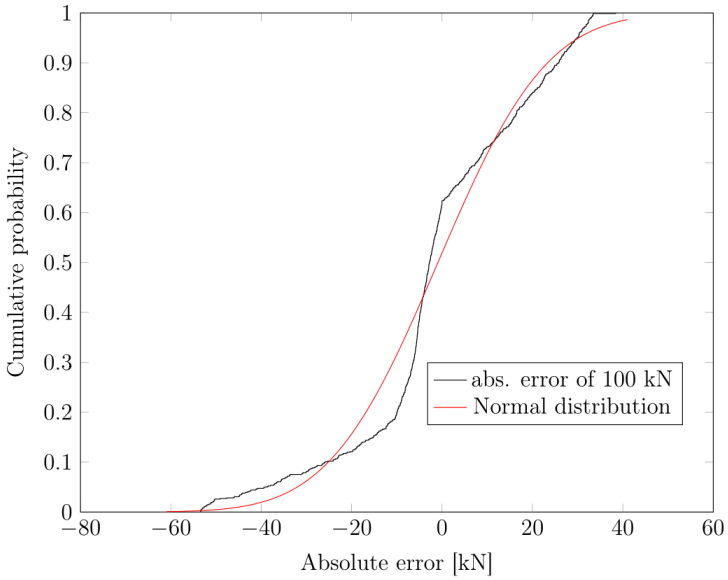

Figure 63: Cumulative distribution function of the absolute error of an 100 kN point load from the instrumented area of Figure 35.

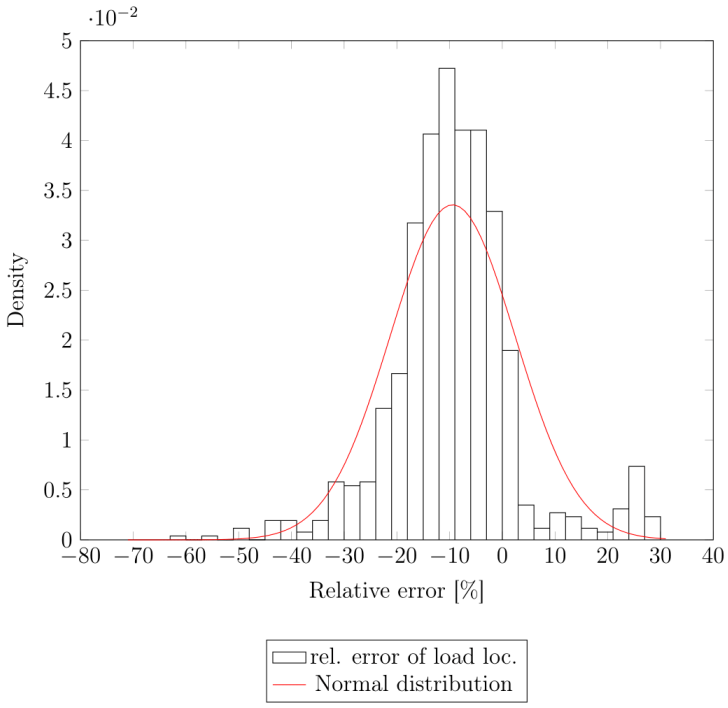

Figure 64: Probability density function of the relative error of the load location of an 1 kN point load from the instrumented area of Figure 37.

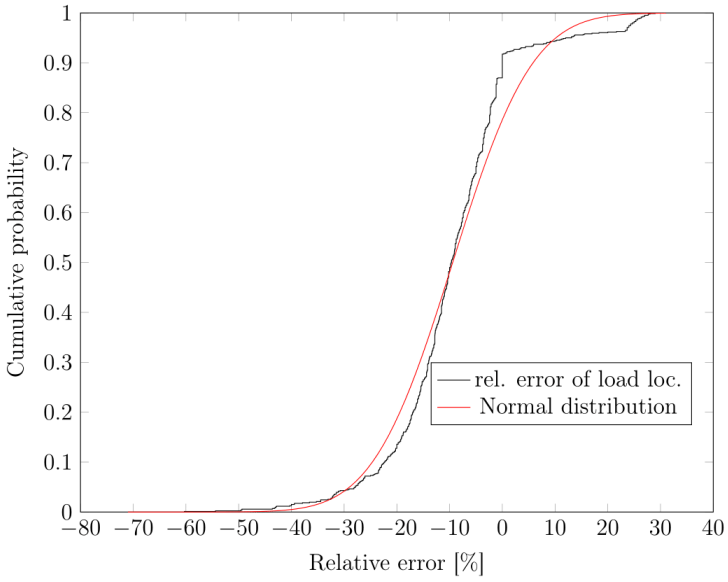

Figure 65: Cumulative distribution function of the relative error of the load location of an 1 kN point load instrumented area of Figure 37.

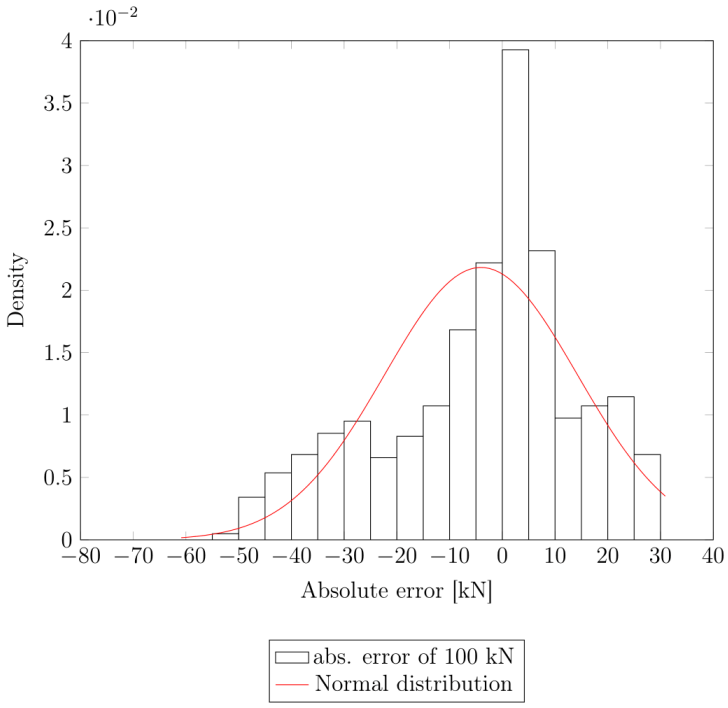

Figure 66: Probability density function of the absolute error, 100 kN, pressure area 0.3 m × 0.2 m, Figure 39.

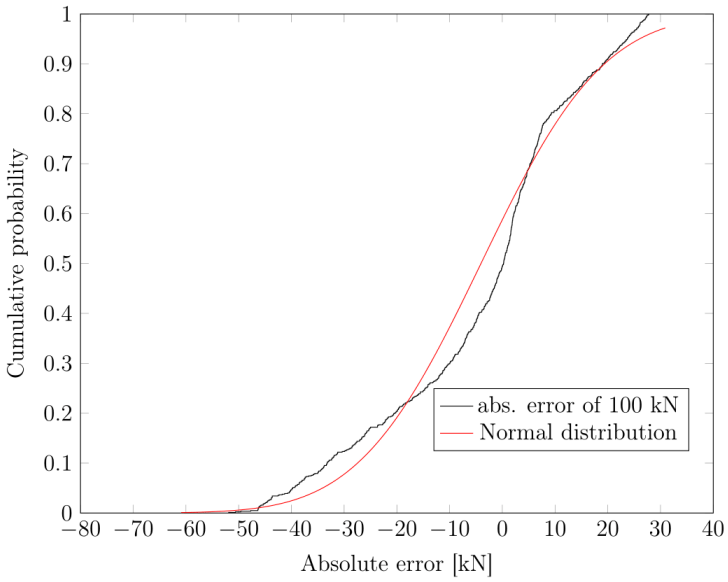

Figure 67: Cumulative density function of the absolute error, 100 kN, pressure area 0.3 m × 0.2 m, Figure 39.

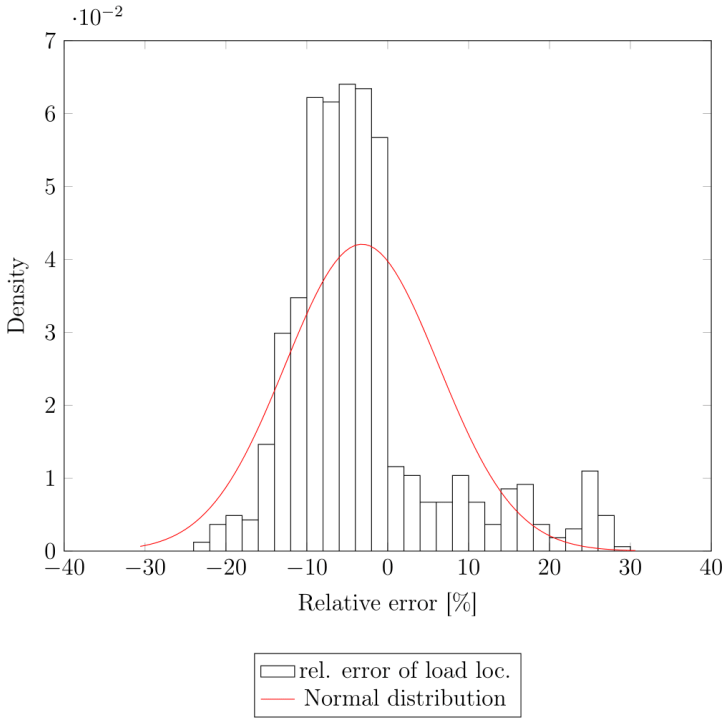

Figure 68: Probability density function of the absolute error, load location, 100 kN, pressure area 0.3 m × 0.2 m, Figure 40.

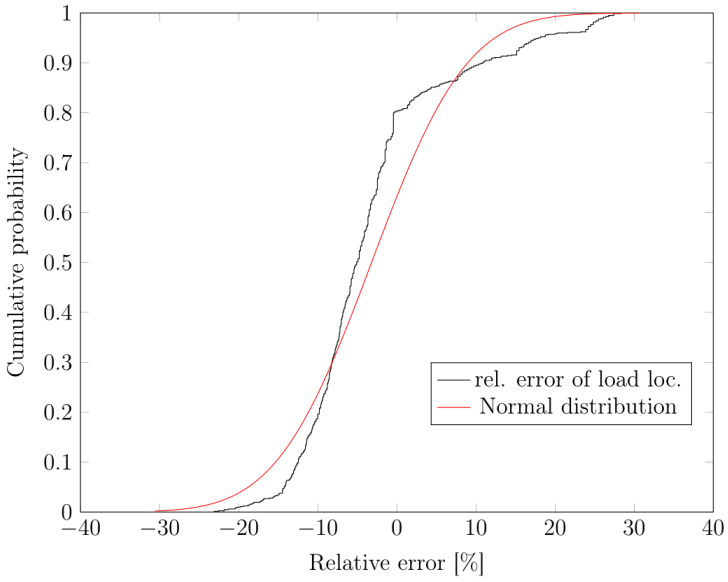

Figure 69: Cumulative density function of the absolute error, load location, 100 kN, pressure area 0.3 m × 0.2 m, Figure 40.

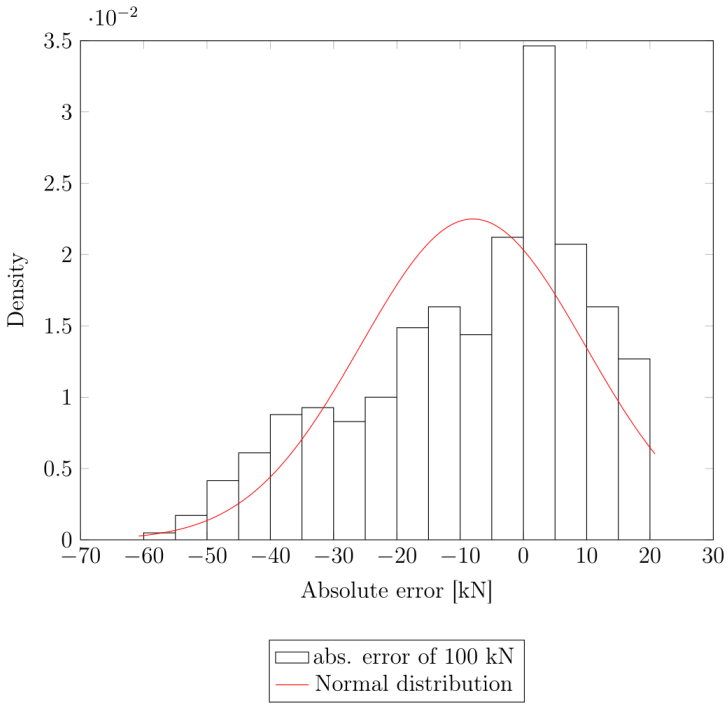

Figure 70: Probability density function of the absolute error, 100 kN, pressure area 0.3 m × 0.4 m, Figure 42.

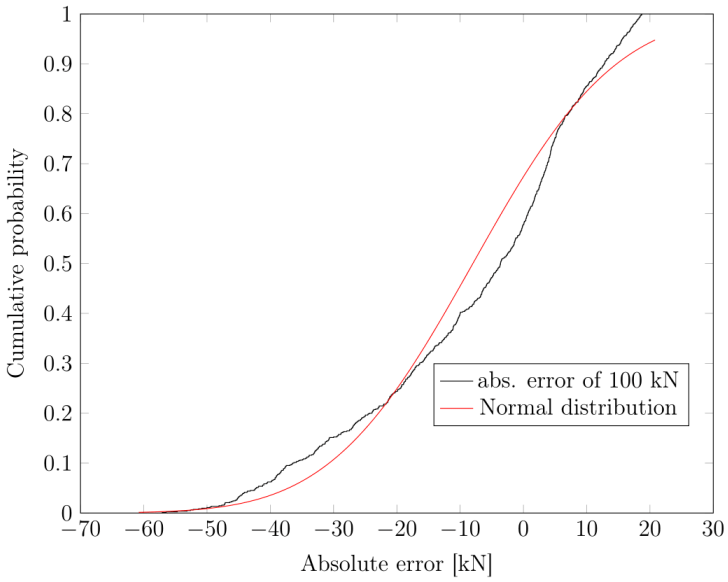

Figure 71: Cumulative density function of the absolute error, 100 kN, pressure area 0.3 m × 0.4 m, Figure 42.

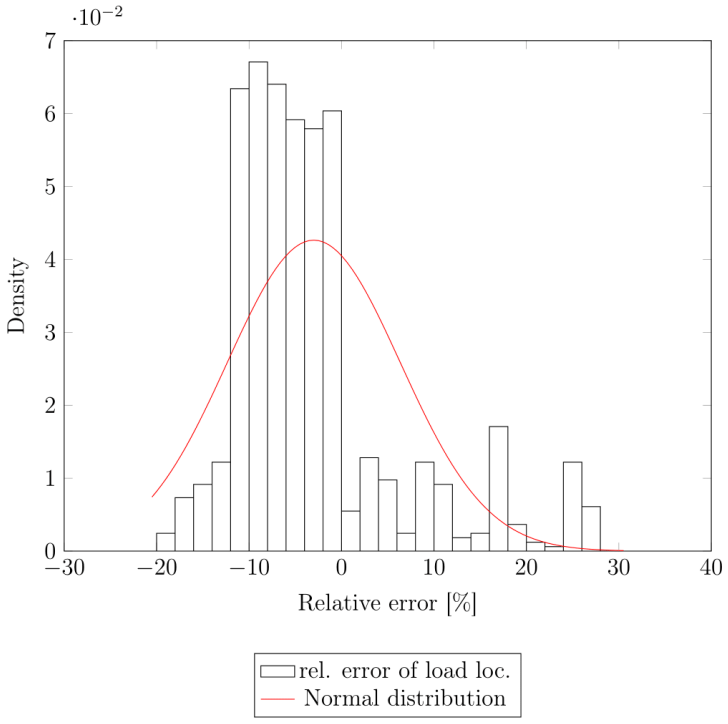

Figure 72: Probability density function of the absolute error, load location, 100 kN, pressure area 0.3 m × 0.4 m, Figure 43.

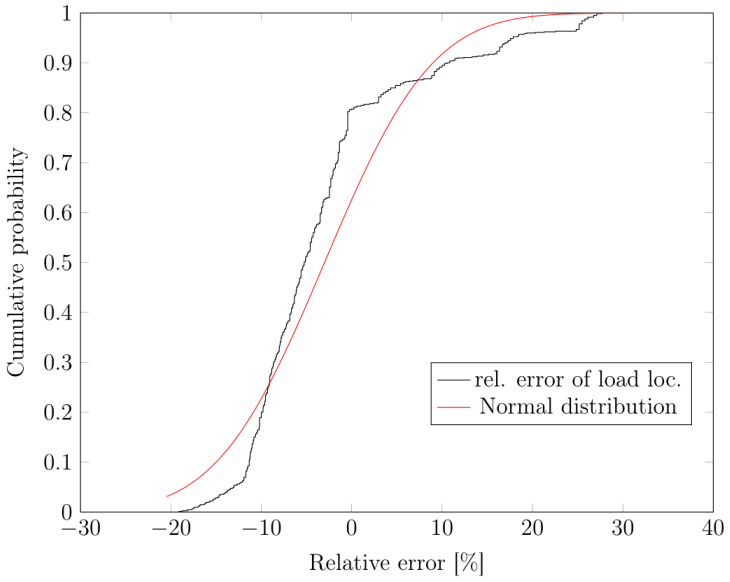

Figure 73: Cumulative density function of the absolute error, load location, 100 kN, pressure area 0.3 m × 0.4 m, Figure 43.

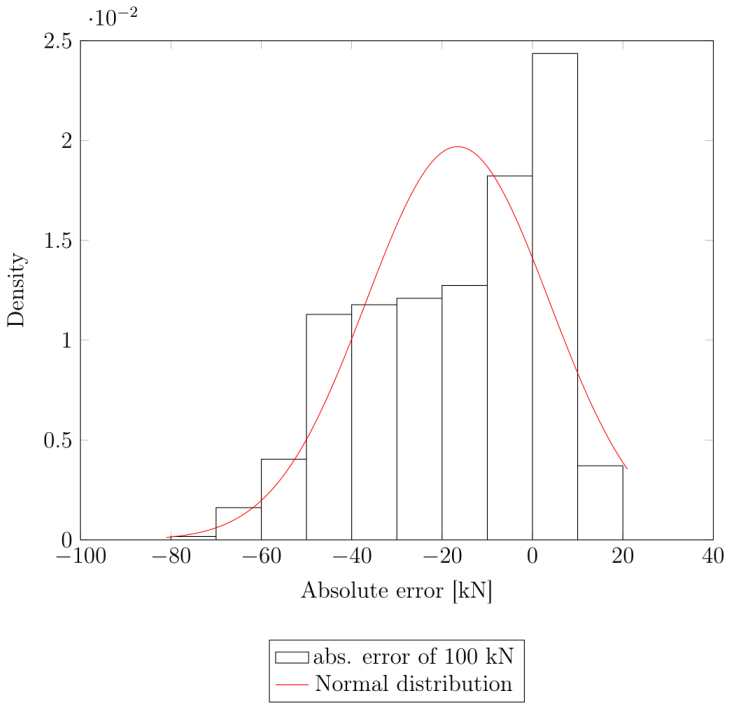

Figure 74: Probability density function of the absolute error, 100 kN, pressure area 0.3 m × 0.8 m, Figure 45.

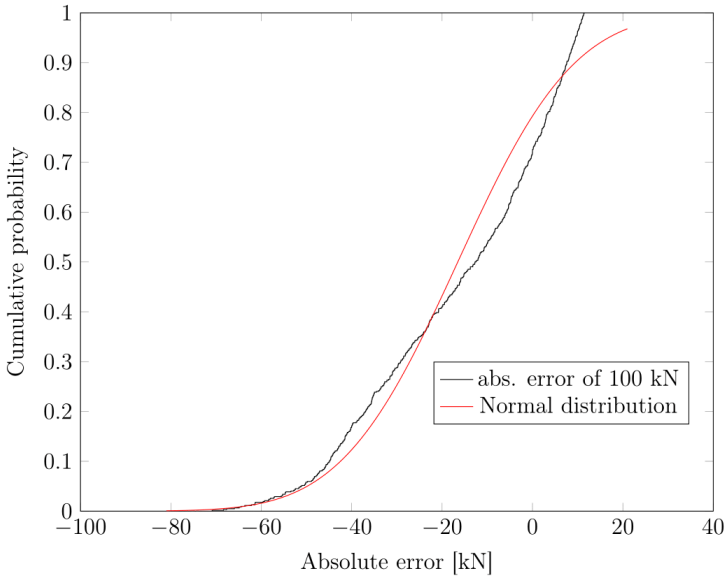

Figure 75: Cumulative density function of the absolute error, 100 kN, pressure area 0.3 m × 0.8 m, Figure 45.

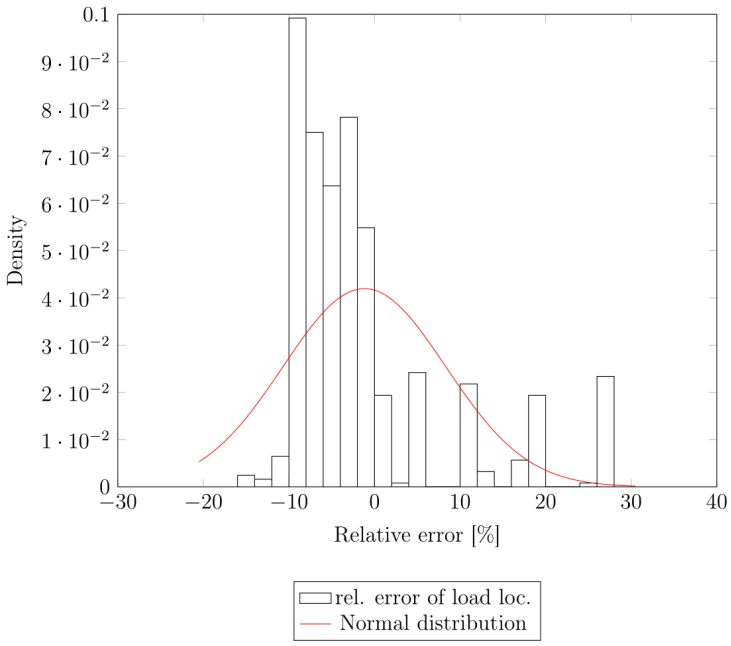

Figure 76: Probability density function of the absolute error, load location, 100 kN, pressure area 0.3 m × 0.8 m, Figure 46.

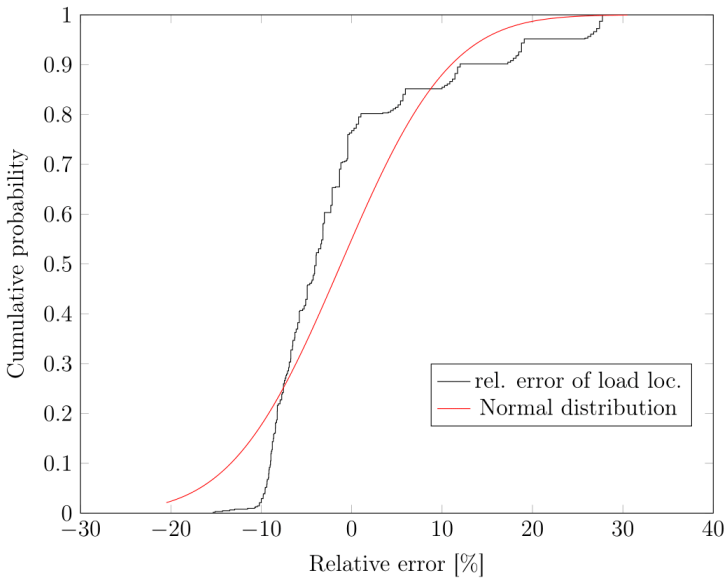

Figure 77: Cumulative density function of the absolute error, load location, 100 kN, pressure area 0.3 m × 0.8 m, Figure 46.

```
/clear
/PREP7
!Material and geometry data
Lg= 1.4                 !Frame length
s=  0.4                 !Frame spacing
hw= 0.2                 !Web height
Em= 209e9               !Young's modulus
nu= 0.3                 !Poission's ratio
tp= 0.02                !Plate thickness
tw= 0.019               !Web tichkness

ET,1,SHELL181
MPTEMP,,,,,,,,
MPTEMP,1,0
MPDATA,EX,1,,Em
MPDATA,PRXY,1,,nu

!Topology of the Grillage
!Keypoints
k,,0    ,0      ,0
k,,0    ,0.5*s  ,0
k,,Lg   ,0.5*s  ,0
k,,Lg   ,0      ,0
k,,0    ,0.5*s  ,hw
k,,Lg   ,0.5*s  ,hw
k,,0    ,1.5*s  ,0
k,,Lg   ,1.5*s  ,0
k,,0    ,1.5*s  ,hw
k,,Lg   ,1.5*s  ,hw
k,,0    ,2.5*s  ,0
k,,Lg   ,2.5*s  ,0
k,,0    ,2.5*s  ,hw
k,,Lg   ,2.5*s  ,hw
k,,0    ,3.5*s  ,0
k,,Lg   ,3.5*s  ,0
k,,0    ,3.5*s  ,hw
k,,Lg   ,3.5*s  ,hw
k,,0    ,4.5*s  ,0
k,,Lg   ,4.5*s  ,0
k,,0    ,4.5*s  ,hw
k,,Lg   ,4.5*s  ,hw
k,,0    ,5*s    ,0
k,,Lg   ,5*s    ,0

!Lines
L,       1,       2
L,       2,       3
L,       3,       4
L,       4,       1
L,       2,       7
L,       7,       8
L,       8,       3
L,       7,      11
L,      11,      12
L,      12,       8
L,      11,      15
L,      15,      16
L,      16,      12
L,      15,      19
L,      19,      20
L,      20,      16
L,      19,      23
L,      23,      24
L,      24,      20
L,       2,       5
L,       5,       6
L,       6,       3
L,       7,       9
L,       9,      10
```

Figure 78: Code for geometry creation in *Ansys 18.2*, Page 1.

```
 70  L,       10,        8
 71  L,       11,       13
 72  L,       13,       14
 73  L,       14,       12
 74  L,       15,       17
 75  L,       17,       18
 76  L,       18,       16
 77  L,       19,       21
 78  L,       21,       22
 79  L,       22,       20
 80
 81  lesize,all,hw/10        !Edge size for the elements
 82
 83  !Areas
 84  FLST,2,4,4
 85  FITEM,2,4
 86  FITEM,2,1
 87  FITEM,2,2
 88  FITEM,2,3
 89  AL,P51X
 90  FLST,2,4,4
 91  FITEM,2,2
 92  FITEM,2,5
 93  FITEM,2,6
 94  FITEM,2,7
 95  AL,P51X
 96  FLST,2,4,4
 97  FITEM,2,8
 98  FITEM,2,9
 99  FITEM,2,10
100  FITEM,2,6
101  AL,P51X
102  FLST,2,4,4
103  FITEM,2,11
104  FITEM,2,12
105  FITEM,2,13
106  FITEM,2,9
107  AL,P51X
108  FLST,2,4,4
109  FITEM,2,14
110  FITEM,2,15
111  FITEM,2,16
112  FITEM,2,12
113  AL,P51X
114  FLST,2,4,4
115  FITEM,2,15
116  FITEM,2,17
117  FITEM,2,18
118  FITEM,2,19
119  AL,P51X
120  FLST,2,4,4
121  FITEM,2,20
122  FITEM,2,21
123  FITEM,2,22
124  FITEM,2,2
125  AL,P51X
126  FLST,2,4,4
127  FITEM,2,23
128  FITEM,2,24
129  FITEM,2,25
130  FITEM,2,6
131  AL,P51X
132  FLST,2,4,4
133  FITEM,2,9
134  FITEM,2,26
135  FITEM,2,27
136  FITEM,2,28
137  AL,P51X
138  FLST,2,4,4
```

Figure 79: Code for geometry creation in *Ansys 18.2*, Page 2.

```
139  FITEM,2,29
140  FITEM,2,30
141  FITEM,2,31
142  FITEM,2,12
143  AL,P51X
144  FLST,2,4,4
145  FITEM,2,15
146  FITEM,2,32
147  FITEM,2,33
148  FITEM,2,34
149  AL,P51X
150
151  AREVERSE,5
152  AREVERSE,4
153  AREVERSE,3
154  AREVERSE,1
155  AREVERSE,7
156  AREVERSE,8
157  AREVERSE,10
158
159  !Sections
160  sect,1,shell,,
161  secdata, tp,1,0.0,5
162  secoffset,TOP
163  seccontrol,,,, , , ,
164
165  sect,2,shell,,
166  secdata, tw,1,0,5
167  secoffset,MID
168  seccontrol,,,, , , ,
169
170  !Assignment of Sections to Areas
171  asel,s,,,      1
172  asel,a,,,      2
173  asel,a,,,      3
174  asel,a,,,      4
175  asel,a,,,      5
176  asel,a,,,      6
177  aatt,1,,1,,1
178
179  asel,s,,,      7
180  asel,a,,,      8
181  asel,a,,,      9
182  asel,a,,,      10
183  asel,a,,,      11
184  aatt,1,,1,,2
185
186  !Meshing
187  asel,all
188  amesh,all
```

Figure 80: Code for geometry creation in *Ansys 18.2*, Page 3.

```
1   *cfopen,Results_ICM,dat !Write the ICM in a text file
2   *DIM,CMatrix,ARRAY,5,5  !Defines an array of 5x5
3
4   NLGEOM, on              !Includes large-deflection effects in a static or full
    transient analysis
5
6   !Starting the loop
7   *do,i,0,4,1
8           !Delete boundary conditions and forces
9           /PREP7
10          allsel,all
11          LSCLEAR,ALL
12
13          FINISH
14          /SOL
15          !Apply boundary conditions
16          nsel,s,loc,y,0
17          D,all, ,0, , , ,all,,, , ,
18          nsel,s,loc,y,5*s
19          D,all, ,0, , , ,all,,, , ,
20
21          nsel,s,loc,x,0
22          D,all, ,0, , , ,all,,, , ,
23          nsel,s,loc,x,Lg
24          D,all, ,0, , , ,all,,, , ,
25
26          !Apply the unit load
27          nsel,s,loc,z,0
28          nsel,r,loc,x,Lg/2
29          nsel,r,loc,y,((1/2)+i)*s
30
31          F,all,FZ,1000   !Unit load of 1 kN
32
33          !Before solve
34          allsel,all
35          !Solve
36          FINISH
37          /SOL
38          /STATUS,SOLU
39          SOLVE
40
41          FINISH
42          /POST1
43          !Get strains at the top side of the plate
44          SHELL,TOP
45          *GET,STRAINXZ_1uT,NODE,7387,EPEL,XZ
46          *GET,STRAINXZ_1oT,NODE,7747,EPEL,XZ
47          *GET,STRAINXZ_2uT,NODE,8097,EPEL,XZ
48          *GET,STRAINXZ_2oT,NODE,8457,EPEL,XZ
49          *GET,STRAINXZ_3uT,NODE,8807,EPEL,XZ
50          *GET,STRAINXZ_3oT,NODE,9167,EPEL,XZ
51          *GET,STRAINXZ_4uT,NODE,9877,EPEL,XZ
52          *GET,STRAINXZ_4oT,NODE,9517,EPEL,XZ
53          *GET,STRAINXZ_5uT,NODE,10587,EPEL,XZ
54          *GET,STRAINXZ_5oT,NODE,10227,EPEL,XZ
55          !Get strains at the bot side of the plate
56          SHELL,BOT
57          *GET,STRAINXZ_1uB,NODE,7387,EPEL,XZ
58          *GET,STRAINXZ_1oB,NODE,7747,EPEL,XZ
59          *GET,STRAINXZ_2uB,NODE,8097,EPEL,XZ
60          *GET,STRAINXZ_2oB,NODE,8457,EPEL,XZ
61          *GET,STRAINXZ_3uB,NODE,8807,EPEL,XZ
62          *GET,STRAINXZ_3oB,NODE,9167,EPEL,XZ
63          *GET,STRAINXZ_4uB,NODE,9877,EPEL,XZ
64          *GET,STRAINXZ_4oB,NODE,9517,EPEL,XZ
65          *GET,STRAINXZ_5uB,NODE,10587,EPEL,XZ
66          *GET,STRAINXZ_5oB,NODE,10227,EPEL,XZ
67          !Mean values of the strains
68          STRAINXZ_1u=(STRAINXZ_1uT+STRAINXZ_1uB)/2
```

Figure 81: Code for the calculation of the ICM in *Ansys 18.2*, Page 1.

```
69          STRAINXZ_1o=(STRAINXZ_1oT+STRAINXZ_1oB)/2
70          STRAINXZ_2u=(STRAINXZ_2uT+STRAINXZ_2uB)/2
71          STRAINXZ_2o=(STRAINXZ_2oT+STRAINXZ_2oB)/2
72          STRAINXZ_3u=(STRAINXZ_3uT+STRAINXZ_3uB)/2
73          STRAINXZ_3o=(STRAINXZ_3oT+STRAINXZ_3oB)/2
74          STRAINXZ_4u=(STRAINXZ_4uT+STRAINXZ_4uB)/2
75          STRAINXZ_4o=(STRAINXZ_4oT+STRAINXZ_4oB)/2
76          STRAINXZ_5u=(STRAINXZ_5uT+STRAINXZ_5uB)/2
77          STRAINXZ_5o=(STRAINXZ_5oT+STRAINXZ_5oB)/2
78          !Calculation of the C Matrix
79          diffgamma1=STRAINXZ_1o-STRAINXZ_1u
80          diffgamma2=STRAINXZ_2o-STRAINXZ_2u
81          diffgamma3=STRAINXZ_3o-STRAINXZ_3u
82          diffgamma4=STRAINXZ_4o-STRAINXZ_4u
83          diffgamma5=STRAINXZ_5o-STRAINXZ_5u
84
85          CMatrix(1,1+i)=diffgamma1,diffgamma2,diffgamma3,diffgamma4,diffgamma5
86
87          /INPUT,'ExportICM','inp',
88
89  *enddo
90  *MOPER,AMatrix,CMatrix,INVERT !Calculation of the ICM
```

Figure 82: Code for the calculation of the ICM in *Ansys 18.2*, Page 2.

```
/PREP7

NLGEOM, on              !Includes large-deflection effects in a static or full
transient analysis

*cfopen,Nonlinear,dat   !Write the results in text file
*DIM,dgamma,ARRAY,5,1   !Defines an array of 5x1

!Starting the loop for accuracy determinition
*do,i,0.02,Lg-0.02,0.02
    *do,j,0.02,5*s-0.02,0.02
        !Delete boundary conditions and forces
        /PREP7
        allsel,all
        LSCLEAR,ALL

        FINISH
        /SOLU
        !Apply boundary conditions
        nsel,s,loc,y,0
        D,all, ,0, , , ,all,,, , ,
        nsel,s,loc,y,5*s
        D,all, ,0, , , ,all,,, , ,

        nsel,s,loc,x,0
        D,all, ,0, , , ,all,,, , ,
        nsel,s,loc,x,Lg
        D,all, ,0, , , ,all,,, , ,

        !Apply the unit load
        nsel,s,loc,z,0
        nsel,r,loc,x,i
        nsel,r,loc,y,j

        F,all,FZ,1000   !Unit load of 1 kN

        !Before solve
        allsel,all
        !Solve
        FINISH
        /SOL
        /STATUS,SOLU
        SOLVE

        FINISH
        /POST1
        !Get strains at the top side of the plate
        SHELL,TOP
        *GET,STRAINXZ_1uT,NODE,7387,EPEL,XZ
        *GET,STRAINXZ_1oT,NODE,7747,EPEL,XZ
        *GET,STRAINXZ_2uT,NODE,8097,EPEL,XZ
        *GET,STRAINXZ_2oT,NODE,8457,EPEL,XZ
        *GET,STRAINXZ_3uT,NODE,8807,EPEL,XZ
        *GET,STRAINXZ_3oT,NODE,9167,EPEL,XZ
        *GET,STRAINXZ_4uT,NODE,9877,EPEL,XZ
        *GET,STRAINXZ_4oT,NODE,9517,EPEL,XZ
        *GET,STRAINXZ_5uT,NODE,10587,EPEL,XZ
        *GET,STRAINXZ_5oT,NODE,10227,EPEL,XZ
        !Get strains at the bot side of the plate
        SHELL,BOT
        *GET,STRAINXZ_1uB,NODE,7387,EPEL,XZ
        *GET,STRAINXZ_1oB,NODE,7747,EPEL,XZ
        *GET,STRAINXZ_2uB,NODE,8097,EPEL,XZ
        *GET,STRAINXZ_2oB,NODE,8457,EPEL,XZ
        *GET,STRAINXZ_3uB,NODE,8807,EPEL,XZ
        *GET,STRAINXZ_3oB,NODE,9167,EPEL,XZ
        *GET,STRAINXZ_4uB,NODE,9877,EPEL,XZ
        *GET,STRAINXZ_4oB,NODE,9517,EPEL,XZ
        *GET,STRAINXZ_5uB,NODE,10587,EPEL,XZ
```

Figure 83: Code for the calculation of the accuracy of the ICM in *Ansys 18.2*, Page 1.

```
69          *GET,STRAINXZ_5oB,NODE,10227,EPEL,XZ
70          !Mean values of the strains
71          STRAINXZ_1u=(STRAINXZ_1uT+STRAINXZ_1uB)/2
72          STRAINXZ_1o=(STRAINXZ_1oT+STRAINXZ_1oB)/2
73          STRAINXZ_2u=(STRAINXZ_2uT+STRAINXZ_2uB)/2
74          STRAINXZ_2o=(STRAINXZ_2oT+STRAINXZ_2oB)/2
75          STRAINXZ_3u=(STRAINXZ_3uT+STRAINXZ_3uB)/2
76          STRAINXZ_3o=(STRAINXZ_3oT+STRAINXZ_3oB)/2
77          STRAINXZ_4u=(STRAINXZ_4uT+STRAINXZ_4uB)/2
78          STRAINXZ_4o=(STRAINXZ_4oT+STRAINXZ_4oB)/2
79          STRAINXZ_5u=(STRAINXZ_5uT+STRAINXZ_5uB)/2
80          STRAINXZ_5o=(STRAINXZ_5oT+STRAINXZ_5oB)/2
81          !Calculation of the force on the plate frame system
82          diffgamma1=STRAINXZ_1o-STRAINXZ_1u
83          diffgamma2=STRAINXZ_2o-STRAINXZ_2u
84          diffgamma3=STRAINXZ_3o-STRAINXZ_3u
85          diffgamma4=STRAINXZ_4o-STRAINXZ_4u
86          diffgamma5=STRAINXZ_5o-STRAINXZ_5u
87
88          dgamma(1,1)=diffgamma1
89          dgamma(2,1)=diffgamma2
90          dgamma(3,1)=diffgamma3
91          dgamma(4,1)=diffgamma4
92          dgamma(5,1)=diffgamma5
93
94          *MOPER,Forc,AMatrix,MULT,dgamma
95          Summe=Forc(1,1)+Forc(2,1)+Forc(3,1)+Forc(4,1)+Forc(5,1)
96          Fehler=(((1-Summe)**2)**0.5)*100     !Error in percent
97          AbsFehler=Summe-1                    !Absolute error
98          !Load location determinition
99          xi1=STRAINXZ_1o*1.4/(STRAINXZ_1o-STRAINXZ_1u)
100         xi2=STRAINXZ_2o*1.4/(STRAINXZ_2o-STRAINXZ_2u)
101         xi3=STRAINXZ_3o*1.4/(STRAINXZ_3o-STRAINXZ_3u)
102         xi4=STRAINXZ_4o*1.4/(STRAINXZ_4o-STRAINXZ_4u)
103         xi5=STRAINXZ_5o*1.4/(STRAINXZ_5o-STRAINXZ_5u)
104
105             /INPUT,'NewError','inp',
106
107     *enddo
108 *enddo
109
```

Figure 84: Code for the calculation of the accuracy of the ICM in *Ansys 18.2*, Page 2.

```
!Line load
/PREP7

NLGEOM, on              !Includes large-deflection effects in a static or full
transient analysis

*cfopen,LineLoad08,dat  !Write the results in text file
*DIM,dgamma,ARRAY,5,1   !Defines an array of 5x1

!Starting the loop for accuracy determinition
*do,i,0,0.7-0.3+0.15,0.02
    *do,j,0,1-0.4+0.2,0.02
        !Delete boundary conditions and forces
        /PREP7
        allsel,all
        LSCLEAR,ALL

        FINISH
        /SOLU
        !Apply boundary conditions
        nsel,s,loc,y,0
        D,all, ,0, , , ,all,,, , ,
        nsel,s,loc,y,5*s
        D,all, ,0, , , ,all,,, , ,

        nsel,s,loc,x,0
        D,all, ,0, , , ,all,,, , ,
        nsel,s,loc,x,Lg
        D,all, ,0, , , ,all,,, , ,
        !Apply the unit load
        nsel,s,loc,z,0
        nsel,r,loc,x,0+i,0.3+i
        nsel,r,loc,y,0+j,0.8+j
        ESLN,s,1,all

        SFE,all,1,PRES, ,833.33e3, , ,  !100kN

        !Before solve
        allsel,all
        !Solve
        FINISH
        /SOL
        /STATUS,SOLU
        SOLVE

        FINISH
        /POST1

        !Get strains at the top side of the plate
        SHELL,TOP
        *GET,STRAINXZ_1uT,NODE,7387,EPEL,XZ
        *GET,STRAINXZ_1oT,NODE,7747,EPEL,XZ
        *GET,STRAINXZ_2uT,NODE,8097,EPEL,XZ
        *GET,STRAINXZ_2oT,NODE,8457,EPEL,XZ
        *GET,STRAINXZ_3uT,NODE,8807,EPEL,XZ
        *GET,STRAINXZ_3oT,NODE,9167,EPEL,XZ
        *GET,STRAINXZ_4uT,NODE,9517,EPEL,XZ
        *GET,STRAINXZ_4oT,NODE,9877,EPEL,XZ
        *GET,STRAINXZ_5uT,NODE,10227,EPEL,XZ
        *GET,STRAINXZ_5oT,NODE,10587,EPEL,XZ

        !Get strains at the bot side of the plate
        SHELL,BOT
        *GET,STRAINXZ_1uB,NODE,7387,EPEL,XZ
        *GET,STRAINXZ_1oB,NODE,7747,EPEL,XZ
        *GET,STRAINXZ_2uB,NODE,8097,EPEL,XZ
        *GET,STRAINXZ_2oB,NODE,8457,EPEL,XZ
        *GET,STRAINXZ_3uB,NODE,8807,EPEL,XZ
        *GET,STRAINXZ_3oB,NODE,9167,EPEL,XZ
```

Figure 85: Code for the calculation of the accuracy of the ICM for line loads in *Ansys 18.2*, Page 1.

```
69          *GET,STRAINXZ_4uB,NODE,9517,EPEL,XZ
70          *GET,STRAINXZ_4oB,NODE,9877,EPEL,XZ
71          *GET,STRAINXZ_5uB,NODE,10227,EPEL,XZ
72          *GET,STRAINXZ_5oB,NODE,10587,EPEL,XZ
73
74          !Mean values of the strains
75          STRAINXZ_1u=(STRAINXZ_1uT+STRAINXZ_1uB)/2
76          STRAINXZ_1o=(STRAINXZ_1oT+STRAINXZ_1oB)/2
77          STRAINXZ_2u=(STRAINXZ_2uT+STRAINXZ_2uB)/2
78          STRAINXZ_2o=(STRAINXZ_2oT+STRAINXZ_2oB)/2
79          STRAINXZ_3u=(STRAINXZ_3uT+STRAINXZ_3uB)/2
80          STRAINXZ_3o=(STRAINXZ_3oT+STRAINXZ_3oB)/2
81          STRAINXZ_4u=(STRAINXZ_4uT+STRAINXZ_4uB)/2
82          STRAINXZ_4o=(STRAINXZ_4oT+STRAINXZ_4oB)/2
83          STRAINXZ_5u=(STRAINXZ_5uT+STRAINXZ_5uB)/2
84          STRAINXZ_5o=(STRAINXZ_5oT+STRAINXZ_5oB)/2
85          !Calculation of the force on the plate frame system
86          diffgamma1=STRAINXZ_1o-STRAINXZ_1u
87          diffgamma2=STRAINXZ_2o-STRAINXZ_2u
88          diffgamma3=STRAINXZ_3o-STRAINXZ_3u
89          diffgamma4=STRAINXZ_4o-STRAINXZ_4u
90          diffgamma5=STRAINXZ_5o-STRAINXZ_5u
91
92          dgamma(1,1)=diffgamma1
93          dgamma(2,1)=diffgamma2
94          dgamma(3,1)=diffgamma3
95          dgamma(4,1)=diffgamma4
96          dgamma(5,1)=diffgamma5
97
98          !Calculation of the force on the plate frame system
99          *MOPER,Forc,AMatrix,MULT,dgamma
100         Summe=Forc(1,1)+Forc(2,1)+Forc(3,1)+Forc(4,1)+Forc(5,1)
101         !Mean value
102         MW=Summe/5
103         !Standard deviation
104
            Sigma=(((Forc(1,1)-MW)**2+(Forc(2,1)-MW)**2+(Forc(3,1)-MW)**2+(Forc(4,1)-MW)**2+(
            Forc(5,1)-MW)**2)/5)**(0.5)
105         AbsFehler=Summe-100 !100kN      !Absolute error
106
107         !Middle point
108         xm=0.15+i
109         ym=0.4+j
110
111         !Load location determinition
112         xi1=STRAINXZ_1o*1.4/(STRAINXZ_1o-STRAINXZ_1u)
113         xi2=STRAINXZ_2o*1.4/(STRAINXZ_2o-STRAINXZ_2u)
114         xi3=STRAINXZ_3o*1.4/(STRAINXZ_3o-STRAINXZ_3u)
115         xi4=STRAINXZ_4o*1.4/(STRAINXZ_4o-STRAINXZ_4u)
116         xi5=STRAINXZ_5o*1.4/(STRAINXZ_5o-STRAINXZ_5u)
117
118         /INPUT,'LineLoadError','inp',
119
120     *enddo
121 *enddo
122
```

Figure 86: Code for the calculation of the accuracy of the ICM for line loads in *Ansys 18.2*, Page 2.

```
1   !Load length determination
2   /PREP7
3
4   NLGEOM, on              !Includes large-deflection effects in a static or full
    transient analysis
5
6   *cfopen,LoadLDeti2,dat  !Write the results in text file
7   *DIM,dgamma,ARRAY,5,1   !Defines an array of 5x1
8
9   !Starting the loop
10      *do,j,0.02,1,0.02
11          !Delete boundary conditions and forces
12          /PREP7
13          allsel,all
14          LSCLEAR,ALL
15
16          FINISH
17          /SOLU
18          !Apply boundary conditions
19          nsel,s,loc,y,0
20          D,all, ,0, , , ,all,,, , ,
21          nsel,s,loc,y,5*s
22          D,all, ,0, , , ,all,,, , ,
23
24          nsel,s,loc,x,0
25          D,all, ,0, , , ,all,,, , ,
26          nsel,s,loc,x,Lg
27          D,all, ,0, , , ,all,,, , ,
28          !Apply the unit load
29          nsel,s,loc,z,0
30          nsel,r,loc,x,0.6,0.8
31          nsel,r,loc,y,1-j,1+j
32          ESLN,s,1,all
33
34          SFE,all,1,PRES, ,(100e3/(0.2*2*j)), , , !100kN
35
36          !Before solve
37          allsel,all
38          !Solve
39          FINISH
40          /SOL
41          /STATUS,SOLU
42          SOLVE
43
44          FINISH
45          /POST1
46
47          !Get strains at the top side of the plate
48          SHELL,TOP
49          *GET,STRAINXZ_1uT,NODE,7387,EPEL,XZ
50          *GET,STRAINXZ_1oT,NODE,7747,EPEL,XZ
51          *GET,STRAINXZ_2uT,NODE,8097,EPEL,XZ
52          *GET,STRAINXZ_2oT,NODE,8457,EPEL,XZ
53          *GET,STRAINXZ_3uT,NODE,8807,EPEL,XZ
54          *GET,STRAINXZ_3oT,NODE,9167,EPEL,XZ
55          *GET,STRAINXZ_4uT,NODE,9517,EPEL,XZ
56          *GET,STRAINXZ_4oT,NODE,9877,EPEL,XZ
57          *GET,STRAINXZ_5uT,NODE,10227,EPEL,XZ
58          *GET,STRAINXZ_5oT,NODE,10587,EPEL,XZ
59
60          !Get strains at the bot side of the plate
61          SHELL,BOT
62          *GET,STRAINXZ_1uB,NODE,7387,EPEL,XZ
63          *GET,STRAINXZ_1oB,NODE,7747,EPEL,XZ
64          *GET,STRAINXZ_2uB,NODE,8097,EPEL,XZ
65          *GET,STRAINXZ_2oB,NODE,8457,EPEL,XZ
66          *GET,STRAINXZ_3uB,NODE,8807,EPEL,XZ
67          *GET,STRAINXZ_3oB,NODE,9167,EPEL,XZ
68          *GET,STRAINXZ_4uB,NODE,9517,EPEL,XZ
```

Figure 87: Code for the calculation of load length in *Ansys 18.2*, Page 1.

```
69          *GET,STRAINXZ_4oB,NODE,9877,EPEL,XZ
70          *GET,STRAINXZ_5uB,NODE,10227,EPEL,XZ
71          *GET,STRAINXZ_5oB,NODE,10587,EPEL,XZ
72
73          !Mean values of the strains
74          STRAINXZ_1u=(STRAINXZ_1uT+STRAINXZ_1uB)/2
75          STRAINXZ_1o=(STRAINXZ_1oT+STRAINXZ_1oB)/2
76          STRAINXZ_2u=(STRAINXZ_2uT+STRAINXZ_2uB)/2
77          STRAINXZ_2o=(STRAINXZ_2oT+STRAINXZ_2oB)/2
78          STRAINXZ_3u=(STRAINXZ_3uT+STRAINXZ_3uB)/2
79          STRAINXZ_3o=(STRAINXZ_3oT+STRAINXZ_3oB)/2
80          STRAINXZ_4u=(STRAINXZ_4uT+STRAINXZ_4uB)/2
81          STRAINXZ_4o=(STRAINXZ_4oT+STRAINXZ_4oB)/2
82          STRAINXZ_5u=(STRAINXZ_5uT+STRAINXZ_5uB)/2
83          STRAINXZ_5o=(STRAINXZ_5oT+STRAINXZ_5oB)/2
84          !Calculation of the force on the plate frame system
85          diffgamma1=STRAINXZ_1o-STRAINXZ_1u
86          diffgamma2=STRAINXZ_2o-STRAINXZ_2u
87          diffgamma3=STRAINXZ_3o-STRAINXZ_3u
88          diffgamma4=STRAINXZ_4o-STRAINXZ_4u
89          diffgamma5=STRAINXZ_5o-STRAINXZ_5u
90
91          dgamma(1,1)=diffgamma1
92          dgamma(2,1)=diffgamma2
93          dgamma(3,1)=diffgamma3
94          dgamma(4,1)=diffgamma4
95          dgamma(5,1)=diffgamma5
96
97          !Calculation of the force on the plate frame system
98          *MOPER,Forc,AMatrix,MULT,dgamma
99          Summe=Forc(1,1)+Forc(2,1)+Forc(3,1)+Forc(4,1)+Forc(5,1)
100         !Mean value
101         MW=Summe/5
102         !Standard deviation
103
            Sigma=(((Forc(1,1)-MW)**2+(Forc(2,1)-MW)**2+(Forc(3,1)-MW)**2+(Forc(4,1)-MW)**2+(
            Forc(5,1)-MW)**2)/5)**(0.5)
104         AbsFehler=Summe-100 !100kN
105         !Load length
106         ll=2*j
107
108         /INPUT,'LineLDeti','inp',
109
110     *enddo
```

Figure 88: Code for the calculation of load length in *Ansys 18.2*, Page 2.